



Available online at www.sciencedirect.com

ScienceDirect

Comput. Methods Appl. Mech. Engrg. 399 (2022) 115340

Computer methods in applied mechanics and engineering

www.elsevier.com/locate/cma

A meshfree peridynamic model for brittle fracture in randomly heterogeneous materials

Yiming Fan^a, Huaiqian You^a, Xiaochuan Tian^b, Xiu Yang^c, Xingjie Li^d, Naveen Prakash^e, Yue Yu^a,*

a Department of Mathematics, Lehigh University, Bethlehem, PA, 18015, United States of America
 b Department of Mathematics, University of California, San Diego, CA, 92093, United States of America
 c Department of Industrial and Systems Engineering, Lehigh University, Bethlehem, PA, 18015, United States of America
 d Department of Mathematics and Statistics, University of North Carolina at Charlotte, Charlotte, NC, 28223, United States of America
 e Manufacturing Technology and Engineering, Corning Incorporated, Corning, NY, 14831, United States of America

Received 12 February 2022; received in revised form 30 June 2022; accepted 2 July 2022 Available online 18 July 2022

Abstract

In this work we aim to develop a unified mathematical framework and a reliable computational approach to model the brittle fracture in heterogeneous materials with variability in material microstructures, and to provide statistical metrics for quantities of interest, such as the fracture toughness. To describe the material responses such as the nucleation and growth of fractures in a uniform setting, we consider the peridynamics model. In particular, a stochastic state-based peridynamic model is developed, where the micromechanical parameters are modeled by a finite-dimensional random field, e.g., a combination of truncated random variables determined by the Karhunen-Loève decomposition or the principal component analysis (PCA). To solve this stochastic peridynamic problem, probabilistic collocation method (PCM) is employed to sample the random field that represents the micromechanical parameters. For each sample, the corresponding peridynamic problem is solved by an optimization-based meshfree quadrature rule. We present rigorous analysis for the proposed scheme and verify the convergence rate with a number of benchmark problems. The proposed scheme not only possesses the asymptotic compatibility spatially but also achieves an algebraic or sub-exponential convergence rate in the parametric random space when the number of collocation points grows. Finally, to validate the applicability of this approach on real-world fracture problems, we consider the problem of crystallization toughening in glass-ceramic materials, in which the material at the microstructural scale contains both amorphous glass and crystalline phases. The proposed stochastic peridynamic solver is employed to capture the crack initiation and its growth of the glass-ceramics with different crystal volume fractions, and the averaged fracture toughness are also calculated accordingly. The numerical estimates of fracture toughness show good consistency with data from experimental measurements. © 2022 Elsevier B.V. All rights reserved.

Keywords: Uncertainty quantification; Peridynamics; Meshfree method; Brittle fracture; Probabilistic collocation method; Heterogeneous material

E-mail addresses: yif319@lehigh.edu (Y. Fan), huy316@lehigh.edu (H. You), xctian@ucsd.edu (X. Tian), xiy518@lehigh.edu (X. Yang), xli47@uncc.edu (X. Li), PrakashN2@corning.com (N. Prakash), yuy214@lehigh.edu (Y. Yu).

^{*} Corresponding author.

1. Introduction

Detection and prediction of heterogeneous material damage are ubiquitous in applications of interest to the broad scientific and engineering community [1–10]. In disciplines ranging from material design to non-destructive evaluation, heterogeneities in materials and media need to be accurately captured to guarantee reliable and trustworthy damage predictions that inform decision making. In the past decades, important discoveries and advancements have been made toward understanding material microstructures and its relationship with damage observed in the macroscale. New experimental technologies and test procedures have been designed to observe much smaller microstructure patterns and make defects detection much faster [11–18]. On the other hand, novel mathematical models and numerical tools have been developed to describe failure initiation and progression, which provide relatively inexpensive alternatives to the extensive experimental testing [19–23]. However, fundamental challenges are still present in utilizing multiscale material models, and numerical simulations to provide a comprehensive physical and functional description of material damage, mainly due to the following difficulties [24]:

- 1. High complexity and heterogeneity in material damage problems generally require numerical simulations at fine scales that are often computationally prohibitive. Bottom-up approaches such as the fine-grained atomistic models have provided important insights into the fracture process, but they generally do not scale up to finite-size samples. This limitation raises the need for new mathematical models that act at coarser scales and capture complex nonlinear modes of failure from the fine scale.
- 2. Different material microstructures, properties, interfacial conditions, and operating environments all cause variability within materials, which is tremendously difficult to be fully quantified. Therefore, without complete detailed measurements for each individual material sample, it is often non-practical, if not impossible, to provide full quantitative damage characterization. This fact calls for stochastic modeling of the variability and characterization of material failure for uncertainty quantification.

These two challenges both call for mathematical models that not only capture the material fracture initiation and progression, but also account for heterogeneity and variability. To describe crack initiation and evolution simultaneously from the microscale up, we employ the peridynamic theory, a spatially nonlocal continuum theory, which provides a description of continuum mechanics in terms of integral operators rather than classical differential operators [25–40]. These nonlocal models are defined in terms of a lengthscale δ , referred to as a horizon, which denotes the range of nonlocal interaction between particles. The integral operator allows a natural description of processes requiring reduced regularity in the relevant solution, such as fracture mechanics [41,42]. Therefore in peridynamics the material damage can be captured autonomously as a natural component of the material deformation. To account for heterogeneity and variability, we propose to develop a stochastic peridynamics formulation where the heterogeneous material property is modeled by a random field. Currently, most of the stateof-the-art works on peridynamics consider a homogenized and/or deterministic model. However, a deterministic and homogenized model may not work well when the material is highly heterogeneous, since the microstructure may play a critical role in those materials. In a recent study on reinforced concrete modeling, Zhao et al. found that a fully homogenized peridynamic model fails to capture certain fracture modes/patterns [43] in a correct manner. Therefore, they have proposed a stochastic bond-based peridynamic model where the material property is described by random fields. Each bond connecting two material points x and y is modeled by a random variable, and the discrete probability distribution of this random variable depends on the volume fraction of aggregate and cement. With this model, fracture patterns match experimental observations. Their findings indicate the importance of incorporating the spatial variability of material properties in peridynamics. However, in [43] the authors focused on the crack pattern in individual realizations rather than the solution's statistics. Their numerical study only provides a qualitative validation of the fracture patterns and the order in which various cracks develop. To provide quantitative verification and validation of the model, it calls for an effective stochastic method to provide the statistical metric on the impact of microstructure variability.

In this work, we propose a stochastic state-based peridynamics model where the heterogeneous material property varies spatially and is described by a random field. The solution to this stochastic problem describes the statistics of the material responses, such as the displacement and damage fields. In particular, we employ the linear peridynamic solid (LPS) model [44] as a prototypical state-based model which is appropriate for brittle fracture, and propose a heterogeneous LPS formulation where the formulation of two-point function is used to describe

the heterogeneous material properties. Although such an averaged two-point function formulation was developed for nonlocal diffusion [45,46] and peridynamics [47–51] models, we have for the first time provided rigorous mathematical analysis for the well-posedness of this formulation in a heterogeneous LPS model. Furthermore, an important feature of peridynamics is that when classical continuum models still apply, peridynamics revert to classical continuum models as its horizon size $\delta \to 0$. Numerical discretizations which preserve this limit under the grid refinement $h \to 0$ are termed as asymptotically compatible (AC) [52], and there have been significant works in recent years toward establishing such discretizations [33,45,52–61]. In this work, we have also rigorously shown that our stochastic heterogeneous LPS model guarantees consistency to the corresponding local limit, which provides a critical ingredient in achieving a convergent simulation in an asymptotic compatible way.

To study the impact of microstructure variability, our second objective is to numerically discretize the proposed stochastic peridynamics model and compute the first two statistical moments, i.e., the mean and (co)variance. The mean provides an unbiased estimate of the variables and the variance quantifies the uncertainty associated with this estimate. Such a development calls for a comprehensive treatment of an AC spatial discretization together with an effective stochastic approximation method, which can provide fast and convergent simulations for the heterogeneous peridynamic fractures and offer stochastic modeling for the variability and characterization of material failure for uncertainty quantification. Generally speaking, AC spatial discretization strategies for peridynamics can be classified into two categories. The first class involves traditional finite element formulations and carefully performing geometric calculations to integrate over relevant horizon/element subdomains, while the second type adopts a strong-form meshfree discretization where particles are associated with an abstract measure, and provides a sharp representation of the fracture surface by breaking bonds. The former is based on a variational setting and therefore is more amenable to mathematical analysis, while the latter is simple to implement and is generally faster [62,63]. In this paper, we pursue the meshfree viewpoint. In particular, a meshfree method is developed based on the optimization-based quadrature rule [33,34,45,65]. For the stochastic numerical method, several approaches were developed for stochastic local (classical) PDE models, including probabilistic Galerkin methods (PGMs) [66–72], probabilistic collocation methods (PCMs) [73–77], reduced basis methods [46,78–82], etc. Among these methods, PCM with sparse grids inherits the ease of implementation in the Monte Carlo methods since only solutions at sample points are needed. At the same time, it also reduces the required number of sample points to achieve a given numerical accuracy for problems described by a relatively high dimensional random space. Consequently in this work, we will employ PCM with full tensor products for random dimensions $N \le 4$, and PCM with sparse grids when the dimension of random space is more than 4, following the suggestion by [77]. To verify and validate the proposed model as well as the numerical approach, we numerically investigate the convergence to the analytical local limit for a number of benchmark problems, including manufactured smooth solutions, composite material with discontinuous material properties, and material fracture problems. In addition, we validate the estimates of fracture toughness on randomly heterogeneous materials against an experiment of glass-ceramics [83], providing evidence that the scheme yields accurate predictions for statistic damage metrics in practical engineering applications.

The paper is organized as follows. We firstly describe the deterministic and stochastic heterogeneous LPS problems in Section 2, and provide mathematical analysis to establish their compatibility with the corresponding local problems. Next, we pursue a consistent discretization. The numerical approach for stochastic LPS problems is proposed in Section 3 and is numerically verified in Section 4. When no fracture occurs and the material properties are sufficiently smooth, the classical continuum theory applies and the formulation preserves the AC limit for δ -convergence, with an optimal $O(\delta^2)$ convergence rate. When fracture occurs and/or the material properties present discontinuity, the spatial discretization formulation is still able to capture the material heterogeneity and the resulting damage field, with an $O(\delta)$ convergence rate to the local limit. Although the linear convergence with respect to δ was reported in previous literature on deterministic nonlocal diffusion problems with interfaces [84,85], this work has for the first time provided a systematic study on stochastic and peridynamic problems. When the nonlocal solution is analytic with respect to the input random variables, this method at least guarantees an algebraic convergence (for PCM with sparse grids) or exponential convergence (for PCM with full tensor products) with respect to increasing sample size. Therefore, we have established a unified mathematical framework, which is able to incorporate all of the necessary ingredients to perform non-trivial simulations of fracture mechanics in

¹ For peridynamics one often refines both δ and h at the same rate under so-called δ -convergence [64]. In this setting, banded stiffness matrix is obtained which allows scalable implementations. Although in the literature a scheme is termed AC if it recovers the solution whenever δ , $h \rightarrow 0$, in this work we adopt a practical setting and only require the δ -convergence for AC.

heterogeneous materials while ensuring a scalable implementation and guaranteed convergence rate. In Section 5, we further extend the proposed formulation to handle a more engineering-oriented problem, which is a glassy matrix containing randomly distributed crystal grains. A quasi-static brittle fracture model is considered. The numerical results provide preliminary quantitative validation when compared with available experimental measurements on material fracture toughness. Section 6 summarizes our findings and discusses future research. Additional discussions and detailed proofs are provided in Appendix.

2. Peridynamics for randomly heterogeneous materials

In this section, we introduce the state-based peridynamics formulation, together with the major notations and definitions. In particular, we consider the LPS model [44], which is a prototypical state-based model appropriate for brittle fracture. The LPS model may be interpreted as a nonlocal generalization of the mixed form of linear elasticity, evolving both displacements and a dilatation. We begin with a review of the deterministic LPS model for heterogeneous materials [34] in Section 2.1, then extend the formulation to the stochastic LPS problem with random parameters in Section 2.2. Finally, we discuss the treatment of material fracture, including the damage criteria and the handling of free surfaces created by the evolving fractures, in Section 2.3.

2.1. Deterministic peridynamics problem with heterogeneous material properties

We begin by reviewing the governing equations of deterministic LPS models which provide the foundation for the stochastic problems of interest. In this section, we consider the material without damage, with fully prescribed Dirichlet type boundary conditions, and will further extend the discussions to more general boundary conditions and brittle fractures in Section 2.3.

Consider a body occupying a bounded Lipschitz and convex domain $\Omega \subset \mathbb{R}^d$, d=2 or 3, with Dirichlet-type boundary conditions. Let $u:\Omega \to \mathbb{R}^d$ be the displacement field, $\theta:\Omega \to \mathbb{R}$ be the nonlocal dilatation, generalizing the local divergence of displacement, and $K:\mathbb{R}^d \times \mathbb{R}^d \to \mathbb{R}^+ \cup \{0\}$ is a nonnegative kernel function. In this paper we further assume that the interacting kernel function K is radially symmetric (which can therefore be denoted as K(r) for $r \in \mathbb{R}^+ \cup \{0\}$, with a slight abuse of notation), with compactly support on $B_\delta(0)$, the δ -ball centered at 0, and satisfies the following conditions:

$$\begin{cases} K(\boldsymbol{x}, \boldsymbol{y}) = K(|\boldsymbol{x} - \boldsymbol{y}|) = K_{\delta}(|\boldsymbol{x} - \boldsymbol{y}|) = \frac{1}{\delta^{d+2}} K_{1} \left(\frac{|\boldsymbol{x} - \boldsymbol{y}|}{\delta}\right), \\ \text{where } K_{1} \text{ is nonnegative and there exists a positive constant } \zeta < 1 \text{ satisfying} \\ B_{\zeta}(\boldsymbol{0}) \subset \text{supp}(K_{1}) \subset B_{1}(\boldsymbol{0}) \text{ and } \int_{B_{1}(\boldsymbol{0})} K_{1}(|\boldsymbol{z}|)|\boldsymbol{z}|^{2} d\boldsymbol{z} = d. \end{cases}$$
 (2.1)

The above kernel assumptions have implications on the boundary conditions that are prescribed on a collar of thickness δ near the boundary $\partial \Omega$, that we denote as

$$\mathcal{I}\Omega := \{ \mathbf{x} \in \Omega | \operatorname{dist}(\mathbf{x}, \partial \Omega) < \delta \}, \ \mathcal{B}\Omega := \{ \mathbf{x} \notin \Omega | \operatorname{dist}(\mathbf{x}, \partial \Omega) < \delta \}, \ \mathcal{B}\mathcal{B}\Omega := \{ \mathbf{x} \notin \Omega | \operatorname{dist}(\mathbf{x}, \partial \Omega) < 2\delta \}.$$

To apply the nonlocal Dirichlet-type boundary condition, we assume that $u(x) = u_D(x)$ are provided in $\mathcal{BB}\Omega$. Without loss of generality, for the analysis, we consider homogeneous Dirichlet boundary conditions $u_D(x) = 0$.

In the original LPS model for materials with homogeneous material properties [44], the momentum balance is given by the following

$$\mathcal{L}_{\delta}\boldsymbol{u} := -\frac{C_{\alpha}}{d} \int_{B_{\delta}(\boldsymbol{x})} (\lambda - \mu) K(|\boldsymbol{y} - \boldsymbol{x}|) (\boldsymbol{y} - \boldsymbol{x}) (\theta(\boldsymbol{x}) + \theta(\boldsymbol{y})) d\boldsymbol{y}$$

$$-\frac{C_{\beta}}{d} \int_{B_{\delta}(\boldsymbol{x})} \mu K(|\boldsymbol{y} - \boldsymbol{x}|) \frac{(\boldsymbol{y} - \boldsymbol{x}) \otimes (\boldsymbol{y} - \boldsymbol{x})}{|\boldsymbol{y} - \boldsymbol{x}|^{2}} (\boldsymbol{u}(\boldsymbol{y}) - \boldsymbol{u}(\boldsymbol{x})) d\boldsymbol{y} = \boldsymbol{f}(\boldsymbol{x}), \quad \text{for } \boldsymbol{x} \in \Omega,$$

$$(2.2)$$

where the nonlocal dilatation $\theta(x)$ is defined as

$$\theta(\mathbf{x}) := \int_{B_{\delta}(\mathbf{x})} K(|\mathbf{y} - \mathbf{x}|)(\mathbf{y} - \mathbf{x}) \cdot (\mathbf{u}(\mathbf{y}) - \mathbf{u}(\mathbf{x})) \, d\mathbf{y}, \text{ for } \mathbf{x} \in \Omega \cup \mathcal{B}\Omega.$$
(2.3)

Here, $f \in \mathbb{R}^d$ denotes the external body loading forces, and μ , λ denote the (constant) shear modulus and Lamé first parameter, respectively. With appropriate choice of scaling parameters $C_{\alpha} > 0$, $C_{\beta} > 0$ and the kernel function K(r), it can be shown that the system converges to the Navier equations [86–88] for linear elasticity:

$$\mathcal{L}_0 \mathbf{u} := -\nabla \cdot (\lambda \operatorname{tr}(\mathbf{E})\mathbf{I} + 2\mu \mathbf{E}) = -(\lambda - \mu)\nabla[\operatorname{tr}(\mathbf{E})] - \mu\nabla \cdot (2\mathbf{E} + \operatorname{tr}(\mathbf{E})\mathbf{I}) = \mathbf{f}, \tag{2.4}$$

where the strain tensor $\mathbf{E} := \frac{1}{2}(\nabla \mathbf{u} + (\nabla \mathbf{u})^T)$ and $\mathrm{tr}(\mathbf{E})$ denotes its trace. To recover parameters for 3D linear elasticity, one should take $C_{\alpha} = 3$, $C_{\beta} = 30$; whereas for 2D problems, $C_{\alpha} = 2$, $C_{\beta} = 16$. In this paper we consider 2D problems (d = 2), although the algorithm may be generalized to more general kernels and 3D cases.

In [34], the authors extended the above original LPS model to composite materials constituted of multiple phases, where the domain was partitioned into disjoint subdomains with piecewise constant material properties such that $\lambda(x)$ and $\mu(x)$ may vary for each material point x. In this work, we propose to further extend the original LPS model (2.2) and (2.3) to the general heterogeneous materials, with either continuous or discontinuous material parameters $\lambda(x)$ and $\mu(x)$. Specifically, for the deterministic problem where the Lamé moduli $\lambda(x)$ and $\mu(x)$ may vary for each material point x, satisfying

$$0 < \lambda_0 = \inf_{\mathbf{x} \in \Omega \cup \mathcal{BB}\Omega} \lambda(\mathbf{x}) \le \sup_{\mathbf{x} \in \Omega \cup \mathcal{BB}\Omega} \lambda(\mathbf{x}) = \lambda_\infty < \infty,$$

$$0<\mu_0=\inf_{\boldsymbol{x}\in\Omega\cup\mathcal{B}\mathcal{B}\Omega}\mu(\boldsymbol{x})\leq\sup_{\boldsymbol{x}\in\Omega\cup\mathcal{B}\mathcal{B}\Omega}\mu(\boldsymbol{x})=\mu_\infty<\infty,$$

we employ the following momentum balance and nonlocal dilatation formulations:

$$\mathcal{L}_{H\delta} \boldsymbol{u} := -\int_{B_{\delta}(x)} (\lambda(x, y) - \mu(x, y)) K(|y - x|) (y - x) (\theta(x) + \theta(y)) dy -8 \int_{B_{\delta}(x)} \mu(x, y) K(|y - x|) \frac{(y - x) \otimes (y - x)}{|y - x|^{2}} (\boldsymbol{u}(y) - \boldsymbol{u}(x)) dy = f(x),$$
(2.5)

where θ is defined in (2.3), and the two-point functions $\mu(\cdot, \cdot)$, $\lambda(\cdot, \cdot)$ denote averaged material properties. Specifically, we consider the interaction between x and y as a series of two springs connecting the two points, and then the equivalent total spring constant will be the harmonic mean of the two spring constants [47,51,89]:

$$\frac{2}{\mu(x, y)} = \frac{1}{\mu(x)} + \frac{1}{\mu(y)}, \quad \frac{2}{\lambda(x, y)} = \frac{1}{\lambda(x)} + \frac{1}{\lambda(y)}.$$
 (2.6)

We notice that $\mu(\cdot, \cdot)$ and $\lambda(\cdot, \cdot)$ will also satisfy

$$0<\lambda_0=\inf_{x,y\in\Omega\cup\mathcal{BB}\Omega}\lambda(x,\,y)\leq\sup_{x,y\in\Omega\cup\mathcal{BB}\Omega}\lambda(x,\,y)=\lambda_\infty<\infty,$$

$$0<\mu_0=\inf_{\pmb{x},\pmb{y}\in\Omega\cup\mathcal{BB}\Omega}\mu(\pmb{x},\pmb{y})\leq\sup_{\pmb{x},\pmb{y}\in\Omega\cup\mathcal{BB}\Omega}\mu(\pmb{x},\pmb{y})=\mu_\infty<\infty.$$

For the proof of the algorithm's wellposedness, we will also need the following assumptions on λ_0 , μ_0 , λ_{∞} and μ_{∞} :

Assumption 1. There exist two constants $A_0, A_1 > 0$ such that

$$(4 - A_1)\mu_0 - A_0(\lambda_\infty - \lambda_0) > 0, (2.7)$$

$$\lambda_{\infty} - \frac{\lambda_{\infty} - \lambda_0}{2A_0} - \frac{\mu_{\infty}}{2A_1} \ge 0. \tag{2.8}$$

Remark 1. We note that the above assumption generally requires an upper bound of μ_{∞} and a relatively small fluctuation of $\lambda(x)$ and $\mu(x)$. When considering homogeneous materials where the Lamé and shear modulus $\lambda(x)$ and $\mu(x)$ are both constants, we have $\lambda_{\infty} - \lambda_0 = 0$ and the two conditions yield $8\lambda_{\infty} > \mu_{\infty}$. This condition is suboptimal, since the homogeneous LPS model can be proved to be well-posed given any $\lambda, \mu > 0$ (see, e.g., [88]).

In Sections 4–5, empirical experiments are performed on cases that do not satisfy Assumption 1. Stable and converging numerical results are still observed. We will investigate more general and optimal conditions of λ and μ in future work.

Consider a (quasi) static state-based peridynamic problem with Dirichlet-type boundary conditions:

$$\begin{cases}
\mathcal{L}_{H\delta}u(x) = f(x), & \text{in } \Omega \\
\theta(x) = \int_{B_{\delta}(x)} K(|y - x|)(y - x) \cdot (u(y) - u(x)) \, dy, & \text{in } \Omega \cup \mathcal{B}\Omega \\
u(x) = u_D(x), & \text{in } \mathcal{B}\Omega
\end{cases} \tag{2.9}$$

we multiply a test function v(x) satisfying v(x) = 0 in $\mathcal{BB}\Omega$ to (2.5), integrate it with respect to $x \in \Omega \cup \mathcal{BB}\Omega$, then we obtain the weak formulation

$$\begin{split} &(f, \mathbf{v})_{L^{2}(\Omega)} \\ &= -\int_{\Omega \cup \mathcal{B} \mathcal{B} \Omega} \int_{\Omega \cup \mathcal{B} \mathcal{B} \Omega} \left(\lambda(\mathbf{x}, \mathbf{y}) - \mu(\mathbf{x}, \mathbf{y}) \right) K(|\mathbf{y} - \mathbf{x}|) \left(\mathbf{y} - \mathbf{x} \right) \cdot \mathbf{v}(\mathbf{x}) \left(\theta(\mathbf{x}) + \theta(\mathbf{y}) \right) d\mathbf{y} d\mathbf{x} \\ &- 8 \int_{\Omega \cup \mathcal{B} \mathcal{B} \Omega} \int_{\Omega \cup \mathcal{B} \mathcal{B} \Omega} \mu(\mathbf{x}, \mathbf{y}) K(|\mathbf{y} - \mathbf{x}|) \frac{(\mathbf{y} - \mathbf{x}) \otimes (\mathbf{y} - \mathbf{x})}{|\mathbf{y} - \mathbf{x}|^{2}} \left(\mathbf{u}(\mathbf{y}) - \mathbf{u}(\mathbf{x}) \right) d\mathbf{y} \mathbf{v}(\mathbf{x}) d\mathbf{x} \\ &= \int_{\Omega \cup \mathcal{B} \mathcal{B} \Omega} \int_{\Omega \cup \mathcal{B} \mathcal{B} \Omega} \left(\lambda(\mathbf{x}, \mathbf{y}) - \mu(\mathbf{x}, \mathbf{y}) \right) K(|\mathbf{y} - \mathbf{x}|) \left(\mathbf{y} - \mathbf{x} \right) \cdot (\mathbf{v}(\mathbf{y}) - \mathbf{v}(\mathbf{x})) d\mathbf{y} \theta(\mathbf{x}) d\mathbf{x} \\ &+ 4 \int_{\Omega \cup \mathcal{B} \mathcal{B} \Omega} \int_{\Omega \cup \mathcal{B} \mathcal{B} \Omega} \mu(\mathbf{x}, \mathbf{y}) \frac{K(|\mathbf{y} - \mathbf{x}|)}{|\mathbf{y} - \mathbf{x}|^{2}} [(\mathbf{y} - \mathbf{x}) \cdot (\mathbf{u}(\mathbf{y}) - \mathbf{u}(\mathbf{x}))] [(\mathbf{y} - \mathbf{x}) \cdot (\mathbf{v}(\mathbf{y}) - \mathbf{v}(\mathbf{x}))] d\mathbf{y} d\mathbf{x} \\ &\coloneqq T_{H\delta}[\mathbf{u}, \mathbf{v}; \lambda, \mu], \end{split}$$

where θ is defined by (2.3) and λ , μ are the two point material property functions defined in (2.6). We also denote the strain energy density function at material point x as

$$W_{\boldsymbol{u}}(\boldsymbol{x}) := \int_{\Omega \cup \mathcal{B} \mathcal{B} \Omega} (\lambda(\boldsymbol{x}, \boldsymbol{y}) - \mu(\boldsymbol{x}, \boldsymbol{y})) K(|\boldsymbol{y} - \boldsymbol{x}|) (\boldsymbol{y} - \boldsymbol{x}) \cdot (\boldsymbol{v}(\boldsymbol{y}) - \boldsymbol{v}(\boldsymbol{x})) d\boldsymbol{y} \theta(\boldsymbol{x})$$

$$+ 4 \int_{\Omega \cup \mathcal{B} \mathcal{B} \Omega} \mu(\boldsymbol{x}, \boldsymbol{y}) \frac{K(|\boldsymbol{y} - \boldsymbol{x}|)}{|\boldsymbol{y} - \boldsymbol{x}|^2} [(\boldsymbol{y} - \boldsymbol{x}) \cdot (\boldsymbol{u}(\boldsymbol{y}) - \boldsymbol{u}(\boldsymbol{x}))]^2 d\boldsymbol{y}.$$

With the boundedness properties of $\lambda(\cdot, \cdot)$ and $\mu(\cdot, \cdot)$, we have the following characterization of the space, with detailed proof elaborated in Appendix A.1.

Lemma 1. The nonlocal energy semi-norm is

$$|\boldsymbol{u}|_{S_{H\delta}(\Omega)} = \left[\int_{\Omega \cup BB\Omega} \int_{\Omega \cup BB\Omega} \frac{K(|\boldsymbol{y} - \boldsymbol{x}|)}{|\boldsymbol{y} - \boldsymbol{x}|^2} [(\boldsymbol{y} - \boldsymbol{x}) \cdot (\boldsymbol{u}(\boldsymbol{y}) - \boldsymbol{u}(\boldsymbol{x}))]^2 d\boldsymbol{y} d\boldsymbol{x} \right]^{1/2},$$

and the nonlocal energy space is

$$S_{H\delta}(\Omega) = \left\{ \boldsymbol{u} \in L^{2}(\Omega; \mathbb{R}^{d}) : \int_{\Omega \cup \mathcal{B}B\Omega} \int_{\Omega \cup \mathcal{B}B\Omega} \frac{K(|\boldsymbol{y} - \boldsymbol{x}|)}{|\boldsymbol{y} - \boldsymbol{x}|^{2}} [(\boldsymbol{y} - \boldsymbol{x}) \cdot (\boldsymbol{u}(\boldsymbol{y}) - \boldsymbol{u}(\boldsymbol{x}))]^{2} d\boldsymbol{y} d\boldsymbol{x} < \infty, \ \boldsymbol{u}|_{\mathcal{B}B\Omega} = \boldsymbol{0} \right\}.$$

In the rest of this paper, we will use $||\boldsymbol{u}||_{L^2}$ to denote the $L^2(\Omega; \mathbb{R}^d)$ norm of \boldsymbol{u} , and $||\boldsymbol{u}||_{S_{H\delta}}$ to denote the norm on $S_{H\delta}(\Omega)$:

$$||\mathbf{u}||_{S_{H\delta}}^2 = ||\mathbf{u}||_{L^2}^2 + |\mathbf{u}|_{S_{H\delta}}^2.$$

With the equivalence of the total strain energy with the $|\cdot|_{S_{H\delta}}$ seminorm proved in Lemma 1, similar as in [88] we have the following characterization of the zero energy solution:

Lemma 2. For all $u \in S_{H\delta}(\Omega)$, $\int_{\Omega \cup BB\Omega} W_u(x) dx \geq 0$, and

$$\mathbf{u} = \mathbf{0} \text{ in } \Omega \cup \mathcal{BB}\Omega \Longleftrightarrow |\mathbf{u}|_{S_{H\delta}} = 0 \Longleftrightarrow \int_{\Omega \cup \mathcal{BB}\Omega} W_{\mathbf{u}}(\mathbf{x}) d\mathbf{x} = 0.$$

Following [87, Proposition 5.3] and [88, Proposition 5], we also have the nonlocal Poincare inequality:

Lemma 3. There exist $\overline{\delta} > 0$ and a constant $C = C(\overline{\delta})$ such that for all $\delta \in (0, \overline{\delta})$ we have

$$||\boldsymbol{u}||_{L^2} \leq C|\boldsymbol{u}|_{S_{H\delta}}, \ \forall \boldsymbol{u} \in S_{H\delta}(\Omega).$$

With the above lemmas, we obtain the coercivity and continuity of the bilinear form $T_{H\delta}[u, v; \lambda, \mu]$:

Lemma 4. There exist $\overline{\delta} > 0$ and two constants $r = r(\overline{\delta}) > 0$ and C > 0 such that for all $\delta \in (0, \overline{\delta})$ we have

Coercivity:
$$T_{H\delta}[\boldsymbol{u}, \boldsymbol{u}; \lambda, \mu] \ge r||\boldsymbol{u}||_{S_{H\delta}}^2,$$
 (2.10)

Continuity:
$$T_{H\delta}[\boldsymbol{u}, \boldsymbol{v}; \lambda, \mu] \le C||\boldsymbol{u}||_{S_{H\delta}}||\boldsymbol{v}||_{S_{H\delta}},$$
 (2.11)

for any $\boldsymbol{u}, \boldsymbol{v} \in S_{H\delta}(\Omega)$.

Proof. The coercivity of $T_{H\delta}$ is an immediate result of Lemmas 1 and 3. The continuity is obtained by applying (A.1) and (A.2). \Box

Finally, denoting the dual space of $S_{H\delta}(\Omega)$ as $S_{H\delta}(\Omega)^*$, the well-posedness result is obtained as an application of the Lax–Milgram theorem:

Theorem 1. For a given body load $f \in S_{H\delta}(\Omega)^*$, there exists a unique $\mathbf{u} \in S_{H\delta}(\Omega)$ such that

$$T_{H\delta}[\boldsymbol{u}, \boldsymbol{v}; \lambda, \mu] = \langle \boldsymbol{f}, \boldsymbol{v} \rangle, \ \forall \boldsymbol{v} \in S_{H\delta}(\Omega).$$

With the well-posedness proved, we now investigate the consistency of the proposed nonlocal formulation with the classical linear elastic model as $\delta \to 0$. Specifically, the classical linear elastic model with heterogeneous material parameters writes²:

$$\begin{cases}
\mathcal{L}_{H0}\mathbf{u}(\mathbf{x}) := -(\lambda(\mathbf{x}) - \mu(\mathbf{x}))\nabla[\operatorname{tr}(\mathbf{E}(\mathbf{x}))] - \mu(\mathbf{x})\nabla \cdot (2\mathbf{E}(\mathbf{x}) + \operatorname{tr}(\mathbf{E}(\mathbf{x}))\mathbf{I}) = \mathbf{f}(\mathbf{x}), & \text{in } \Omega, \\
\mathbf{u}(\mathbf{x}) = \mathbf{u}_D(\mathbf{x}), & \text{on } \mathcal{BB}\Omega,
\end{cases} \tag{2.12}$$

where $\mathbf{E}(x) := \frac{1}{2}(\nabla u(x) + (\nabla u(x))^T)$. We denote u_{δ} as the solution of the peridynamics problem (2.9) and u_0 as the solution of (2.12), and aim to show that $u_{\delta} \to u_0$ as $\delta \to 0$.

We first study the consistency of operators with the following lemma. Detailed proofs are elaborated in Appendix A.2.

Lemma 5. Assume that $\mathbf{u} \in C^4(\overline{\Omega \cup \mathcal{B}\mathcal{B}\Omega})$ and $\lambda(\cdot), \mu(\cdot) \in C^2(\overline{\Omega \cup \mathcal{B}\mathcal{B}\Omega})$, then there exists $\overline{\delta} > 0$ such that for any $0 < \delta \leq \overline{\delta}$, $|\mathcal{L}_{H0}\mathbf{u}(\mathbf{x}) - \mathcal{L}_{H\delta}\mathbf{u}(\mathbf{x})| \leq C\delta^2$ for $\mathbf{x} \in \Omega$. Here the generic constant C is independent of δ but may depend on the C^4 norm of \mathbf{u} .

With above regularity assumptions on u_0 and $\lambda(\cdot)$, $\mu(\cdot)$, we now further investigate the convergence of $||u_{\delta} - u_0||_{L^2}$, with detailed proof provided in Appendix A.3:

Theorem 2. Let \mathbf{u}_{δ} be the weak solution to the nonlocal problem and \mathbf{u}_{0} be the weak solution to the local problem. Assume that $\lambda(\cdot)$, $\mu(\cdot) \in C(\overline{\Omega \cup \mathcal{BB}\Omega})$. Then for any $\mathbf{f} \in (S_{H\delta}(\Omega))^*$, the dual space of $S_{H\delta}(\Omega)$, we have

$$\|u_{\delta}\|_{S_{H\delta}(\Omega)} \le \frac{\|f\|_{(S_{H\delta}(\Omega))^*}}{r}.$$
 (2.13)

In addition, if $\|f\|_{(S_{H\delta}(\Omega))^*}$ is uniformly bounded for all $\delta \in (0, \overline{\delta})$ for some positive constant $\overline{\delta} > 0$, then the nonlocal and local problems are compatible as $\delta \to 0$:

$$\lim_{\delta\to 0} ||\boldsymbol{u}_{\delta} - \boldsymbol{u}_{0}||_{L^{2}(\Omega;\mathbb{R}^{d})} = 0.$$

The next theorem characterizes the rate of convergence of u_{δ} to u_0 as $\delta \to 0$ when additional regularity is assumed for u_0 .

² We note that it is generally not necessary to have the local solution u defined in $\mathcal{BB}\Omega$. When Ω is a Lipschitz domain, the above bounds can also be obtained for the general $u \in C^4(\overline{\Omega})$, since one can extend u to a C^4 function \hat{u} in \mathbb{R}^d (see, e.g., [90, Section 2.5]). For further discussions on applying Dirichlet-type boundary conditions as an extended local solution, we refer interested readers to [65].

Theorem 3. Let \mathbf{u}_{δ} be the weak solution to the nonlocal problem and \mathbf{u}_{0} the weak solution to the local problem. In addition, we assume that $\mathbf{u}_{0} \in C^{4}(\overline{\Omega \cup \mathcal{B}\mathcal{B}\Omega})$ and $\lambda(\cdot)$, $\mu(\cdot) \in C^{2}(\overline{\Omega \cup \mathcal{B}\mathcal{B}\Omega})$. Then there exists $\overline{\delta} > 0$ such that for any $0 < \delta < \overline{\delta}$, we have

$$\|\mathbf{u}_0 - \mathbf{u}_\delta\|_{S_{H\delta}(\Omega)} \leq C\delta^2$$
,

where the generic constant C is independent of δ but may depend on the C^4 norm of u_0 .

Proof. Since u_0 is defined on $\Omega \cup \mathcal{BB}\Omega$, then we can compute $-\mathcal{L}_{H\delta}u_0(x)$ for any $x \in \Omega$. Let $f_{\delta}(x) = -\mathcal{L}_{H\delta}u_0(x)$, then we have $-e_{\delta}(x) = -\mathcal{L}_{H\delta}(u_{\delta} - u_0)(x) = \mathcal{L}_{H\delta}(u_0)(x) - \mathcal{L}_{H0}(u_0)(x) = f(x) - f_{\delta}(x)$ for $x \in \Omega$. From the truncation error analysis in Lemma 5, we get $||f - f_{\delta}||_{L^{\infty}(\Omega,\mathbb{R}^d)} = O(\delta^2)$. Since $u_{\delta} - u_0$ is the weak solution to the nonlocal problem with load vector $f - f_{\delta}$, we can use (2.13) to get

$$\|\mathbf{u}_0 - \mathbf{u}_\delta\|_{S_{H\delta}(\Omega)} \le C\|f - f_\delta\|_{L^2(\Omega,\mathbb{R}^d)} \le C\|f - f_\delta\|_{L^\infty(\Omega,\mathbb{R}^d)} = O(\delta^2).$$

2.2. Parametric peridynamics problem

In this section, we will consider the case where the material properties λ and μ are provided by random fields $\lambda(x,\omega)$ and $\mu(x,\omega)$, where $\omega\in\Omega_p$ and Ω_p is the sample space of a probability space $(\Omega_p,\mathcal{F},\mathcal{P})$. Here, \mathcal{F} is the σ -algebra of subsets of Ω_p and \mathcal{P} is the probability measure. Following the practice in [45], we represent this random field in a "truncated" form using a limited number of random variables, either because they have been approximated by a truncated expansion such as the Karhunen–Loeve expansion or through PCA (see Section 5), or because the input itself is defined in terms of a finite number of random variables. Thus, the material parameters can be rewritten as $\lambda(x,\xi)$ and $\mu(x,\xi)$, where $\xi=(\xi_{(1)},\xi_{(2)},\ldots,\xi_{(N)})$, N is a positive integer which denotes the dimension of the parametric space, and $\xi_{(i)}$ are random variables, and we assume they are independent and identically distributed (i.i.d.) random variables. Under this setting, we consider

$$\lambda(\mathbf{x}, \boldsymbol{\xi}) : (\Omega \cup \mathcal{B}\mathcal{B}\Omega) \times \Gamma \to \mathbb{R}, \quad \mu(\mathbf{x}, \boldsymbol{\xi}) : (\Omega \cup \mathcal{B}\mathcal{B}\Omega) \times \Gamma \to \mathbb{R},$$

where Γ is the space of $\boldsymbol{\xi}$ and it is typically called random space or parametric space. Without loss of generality, here we assume that $\Gamma = \prod_{i=1}^N \Gamma_i \subset \mathbb{R}^N$ where $\Gamma_i = [-1,1]$, and the random variable $\boldsymbol{\xi} \in \Gamma$ has a probability density $\rho : \Gamma \to \mathbb{R}^+$. Similar as in the deterministic problem, for each $\boldsymbol{\xi} \in \Gamma$, we use harmonic means of λ and μ to model averaged material properties:

$$\frac{2}{\mu(x,y,\xi)} = \frac{1}{\mu(x,\xi)} + \frac{1}{\mu(y,\xi)}, \quad \frac{2}{\lambda(x,y,\xi)} = \frac{1}{\lambda(x,\xi)} + \frac{1}{\lambda(y,\xi)}.$$
 (2.14)

We are then interested in solving the family of heterogeneous peridynamic problems given by

$$\begin{cases}
\mathcal{L}_{H\delta}\boldsymbol{u} := -\int_{B_{\delta}(\boldsymbol{x})} \left(\lambda(\boldsymbol{x}, \boldsymbol{y}, \boldsymbol{\xi}) - \mu(\boldsymbol{x}, \boldsymbol{y}, \boldsymbol{\xi})\right) K(|\boldsymbol{y} - \boldsymbol{x}|) \left(\boldsymbol{y} - \boldsymbol{x}\right) \left(\boldsymbol{\theta}(\boldsymbol{x}, \boldsymbol{\xi}) + \boldsymbol{\theta}(\boldsymbol{y}, \boldsymbol{\xi})\right) d\boldsymbol{y} \\
-8 \int_{B_{\delta}(\boldsymbol{x})} \mu(\boldsymbol{x}, \boldsymbol{y}, \boldsymbol{\xi}) K(|\boldsymbol{y} - \boldsymbol{x}|) \frac{(\boldsymbol{y} - \boldsymbol{x}) \otimes (\boldsymbol{y} - \boldsymbol{x})}{|\boldsymbol{y} - \boldsymbol{x}|^2} \left(\boldsymbol{u}(\boldsymbol{y}, \boldsymbol{\xi}) - \boldsymbol{u}(\boldsymbol{x}, \boldsymbol{\xi})\right) d\boldsymbol{y} = \boldsymbol{f}(\boldsymbol{x}), & \text{for } \boldsymbol{x} \in \Omega, \\
\theta(\boldsymbol{x}, \boldsymbol{\xi}) = \int_{B_{\delta}(\boldsymbol{x})} K(|\boldsymbol{y} - \boldsymbol{x}|) (\boldsymbol{y} - \boldsymbol{x}) \cdot \left(\boldsymbol{u}(\boldsymbol{y}, \boldsymbol{\xi}) - \boldsymbol{u}(\boldsymbol{x}, \boldsymbol{\xi})\right) d\boldsymbol{y}, & \text{for } \boldsymbol{x} \in \Omega \cup \mathcal{B}\Omega, \\
\boldsymbol{u}(\boldsymbol{x}, \boldsymbol{\xi}) = \boldsymbol{u}_D(\boldsymbol{x}, \boldsymbol{\xi}), & \text{for } \boldsymbol{x} \in \mathcal{B}\mathcal{B}\Omega.
\end{cases}$$

$$(2.15)$$

For each $\xi \in \Gamma$, we assume the uniform boundedness of the material properties, i.e.,

$$\begin{split} 0 < \lambda_0 &= \inf_{\boldsymbol{x} \in \Omega \cup \mathcal{B} \mathcal{B} \Omega} \lambda(\boldsymbol{x}, \boldsymbol{\xi}) \leq \sup_{\boldsymbol{x} \in \Omega \cup \mathcal{B} \mathcal{B} \Omega} \lambda(\boldsymbol{x}, \boldsymbol{\xi}) = \lambda_\infty < \infty, \\ 0 < \mu_0 &= \inf_{\boldsymbol{x} \in \Omega \cup \mathcal{B} \mathcal{B} \Omega} \mu(\boldsymbol{x}, \boldsymbol{\xi}) \leq \sup_{\boldsymbol{x} \in \Omega \cup \mathcal{B} \mathcal{B} \Omega} \mu(\boldsymbol{x}, \boldsymbol{\xi}) = \mu_\infty < \infty, \end{split}$$

for $\xi \in \Gamma$, and λ_0 , λ_∞ , μ_0 , μ_∞ satisfy Assumption 1. Therefore, for each $\xi \in \Gamma$, the conditions for Theorem 1 still hold and therefore the Lax–Milgram theorem ensures the well-posedness of the corresponding peridynamic problem. In addition, in order to consider the limit $\delta \to 0$, we need to assume that for each $\xi \in \Gamma$ and $x \in \Omega \cup \mathcal{BB}\Omega$,

$$\lambda(\cdot, \xi), \, \mu(\cdot, \xi) \in C(\overline{\Omega \cup \mathcal{B}\mathcal{B}\Omega}). \tag{2.16}$$

Then we have the corresponding family of local linear elastic problem for each $\xi \in \Gamma$:

$$\begin{cases} \mathcal{L}_{H0}u(x,\xi) := -(\lambda(x,\xi) - \mu(x,\xi))\nabla[\operatorname{tr}(\mathbf{E}(x,\xi))] - \mu(x,\xi)\nabla\cdot(2\mathbf{E}(x,\xi) + \operatorname{tr}(\mathbf{E}(x,\xi))\mathbf{I}) = f(x), & \text{in } \Omega, \\ u(x,\xi) = u_D(x,\xi), & \text{in } \mathcal{BB}\Omega. \end{cases}$$

$$(2.17)$$

For each given parameter $\xi \in \Gamma$, we denote the solution to the peridynamic problem (2.15) by $u_{\delta}(x, \xi)$ and the solution to the corresponding local equation (2.17) by $u_0(x, \xi)$. A corollary of Theorem 2 is that $u_{\delta}(x, \xi)$ converges to $u_0(x, \xi)$ in the space $L^2(\Omega) \otimes L^2_{\varrho}(\Gamma)$ as $\delta \to 0$:

Corollary 1. Let $u_{\delta}(x, \xi)$ be the weak solution to (2.15) and $u_{0}(x, \xi)$ the weak solution to (2.17). Assume that $\lambda(\cdot, \xi)$, $\mu(\cdot, \xi) \in C(\overline{\Omega \cup \mathcal{BB}\Omega})$, then there exists $\overline{\delta} > 0$ such that for any $0 < \delta < \overline{\delta}$, we have

$$\lim_{\delta \to 0} \| \boldsymbol{u}_{\delta} - \boldsymbol{u}_{0} \|_{L^{2}(\Omega; \mathbb{R}^{d}) \otimes L^{2}_{\rho}(\Gamma)} = 0.$$

In addition, if we have $\mathbf{u}_0(\cdot, \boldsymbol{\xi}) \in C^4(\overline{\Omega \cup \mathcal{B}\mathcal{B}\Omega})$ with uniform C^4 norm for $\boldsymbol{\xi} \in \Gamma$ and $\lambda(\cdot, \boldsymbol{\xi}), \mu(\cdot, \boldsymbol{\xi}) \in C^2(\overline{\Omega \cup \mathcal{B}\mathcal{B}\Omega})$, then

$$\|\boldsymbol{u}_{\delta} - \boldsymbol{u}_{0}\|_{S_{H\delta}(\Omega) \otimes L_{2}^{2}(\Gamma)} \leq C\delta^{2},$$

where the generic constant C is independent of δ but may depend on the C^4 norm of u_0 .

Proof. For any $\boldsymbol{\xi} \in \Gamma$, and, we know from Theorem 2 that $\|\boldsymbol{u}_{\delta}(\cdot,\boldsymbol{\xi})\|_{S_{H\delta}(\Omega)} \leq C$ for all $\delta \in (0,\overline{\delta})$ and $\|\boldsymbol{u}_{\delta}(\cdot,\boldsymbol{\xi}) - \boldsymbol{u}_{0}(\cdot,\boldsymbol{\xi})\|_{L^{2}(\Omega;\mathbb{R}^{d})} \to 0$ as $\delta \to 0$. Therefore, it is easy to see that $\|\boldsymbol{u}_{\delta}(\cdot,\boldsymbol{\xi}) - \boldsymbol{u}_{0}(\cdot,\boldsymbol{\xi})\|_{L^{2}(\Omega;\mathbb{R}^{d})} \leq C$ for all $\boldsymbol{\xi} \in \Gamma$ and $\delta \in (0,\overline{\delta})$. Using the dominated convergence theorem, we have

$$\|\boldsymbol{u}_{\delta}-\boldsymbol{u}_{0}\|_{L^{2}(\Omega;\mathbb{R}^{d})\otimes L^{2}_{\rho}(\Gamma)}=\int_{\Gamma}\|\boldsymbol{u}_{\delta}(\cdot,\boldsymbol{\xi})-\boldsymbol{u}_{0}(\cdot,\boldsymbol{\xi})\|_{L^{2}(\Omega;\mathbb{R}^{d})}^{2}\rho(\boldsymbol{\xi})d\boldsymbol{\xi}\overset{\delta\to 0}{\longrightarrow}0.$$

The second statement comes from Theorem 3 by noticing that $\|u_0(\cdot, \xi)\|_{C^4(\overline{\Omega \cup BB\Omega})} \le C$ for all $\xi \in \Gamma$. \square

2.3. Peridynamics formulation for brittle fractures

One of the main appeals of peridynamics is to handle fracture problems, where free surfaces are associated with the evolution of a fracture surface. In this section, we first consider the deterministic LPS model and propose the handling of free surfaces in heterogeneous materials, then apply it to the treatment of material fractures. Lastly, we will conclude this section with a stochastic LPS formulation for evolving fractures.

We now consider general mixed boundary conditions: $\partial \Omega = \partial \Omega_D \bigcup \bar{\partial} \Omega_N$ and $(\partial \Omega_D)^o \bigcap (\partial \Omega_N)^o = \emptyset$. Here $\partial \Omega_D$ and $\partial \Omega_N$ are both curves. To apply the nonlocal Dirichlet-type boundary condition, we assume that $u(x) = u_D(x)$ are provided in a layer with non-zero volume outside Ω , while the free surface boundary condition is applied on the sharp interface $\partial \Omega_N$. To define a Dirichlet-type constraint, we denote

$$\mathcal{I}\Omega_D := \{ \boldsymbol{x} \in \Omega | \operatorname{dist}(\boldsymbol{x}, \partial \Omega_D) < \delta \}, \ \mathcal{B}\Omega_D := \{ \boldsymbol{x} \notin \Omega | \operatorname{dist}(\boldsymbol{x}, \partial \Omega_D) < \delta \}, \ \mathcal{B}\mathcal{B}\Omega_D := \{ \boldsymbol{x} \notin \Omega | \operatorname{dist}(\boldsymbol{x}, \partial \Omega_D) < 2\delta \},$$

and assume that the value of \mathbf{u} is given on $\mathcal{BB}\Omega_D$. For notation simplicity, we denote $\Omega_D := \Omega \cup \mathcal{BB}\Omega_D$. Similarly, to apply the free surface boundary condition, we denote

$$\mathcal{I}\Omega_N := \{ \mathbf{x} \in \Omega | \operatorname{dist}(\mathbf{x}, \partial \Omega_N) < \delta \}, \ \mathcal{B}\Omega_N := \{ \mathbf{x} \notin \Omega | \operatorname{dist}(\mathbf{x}, \partial \Omega_N) < \delta \}, \ \mathcal{B}\mathcal{B}\Omega_N := \{ \mathbf{x} \notin \Omega | \operatorname{dist}(\mathbf{x}, \partial \Omega_N) < 2\delta \}.$$

Unless stated otherwise, in this paper we further assume sufficient regularity in the boundary that we may take δ sufficiently small so that for any $\mathbf{x} \in \mathcal{I}\Omega$, there exists a unique orthogonal projection³ of \mathbf{x} onto $\partial \Omega$, which is the closest point on $\partial \Omega$ to \mathbf{x} . We denote this projection as $\overline{\mathbf{x}}$. Therefore, one has $\overline{\mathbf{x}} - \mathbf{x} = s_x \mathbf{n}(\mathbf{x})$ for $\mathbf{x} \in \mathcal{I}\Omega_N$, where $0 < s_x < \delta$. Here \mathbf{n} denotes the normal direction pointing out of the domain for each $\mathbf{x} \in \mathcal{I}\Omega_N$, and let \mathbf{p} denote the tangential direction. Here, we propose the following formulation for the (partially) free surface

³ Here we notice that it is possible $\mathcal{I}\Omega_D \cap \mathcal{I}\Omega_N \neq \emptyset$. In our numerical solver, we treat x with the Dirichlet-type boundary condition if the projection of x is in $\partial \Omega_D$. Otherwise, we use the Neumann-type boundary condition at x.

problem:

$$\mathcal{L}_{N\delta}\boldsymbol{u}(\boldsymbol{x}) := -\int_{B_{\delta}(\boldsymbol{x})\cap\Omega_{D}} (\lambda(\boldsymbol{x},\boldsymbol{y}) - \mu(\boldsymbol{x},\boldsymbol{y})) K(|\boldsymbol{y}-\boldsymbol{x}|) (\boldsymbol{y}-\boldsymbol{x}) \left(\theta^{corr}(\boldsymbol{x}) + \theta^{corr}(\boldsymbol{y})\right) d\boldsymbol{y}
-8 \int_{B_{\delta}(\boldsymbol{x})\cap\Omega_{D}} \mu(\boldsymbol{x},\boldsymbol{y}) K(|\boldsymbol{y}-\boldsymbol{x}|) \frac{(\boldsymbol{y}-\boldsymbol{x})\otimes(\boldsymbol{y}-\boldsymbol{x})}{|\boldsymbol{y}-\boldsymbol{x}|^{2}} (\boldsymbol{u}(\boldsymbol{y}) - \boldsymbol{u}(\boldsymbol{x})) d\boldsymbol{y}
-2\theta^{corr}(\boldsymbol{x}) \int_{B_{\delta}(\boldsymbol{x})\setminus\Omega_{D}} (\lambda(\boldsymbol{x},\boldsymbol{y}) - \mu(\boldsymbol{x},\boldsymbol{y})) K(|\boldsymbol{y}-\boldsymbol{x}|) (\boldsymbol{y}-\boldsymbol{x}) d\boldsymbol{y}
-4\theta^{corr}(\boldsymbol{x}) \int_{B_{\delta}(\boldsymbol{x})\setminus\Omega_{D}} (\lambda(\boldsymbol{x},\boldsymbol{y}) + 2\mu(\boldsymbol{x},\boldsymbol{y})) K(|\boldsymbol{y}-\boldsymbol{x}|) \frac{[(\boldsymbol{y}-\boldsymbol{x})\cdot\mathbf{n}][(\boldsymbol{y}-\boldsymbol{x})\cdot\mathbf{p}]^{2}}{|\boldsymbol{y}-\boldsymbol{x}|^{2}} \mathbf{n} d\boldsymbol{y}
+4\theta^{corr}(\boldsymbol{x}) \int_{B_{\delta}(\boldsymbol{x})\setminus\Omega_{D}} \lambda(\boldsymbol{x},\boldsymbol{y}) K(|\boldsymbol{y}-\boldsymbol{x}|) \frac{[(\boldsymbol{y}-\boldsymbol{x})\cdot\mathbf{n}]^{3}}{|\boldsymbol{y}-\boldsymbol{x}|^{2}} \mathbf{n} d\boldsymbol{y} = \boldsymbol{f}(\boldsymbol{x}), \tag{2.18}$$

and

$$\theta^{corr}(\mathbf{x}) = \int_{B_{\delta}(\mathbf{x}) \cap \Omega_D} K(|\mathbf{y} - \mathbf{x}|) (\mathbf{y} - \mathbf{x}) \cdot \mathbf{M}(\mathbf{x}) \cdot (\mathbf{u}(\mathbf{y}) - \mathbf{u}(\mathbf{x})) d\mathbf{y}, \tag{2.19}$$

$$\mathbf{M}(\mathbf{x}) = \left[\int_{B_{\delta}(\mathbf{x}) \cap \Omega_D} K(|\mathbf{y} - \mathbf{x}|) (\mathbf{y} - \mathbf{x}) \otimes (\mathbf{y} - \mathbf{x}) d\mathbf{y} \right]^{-1}.$$
 (2.20)

Here we notice that for $\mathbf{x} \notin \mathcal{I}\Omega_N$, $\mathbf{M}(\mathbf{x})$ coincides with the identity matrix and hence $\theta^{corr} = \theta$. Therefore, the nonlocal operator $\mathcal{L}_{N\delta}$ in (2.18) is the same as $\mathcal{L}_{H\delta}$ for $\mathbf{x} \in \Omega \backslash \mathcal{I}\Omega_N$. That means, for material points which are sufficiently far away from the free surface, we obtain the momentum balance and nonlocal dilatation formulation (2.5). On the other hand, when considering homogeneous materials, i.e., when $\lambda(\mathbf{x}) = \lambda$ and $\mu(\mathbf{x}) = \mu$ are constants, we obtain the Neumann-type LPS formulation developed in [34], which as shown to provide an approximation for the corresponding linear elastic model with free surfaces in the case of linear displacement fields.

With the free surface formulation, we now employ the composite LPS model (2.5) and extend it to model brittle fracture in the general heterogeneous materials. In peridynamics, material damage is incorporated into the constitutive model by allowing the bonds of material points to break irreversibly. To model brittle fracture in the LPS model, we employ the critical stretch criterion where breakage occurs when a bond is extended beyond some predetermined critical bond deformed length [34,91]. Although a similar idea can be applied for dynamic fracture problems [34], in this work we consider quasi-static fracture problems, and use the time instant t to denote the indexes for (incrementally increasing) loading in quasi-static problems. For example, the displacement solution at time instant t will be denoted as u(x, t). Consider the case where the material properties λ , μ and the fracture energy G are provided by random fields $\lambda(x, \xi)$, $\mu(x, \xi)$ and $G(x, \xi)$, where we recall that $\xi = (\xi_{(1)}, \xi_{(2)}, \dots, \xi_{(N)})$, with $N \in \mathbb{N}$ being the dimension of the parametric space, and $\xi_{(i)}$ are i.i.d. random variables. We propose the following formulation for $x \in \Omega$

$$\mathcal{L}_{F\delta} u(x, t, \xi) := -\int_{B_{\delta}(x)} \gamma(x, y, t, \xi) \left(\lambda(x, y, \xi) - \mu(x, y, \xi)\right) K(|y - x|) \left(y - x\right) \left(\theta^{corr}(x, t, \xi) + \theta^{corr}(y, t, \xi)\right) dy \\
- 8 \int_{B_{\delta}(x)} \gamma(x, y, t, \xi) \mu(x, y, \xi) K(|y - x|) \frac{(y - x) \otimes (y - x)}{|y - x|^2} \left(u(y, t, \xi) - u(x, t, \xi)\right) dy \\
- 2 \theta^{corr}(x, t, \xi) \int_{B_{\delta}(x)} (1 - \gamma(x, y, t, \xi)) \left(\lambda(x, y, \xi) - \mu(x, y, \xi)\right) K(|y - x|) (y - x) dy \\
- 4 \theta^{corr}(x, t, \xi) \int_{B_{\delta}(x)} (1 - \gamma(x, y, t, \xi)) (\lambda(x, y, \xi) + 2\mu(x, y, \xi)) K(|y - x|) \frac{[(y - x) \cdot \mathbf{n}][(y - x) \cdot \mathbf{p}]^2}{|y - x|^2} \mathbf{n} dy \\
+ 4 \theta^{corr}(x, t, \xi) \int_{B_{\delta}(x)} (1 - \gamma(x, y, t, \xi)) \lambda(x, y, \xi) K(|y - x|) \frac{[(y - x) \cdot \mathbf{n}]^3}{|y - x|^2} \mathbf{n} dy = f(x, t), \tag{2.21}$$

and for $x \in \Omega \cup \mathcal{B}\Omega_D$

$$\theta^{corr}(\boldsymbol{x},t,\boldsymbol{\xi}) = \int_{B_{S}(\boldsymbol{x})} \gamma(\boldsymbol{x},\boldsymbol{y},t,\boldsymbol{\xi}) K(|\boldsymbol{y}-\boldsymbol{x}|) (\boldsymbol{y}-\boldsymbol{x}) \cdot \mathbf{M}(\boldsymbol{x},t,\boldsymbol{\xi}) \cdot (\boldsymbol{u}(\boldsymbol{y},t,\boldsymbol{\xi}) - \boldsymbol{u}(\boldsymbol{x},t,\boldsymbol{\xi})) d\boldsymbol{y}, \tag{2.22}$$

$$\mathbf{M}(\mathbf{x}, t, \boldsymbol{\xi}) = \left[\int_{B_{\delta}(\mathbf{x})} \gamma(\mathbf{x}, \mathbf{y}, t, \boldsymbol{\xi}) K(|\mathbf{y} - \mathbf{x}|) (\mathbf{y} - \mathbf{x}) \otimes (\mathbf{y} - \mathbf{x}) d\mathbf{y} \right]^{-1}, \tag{2.23}$$

where the averaged two-point functions $\mu(\cdot, \cdot, \xi)$, $\lambda(\cdot, \cdot, \xi)$ are defined using the harmonic mean, following (2.14). The boolean state function $\gamma(x, y, t, \xi)$ is defined and updated following

$$\gamma(\boldsymbol{x}, \boldsymbol{y}, t, \boldsymbol{\xi}) = \begin{cases} 1, & \text{if } s(\boldsymbol{x}, \boldsymbol{y}, \tau, \boldsymbol{\xi}) \leq s_0(\boldsymbol{x}, \boldsymbol{y}, \boldsymbol{\xi}), \ \forall \tau \leq t, \ \text{and} \ \boldsymbol{y} \in B_{\delta}(\boldsymbol{x}) \cap \Omega_D, \\ 0, & \text{otherwise}, \end{cases}$$
 (2.24)

with the associated strain s and the critical bond stretch s_0 related to material parameters:

$$s(x, y, t, \xi) := \frac{\|u(y, t, \xi) - u(x, t, \xi) + y - x\| - \|y - x\|}{\|y - x\|},$$

$$s_0(x, y, \xi) := \sqrt{\frac{G(x, y)}{4(\lambda(x, y, \xi) - \mu(x, y, \xi))\beta' + 8\mu(x, y, \xi)\beta}}, \text{ where } \beta := \frac{3\delta}{4\pi}, \ \beta' := 0.23873\delta.$$
 (2.25)

Here $G(x, y, \xi)$ is the averaged fracture energy defined via the arithmetic mean:

$$G(x, y, \xi) = \frac{1}{2}(G(x, \xi) + G(y, \xi)). \tag{2.26}$$

To summarize, for each $\xi \in \Gamma$, we obtain a unified mathematical formulation for a (quasi)-static state-based peridynamic problem with general mixed boundary conditions for brittle fractures:

$$\begin{cases}
\mathcal{L}_{F\delta}\boldsymbol{u}(\boldsymbol{x},t,\boldsymbol{\xi}) = f(\boldsymbol{x},t), & \text{in } \Omega \\
\theta^{corr}(\boldsymbol{x},t,\boldsymbol{\xi}) = \int_{B_{\delta}(\boldsymbol{x})} \gamma(\boldsymbol{x},\boldsymbol{y},t,\boldsymbol{\xi}) K(|\boldsymbol{y}-\boldsymbol{x}|) (\boldsymbol{y}-\boldsymbol{x})^T \mathbf{M}(\boldsymbol{x},t,\boldsymbol{\xi}) (\boldsymbol{u}(\boldsymbol{y},t,\boldsymbol{\xi}) - \boldsymbol{u}(\boldsymbol{x},t,\boldsymbol{\xi})) \, d\boldsymbol{y}, & \text{in } \Omega \cup \mathcal{B}\Omega_D \\
\boldsymbol{u}(\boldsymbol{x},t,\boldsymbol{\xi}) = \boldsymbol{u}_D(\boldsymbol{x},t,\boldsymbol{\xi}), & \text{in } \mathcal{B}\mathcal{B}\Omega_D
\end{cases}$$
(2.27)

Remark 2. To see the intuition for the averaged material properties definition in (2.14) and the averaged fracture energy definition in (2.26), we take the interaction between x and y as an analog of a series of two springs connecting the two points. Assuming that the two springs are with elongation lengths l_1 and l_2 , respectively, and their spring constants are k_1 and k_2 , respectively. We notice that l_1 and l_2 can be seen as the analog of the bond elongation in peridynamics, i.e., u(y) - u((x + y)/2) and u((x + y)/2) - u(x), respectively, and k_1 , k_2 can be seen as the analog of material properties. Then the force balance between x, y yields $k_1l_1 = k_2l_2$ and therefore the equivalent strength of this bond would be $k = \frac{k_1l_1 + k_2l_2}{l_1 + l_2} = \frac{2}{k_1^{-1} + k_2^{-1}}$, which can be viewed as a simplified version of the harmonic mean formulation for the averaged material properties definition in (2.14). On the other hand, the total energy of the spring series writes $\frac{1}{2}(k_1l_1^2 + k_2l_2^2)$, hence we define the averaged fracture energy via the arithmetic mean, as shown in (2.26).⁴

3. Spatial and stochastic numerical methods

In this section, we firstly introduce a strong form of meshfree discretization for the stochastic LPS model. Specifically, the optimization-based quadrature rule [33,34,45] will be employed for spatial discretization, which is simple to implement and generally faster [62,63], and was shown to be asymptotically compatible with corresponding local solutions in the absence of fracture [34]. To sample the random field, the probabilistic collocation method (PCM) is employed, for its high accuracy and ease of implementation by sampling at discrete points in a random space [73,93,94]. Of course, the main appeal of peridynamic discretizations is to handle fracture problems. Therefore, we will also demonstrate how the meshfree scheme adapts to the brittle fracture formulation described in Section 2.3, where free surfaces are associated with the time evolution of a fracture surface. Finally, the fully-discretized formulation for the heterogeneous LPS model with random microstructure will be

⁴ We note that in some studies the harmonic mean formulation is employed for the averaged fracture energy (see [47] and references therein), which would make the interfacial bonds relatively weaker than what we proposed here. However, as studied in [92], in bimaterial problems the interfacial bond strength depends on the interfacial adhesion strength, which should be provided by experiments. Therefore, without further measurements from experiments, we employ the arithmetic mean definition here since it provides a better agreement of fracture toughness with experimental measurements in Section 5.

considered. In absence of fracture and assuming that the solution possesses sufficient continuity, we show that the proposed formulation sustains the asymptotic compatibility spatially and achieves an algebraic or sub-exponential convergence rate in the random coefficients space as the number of collocation points grows. When fractures occur, our formulation automatically provides a sharp representation of the fracture surface by breaking bonds for each microstructure, and then estimates of quantities of interest in heterogeneous material damage problems, such as the fracture toughness, can be obtained.

3.1. Spatial: Optimization-based meshfree quadrature rules

Discretizing the whole interaction region $\Omega \cup \mathcal{BB}\Omega$ by a collection of points $\chi_h = \{x_i\}_{\{i=1,2,\dots,M\}} \subset \Omega \cup \mathcal{BB}\Omega$, we aim to solve for the displacement $u_i \approx u(x_i)$ and nonlocal dilatation $\theta_i \approx \theta(x_i)$ on each $x_i \in \chi_h$. Recall the definitions [95] of fill distance $h_{\chi_h,\Omega} = \sup_{x_i \in \Omega \cup \mathcal{BB}\Omega} \min_{x_j \in \chi_h} \|x_i - x_j\|_2$ and separation distance $q_{\chi_h} = \frac{1}{2} \min_{i \neq j} \|x_i - x_j\|_2$. For simplicity we drop subscripts and simply write h and q. In this paper we assume that χ_h is *quasi-uniform*, namely

For simplicity we drop subscripts and simply write h and q. In this paper we assume that χ_h is *quasi-uniform*, namely that there exists $c_{qu} > 0$ such that $q_{\chi_h} \le h_{\chi_h,\Omega} \le c_{qu}q_{\chi_h}$. To maintain an easily scalable implementation, we further assume δ to be chosen such that the ratio $\frac{h}{\delta}$ is bounded as $\delta \to 0$, restricting ourselves to the " δ -convergence" scenario [64].

Following [34], for materials without fracture we then pursue a discretization in 2D space of the system (2.2) and (2.3) through the following one point quadrature rule at χ_h [96]:

$$(\mathcal{L}_{H\delta}^{h}\boldsymbol{u})_{i} := \sum_{\boldsymbol{x}_{j} \in \chi_{h} \cap B_{\delta}(\boldsymbol{x}_{i})} (\lambda_{ij} - \mu_{ij}) K_{ij} (\boldsymbol{x}_{j} - \boldsymbol{x}_{i}) (\theta_{i} + \theta_{j}) \omega_{j,i}$$

$$(3.1)$$

$$+8\sum_{\mathbf{x}_{j}\in\chi_{h}\cap B_{\delta}(\mathbf{x}_{i})}\mu_{ij}K_{ij}\frac{\left(\mathbf{x}_{j}-\mathbf{x}_{i}\right)\otimes\left(\mathbf{x}_{j}-\mathbf{x}_{i}\right)}{\left|\mathbf{x}_{j}-\mathbf{x}_{i}\right|^{2}}\left(\mathbf{u}_{i}-\mathbf{u}_{j}\right)\omega_{j,i}=\mathbf{f}_{i},$$

$$\theta_{i}:=\sum_{\mathbf{x}_{j}\in\chi_{h}\cap B_{\delta}(\mathbf{x}_{i})}K_{ij}(\mathbf{x}_{j}-\mathbf{x}_{i})\cdot\left(\mathbf{u}_{j}-\mathbf{u}_{i}\right)\omega_{j,i},$$

$$(3.2)$$

where we adopt notations $q_i = q(\mathbf{x}_i)$, $q_{ij} = q(\mathbf{x}_i, \mathbf{x}_j)$ for generic functions q. $\{\omega_{j,i}\}_{\mathbf{x}_j \in B_\delta(\mathbf{x}_i)}$ is a collection of to-bedetermined quadrature weights corresponding to a neighborhood of collocation point \mathbf{x}_i , which will be constructed through an optimization-based approach in [45] to ensure consistency guarantees. Specifically, we seek quadrature weights for integrals supported on balls of the form

$$I[q] := \int_{B_{\delta}(\mathbf{x}_i)} q(\mathbf{x}_i, \mathbf{y}) d\mathbf{y} \approx I_h[q] := \sum_{\mathbf{x}_j \in \chi_h \cap B_{\delta}(\mathbf{x}_i) \setminus \{\mathbf{x}_i\}} q(\mathbf{x}_i, \mathbf{x}_j) \omega_{j,i}$$
(3.3)

where the subscript i in $\{\omega_{j,i}\}$ denotes that we seek a different family of quadrature weights for different subdomains $B_{\delta}(x_i)$. These weights are then generated from the following optimization problem

$$\underset{\{\omega_{j,i}\}}{\operatorname{argmin}} \sum_{x_i \in \chi_h \cap B_\delta(x_i) \setminus \{x_i\}} \omega_{j,i}^2 \quad \text{such that,} \quad I_h[q] = I[q] \quad \forall q \in V_{h,x_i}, \tag{3.4}$$

where $V_{h,x_i} = \left\{q(y-x_i) = \frac{p(y-x_i)}{|y-x_i|^3} \middle| p \in \mathbb{P}_5(\mathbb{R}^d) \text{ such that } \int_{B_\delta(x_i)} q(y-x_i) dy < \infty \right\}$ denotes the space of functions which should be integrated exactly. $\mathbb{P}_m(\mathbb{R}^d)$ is the space of mth order polynomials. As shown in [34], for $u_0 \in C^4(\overline{\Omega \cup \mathcal{BB\Omega}})$ this particular choice of reproducing space guarantees that the truncation error for all nonlocal operators in (2.2) with respect to the local limit converges with an $O(\delta^2)$ rate in the limit $\delta \to 0$. For further discussions and error estimates of this optimization-based quadrature rule, we refer interested readers to [45].

3.2. Stochastic: Probabilistic collocation method with sparse grids

In this work, we use the probabilistic collocation method (PCM) in the parametric space to solve the parametric peridynamics problem [73,93,94]. Consider the stochastic LPS Problem (2.15), PCM can be seen as a Lagrange interpolation in the random space. In particular, let $\Theta_N = \{\xi_k\}_{k=1}^Q \subset \Gamma$ be a set of prescribed nodes such that the Lagrange interpolation in the random space Γ is poised in an interpolation space Γ_I , where N is the dimension of the

parametric space. Then any function $v: \Gamma \to \mathbb{R}$ can be approximated using the Lagrange interpolation polynomial $\mathcal{J}[v](\boldsymbol{\xi}) = \sum_{k=1}^{Q} v(\boldsymbol{\xi}_k) J_k(\boldsymbol{\xi})$, where $J_k(\boldsymbol{\xi})$ is the Lagrange polynomial satisfying $J_k(\boldsymbol{\xi}) \in \Gamma_I$ and $J_k(\boldsymbol{\xi}_j) = \delta_{kj}$. In the PCM approach, we first solve Q deterministic nonlocal problems:

$$\begin{cases}
\mathcal{L}_{H\delta} \boldsymbol{u}(\boldsymbol{x}, \boldsymbol{\xi}_{k}) = \boldsymbol{f}(\boldsymbol{x}), & \text{in } \Omega \\
\theta(\boldsymbol{x}, \boldsymbol{\xi}_{k}) = \int_{B_{\delta}(\boldsymbol{x})} K(|\boldsymbol{y} - \boldsymbol{x}|) (\boldsymbol{y} - \boldsymbol{x})^{T} \left(\boldsymbol{u}(\boldsymbol{y}, \boldsymbol{\xi}_{k}) - \boldsymbol{u}(\boldsymbol{x}, \boldsymbol{\xi}_{k}) \right) d\boldsymbol{y}, & \text{in } \Omega \cup \mathcal{B}\Omega \\
\boldsymbol{u}(\boldsymbol{x}, \boldsymbol{\xi}_{k}) = \boldsymbol{u}_{D}(\boldsymbol{x}, \boldsymbol{\xi}_{k}), & \text{in } \mathcal{B}\Omega
\end{cases} \tag{3.5}$$

for k = 1, ..., Q, and then define the approximation solution $u^Q(x, \xi) := \sum_{k=1}^Q u(x, \xi_k) J_k(\xi)$. Note that in practice (3.5) is solved by the deterministic meshfree solver discussed in Section 3.1. Therefore, the PCM approach can be implemented in an embarrassingly parallel way and the total computational cost is the product of the number of collocation points and the cost of solving a deterministic problem.

To choose the set of prescribed collocation nodes Θ_N , in this work we consider two different strategies: the tensor products of 1D collocation point sets and a sparse grid strategy for high dimensionality. In the tensor product strategy, one first constructs a 1D interpolation for each dimension in the random space. For the *i*th dimension, we take $\varpi_{(i)}$ numbers of nodal points $\Theta_1^{\varpi_{(i)}} = \{\xi_1^i, \dots, \xi_{\varpi_{(i)}}^i\} \subset [-1, 1]$, a 1D interpolation for a smooth function v on the *i*th dimension then writes:

$$\mathcal{U}^{\varpi_{(i)}}[v](\xi_{(i)}) = \sum_{k=1}^{\varpi_{(i)}} v(\xi_k^i) J_k^i(\xi_{(i)})$$
(3.6)

where $J_k^i(\xi_{(i)})$ is the 1D Lagrange polynomial. Then for the case with high dimensionality in parametric space $v: \mathbb{R}^N \to \mathbb{R}$, the tensor product formula is:

$$\mathcal{J}[v] = (\mathcal{U}^{\varpi_{(1)}} \otimes \cdots \otimes \mathcal{U}^{\varpi_{(N)}})[v] = \sum_{k_1=1}^{\varpi_{(1)}} \cdots \sum_{k_N=1}^{\varpi_{(N)}} v\left(\xi_{k_1}^1, \dots, \xi_{k_N}^N\right) \left(J_{k_1}^1 \otimes \cdots \otimes J_{k_N}^N\right). \tag{3.7}$$

Notice here (3.7) requires $Q = \prod_{i=1}^{N} \varpi_{(i)}$ numbers of collocation points in total, which grows exponentially as N increases and makes the simulation non-feasible (see, e.g., [77]). Therefore, the tensor product strategy may be employed for problems with a small number of random dimension. For problems with a relatively large random dimension, we employ the sparse grids strategy. In particular, we employ the sparse grids constructed by the Smolyak algorithm [97], which is a linear combination of tensor product formulas:

$$\mathcal{J}[v] = \sum_{\zeta - N + 1 \le |\boldsymbol{\varpi}| \le \zeta} (-1)^{\zeta - |\boldsymbol{\varpi}|_{l_1}} \binom{N - 1}{\zeta - |\boldsymbol{\varpi}|_{l_1}} (\mathcal{U}^{\boldsymbol{\varpi}_{(1)}} \otimes \cdots \otimes \mathcal{U}^{\boldsymbol{\varpi}_{(N)}}). \tag{3.8}$$

Here ζ is the sparseness parameter, $\boldsymbol{\varpi} = (\varpi_{(1)}, \ldots, \varpi_{(N)}) \in \mathbb{N}^N$, $|\boldsymbol{\varpi}|_{l_1} = \sum_{i=1}^N \varpi_{(i)}$, and $\varpi_{(i)}$ represents the number of collocation points in random dimension i. To compute (3.8), only evaluations on the sparse grids are needed:

$$\Theta_N = \bigcup_{\zeta - N + 1 \le |\varpi|_{I_1} \le \zeta} \left(\Theta_1^{\varpi_{(1)}} \times \dots \times \Theta_1^{\varpi_{(N)}} \right). \tag{3.9}$$

As shown in [98,99], (3.8) is exact for $p(\xi) \in \mathbb{P}_{\zeta-N}(\mathbb{R}^N)$ (all polynomials of degree less than $\zeta-N$) and the total number of nodes $Q \sim \frac{2N^{\zeta-N}}{(\zeta-N)!}$. Therefore, we may see that the sparse grid formulation typically requires a much smaller number of collocation points Q than the full tensor product set and we will refer $\eta = \zeta - N$ as the "level" of the Smolyak formulation. As suggested in [77], generally the tensor product strategy is employed when the dimension of parametric space $N \leq 4$, and the Smolyak sparse grid is preferred when N > 4.

With a proper choice of Θ_N , the statistical moments of each component of the random solution can then be evaluated with the numerical solution of (3.5) on all probabilistic collocation points $\xi_k \in \Theta_N$. To numerically compute the mean and the standard deviation of any function $q(x, \xi)$ of interest, we employ the quadrature rule approximation by choosing the set Θ_N as quadrature point set:

$$\mathbb{E}[q](\mathbf{x}) \approx \sum_{k=1}^{Q} q(\mathbf{x}, \boldsymbol{\xi}_k) \mu_k, \tag{3.10}$$

$$\sigma[q](\mathbf{x}) \approx \sqrt{\sum_{k=1}^{Q} (q(\mathbf{x}, \boldsymbol{\xi}_k))^2 \mu_k - \left[\sum_{l=1}^{Q} q(\mathbf{x}, \boldsymbol{\xi}_l) \mu_l\right]^2},$$
(3.11)

where $\{\mu_k\}_{k=1}^Q$ is the set of corresponding quadrature weights.

We now investigate the approximation error of PCM in the parametric space. First, by our assumptions, $\lambda(x, y, \xi)$ and $\mu(x, y, \xi)$ are continuous in $\xi \in \Gamma$. Therefore, using similar arguments presented in the last part of Theorem 2, one can easily see that the map $u_{\delta}(\cdot, \xi) : \Gamma \mapsto S_{H\delta}(\Omega)$ is continuous, i.e., $u_{\delta} \in C(\Gamma; S_{H\delta}(\Omega))$. Next, we follow the error analysis in [100], which depends on the higher regularity of the solution with respect to the parameter $\xi \in \Gamma$. We make the following regularity assumption for the rest of this subsection.

Assumption 2 (*Regularity*). For each δ , we assume that the map $u_{\delta}(\cdot, \xi) : \Gamma \mapsto S_{H\delta}(\Omega)$ admits an analytic extension to the region $\mathcal{A}(\Gamma, \tau) := \{\hat{\xi} \in \mathbb{C}^N : \operatorname{dist}(\hat{\xi}, \Gamma) \leq \tau\}$. Moreover,

$$\max_{\hat{\boldsymbol{\xi}} \in \mathcal{A}(\Gamma, \tau)} \|\boldsymbol{u}_{\delta}(\cdot, \hat{\boldsymbol{\xi}})\|_{S_{H\delta}(\Omega; \mathbb{C}^d)} \leq C$$

for some C > 0. Note that the space $S_{H\delta}(\Omega; \mathbb{C}^d)$ is defined by

$$S_{H\delta}(\Omega; \mathbb{C}^d) := \{ \boldsymbol{u} \in L^2(\Omega; \mathbb{C}^d) : |\boldsymbol{u}|_{S_{H\delta}(\Omega; \mathbb{C}^d)}^2 := \iint_{(\Omega \cup \mathcal{BB}\Omega)^2} \frac{K(|\boldsymbol{y} - \boldsymbol{x}|)}{|\boldsymbol{y} - \boldsymbol{x}|^2} |(\boldsymbol{y} - \boldsymbol{x}) \cdot (\boldsymbol{u}(\boldsymbol{y}) - \boldsymbol{u}(\boldsymbol{x}))|^2 d\boldsymbol{y} d\boldsymbol{x} < \infty \}$$

where $|\boldsymbol{v}|^2$ is understood as $\overline{\boldsymbol{v}}\boldsymbol{v}$ for $\boldsymbol{v}:\Omega\to\mathbb{C}^d$.

In [100, Theorems 3.10–3.11], error analysis of the Smolyak sparse grids is presented for the classical linear elliptic PDEs, which is based on a fundamental result on the polynomial approximation of analytic functions. Here we present a similar result of [100, Lemma 3.2] (see also [101, Lemma 4.4]) which is the key lemma for the convergence theorem. Detailed proof can be found in Appendix A.4.

Lemma 6. Let $\Gamma^1 = [-1, 1]$ and \mathbb{P}_p denote the polynomial space of degree p. Given a function $\mathbf{v}(\mathbf{x}, t) \in C(\Gamma^1; S_{H\delta}(\Omega))$ which admits an analytic extension to the region $\mathcal{A}(\Gamma^1, \tau) = \{z \in \mathbb{C} : \operatorname{dist}(z, \Gamma^1) \leq \tau\}$ for some $\tau > 0$, then

$$\min_{\boldsymbol{w} \in \mathcal{P}_p \otimes S_{H\delta}(\Omega; \mathbb{C}^d)} \|\boldsymbol{v} - \boldsymbol{w}\|_{C(\Gamma^1; S_{H\delta}(\Omega))} \leq \frac{2}{\varrho - 1} e^{-p\log(\varrho)} \max_{\boldsymbol{z} \in \mathcal{A}(\Gamma^1, \tau)} \|\boldsymbol{v}(\cdot, \boldsymbol{z})\|_{S_{H\delta}(\Omega; \mathbb{C}^d)}$$

where $\rho = 2\tau + \sqrt{1 + 4\tau^2}$.

Once we have Lemma 6, which is an analogue of [100, Lemma 3.2], we can conclude with the following convergence theorem. The proof is omitted since it follows the arguments in [100, Theorems 3.10–3.11].

Theorem 4. Assume that \mathbf{u}_{δ} satisfies Assumption 2. Let $\mathbf{u}_{\delta}^{Q}(\mathbf{x}, \boldsymbol{\xi}) = \sum_{k=1}^{Q} \mathbf{u}_{\delta}(\mathbf{x}, \boldsymbol{\xi}_{k}) J_{k}(\boldsymbol{\xi})$. There exist $C_{1} > 0$ and $\beta_{1} > 0$ depending on N and the analytic region $\mathcal{A}(\Gamma, \tau)$ such that

$$\max_{\boldsymbol{\xi} \in \Gamma} \|\boldsymbol{u}_{\delta}(\cdot, \boldsymbol{\xi}) - \boldsymbol{u}_{\delta}^{Q}(\cdot, \boldsymbol{\xi})\|_{S_{H\delta}(\Omega)} \le C_1 Q^{-\beta_1}. \tag{3.12}$$

Moreover, when $\eta > \frac{N}{\log(2)}$, there exist $C_2 > 0$, $C_3 > 0$ and $\beta_2 > 0$ depending on N and the analytic region $\mathcal{A}(\Gamma, \tau)$, and $\beta_3 > 0$ depending only on N such that

$$\max_{\boldsymbol{\xi} \in \Gamma} \|\boldsymbol{u}_{\delta}(\cdot, \boldsymbol{\xi}) - \boldsymbol{u}_{\delta}^{Q}(\cdot, \boldsymbol{\xi})\|_{S_{H\delta}(\Omega)} \le C_{2} Q^{\beta_{2}} e^{-C_{3} Q^{\beta_{3}}}. \tag{3.13}$$

Remark 3. The convergence of the sparse grid approximation in the parameter space is presented in Theorem 4 as the number of Q increases. If we instead use the tensor product formula (3.7) with 1D Chebyshev points for each dimension in the parameter space (then $p_{(i)} = \varpi_{(i)} - 1$ for the ith dimension, and the total number of samples $Q = \prod_{i=1}^{N} \varpi_{(i)}$), then one can use the one dimensional result presented in Lemma 6 to get a convergence order. In particular, if we assume $\varpi = \varpi_{(i)}$ for i = 1, 2, ..., N, then we have a convergence order $O(e^{-\varpi \log(\varrho)}) = O(e^{-Q^{1/N} \log(\varrho)})$ where ϱ depends on the analytic region $\mathcal{A}(\Gamma, \tau)$.

We now present a result on the estimate of the difference between u_{δ}^{Q} and u_{0} .

Theorem 5. Assume that \mathbf{u}_0 satisfies Assumption 2 with $\delta = 0$. Then there exist $C_1 > 0$ and $\beta_1 > 0$ depending on N and the analytic region $\mathcal{A}(\Gamma, \tau)$ such that

$$\max_{\boldsymbol{\xi} \in \Gamma} \|\boldsymbol{u}_0(\cdot, \boldsymbol{\xi}) - \boldsymbol{u}_{\delta}^{Q}(\cdot, \boldsymbol{\xi})\|_{S_{H\delta}(\Omega)} \le \Lambda(\eta, N) \max_{\boldsymbol{\xi} \in \Gamma} \|\boldsymbol{u}_0(\cdot, \boldsymbol{\xi}) - \boldsymbol{u}_{\delta}(\cdot, \boldsymbol{\xi})\|_{S_{H\delta}(\Omega)} + C_1 Q^{-\beta_1}. \tag{3.14}$$

Moreover, when $\eta > \frac{N}{\log(2)}$, there exist $C_2 > 0$, $C_3 > 0$ and $\beta_2 > 0$ depending on N and the analytic region $\mathcal{A}(\Gamma, \tau)$, and $\beta_3 > 0$ depending only on N such that

$$\max_{\boldsymbol{\xi} \in \Gamma} \|\boldsymbol{u}_0(\cdot, \boldsymbol{\xi}) - \boldsymbol{u}_{\delta}^{Q}(\cdot, \boldsymbol{\xi})\|_{S_{H\delta}(\Omega)} \leq \Lambda(\eta, N) \max_{\boldsymbol{\xi} \in \Gamma} \|\boldsymbol{u}_0(\cdot, \boldsymbol{\xi}) - \boldsymbol{u}_{\delta}(\cdot, \boldsymbol{\xi})\|_{S_{H\delta}(\Omega)} + C_2 Q^{\beta_2} e^{-C_3 Q^{\beta_3}}. \tag{3.15}$$

 $\Lambda(\eta, N)$ is the Lebesgue constant associated with the sparse grid interpolation, satisfying

$$\Lambda(\eta, N) \le \sum_{\zeta - N + 1 \le |\boldsymbol{\varpi}|_{l_1} \le \zeta} {N - 1 \choose \zeta - |\boldsymbol{\varpi}|_{l_1}} \prod_{j=1}^{N} \left(\frac{2}{\pi} \log(\boldsymbol{\varpi}_{(j)} + 1) + 1\right). \tag{3.16}$$

Proof. Let $u_0 - u_\delta^Q = u_0 - u_0^Q + u_0^Q - u_\delta^Q$. The term $\max_{\xi \in \Gamma} \|u_0(\cdot, \xi) - u_0^Q(\cdot, \xi)\|_{S_{H\delta}(\Omega)}$ can then be estimated by Theorem 4. Notice that $\Lambda(\eta, N)$ is the Lebesgue constant associated with the sparse grid interpolation, i.e.,

$$\Lambda(\eta, N) := \sup_{v \in C(\Gamma)} \frac{\|\mathcal{J}[v]\|_{L^{\infty}}}{\|v\|_{L^{\infty}}},$$

where $\mathcal{J}[v]$ is given by (3.8), then we have

$$\max_{\boldsymbol{\xi} \in \Gamma} \|\boldsymbol{u}_0^{\mathcal{Q}}(\cdot, \boldsymbol{\xi}) - \boldsymbol{u}_{\delta}^{\mathcal{Q}}(\cdot, \boldsymbol{\xi})\|_{S_{H\delta}(\Omega)} \leq \Lambda(\eta, N) \max_{\boldsymbol{\xi} \in \Gamma} \|\boldsymbol{u}_0(\cdot, \boldsymbol{\xi}) - \boldsymbol{u}_{\delta}(\cdot, \boldsymbol{\xi})\|_{S_{H\delta}(\Omega)},$$

which leads to the desired results. \square

3.3. Stochastic peridynamics formulation with fracture

We now extend the optimization-based quadrature rule introduced in Section 3.1 to the stochastic LPS model with fracture.

For a given point x_i and the horizon δ , a bond is associated with each neighbor $x_j \in B_\delta(x_i)$, and the weight $\omega_{j,i}$ is associated with this bond. In the meshfree formulation, the fracture surface and the corresponding Neumann-type boundary $\partial \Omega_N$ is represented by breaking bonds between x_i and $x_j \in B_\delta(x_i) \setminus \Omega_D$. For $x_j \in B_\delta(x_i) \cap \Omega_D$ and when their bond stretch has not exceeded the critical bond stretch described in (2.25), we denote the bond between x_i and x_j as "intact" and the change of displacement on material point x_j may have an impact on the displacement at x_i . On the other hand, when $x_j \notin \Omega_D$ and/or when $s(x, y, \tau, \xi) > s_0(x, y, \xi)$ for some time $\tau < t$, we consider the bonds between x_i and x_j as "broken". To discretize the LPS formulation (2.21)–(2.22), the quadrature weights associated with intact bonds will be employed for integrals inside $B_\delta(x_i) \setminus \Omega_D$. Particularly, we express the quadrature weights associated with intact bonds as $\tilde{\omega}_{j,i}$ and the quadrature weights associated with broken bonds as $\hat{\omega}_{j,i}$ and the quadrature weights associated with broken bonds as $\hat{\omega}_{j,i}$ through the scalar boolean state function γ . In particular, for each sample $\xi_k \in \Theta_N$, at the nth step we set:

$$\gamma_{j,i,k}^{n} = \begin{cases} 1, & \text{if } \mathbf{x}_{j} \in B_{\delta}(\mathbf{x}_{i}) \cap \Omega_{D} \text{ and } s(\mathbf{x}_{i}, \mathbf{x}_{i}, t^{l}, \boldsymbol{\xi}_{k}) \leq s_{0}(\mathbf{x}_{i}, \mathbf{x}_{j}, \boldsymbol{\xi}_{k}), \ \forall l = 1, \dots, n, \\ 0, & \text{otherwise,} \end{cases}$$

$$(3.17)$$

$$\tilde{\omega}_{j,i,k}^n := \omega_{j,i} \gamma_{j,i,k}^n, \quad \hat{\omega}_{j,i,k}^n := \omega_{j,i} (1 - \gamma_{j,i,k}^n). \tag{3.18}$$

Notice that the new crack forms new free surfaces, which will be included in $\partial \Omega_N$. Therefore, the computational domain Ω will be updated with the evolution of cracks, we therefore denote the updated domain Ω after the nth step as Ω^n and all subdomains such as Ω_D will also be denoted with a similar fashion. Numerical quadrature of a

given function $a(\mathbf{x})$ over $B_{\delta}(\mathbf{x}_i) \cap \Omega_D^n$ and $B_{\delta}(\mathbf{x}_i) \setminus \Omega_D^n$ may thus be calculated via

$$\int_{B_{\delta}(\mathbf{x}_i)\cap\Omega_D^n} a(\mathbf{y})d\mathbf{y} \approx \sum_{\mathbf{x}_j\in\chi_h\cap B_{\delta}(\mathbf{x}_i)} \tilde{\omega}_{j,i,k}^n a(\mathbf{x}_j), \qquad \int_{B_{\delta}(\mathbf{x}_i)\setminus\Omega_D^n} a(\mathbf{y})d\mathbf{y} \approx \sum_{\mathbf{x}_j\in\chi_h\cap B_{\delta}(\mathbf{x}_i)} \hat{\omega}_{j,i,k}^n a(\mathbf{x}_j).$$

This process is consistent with how damage is typically induced in bond-based peridynamics, such as the prototype microelastic brittle model [102].

Applying the above formulation in (2.21)–(2.22), at the *n*th quasi-static step, we aim to solve for the displacement $u_{i,k}^n \approx u(x_i, t^n, \xi_k)$ and nonlocal dilatation $\theta_{i,k}^n \approx \theta(x_i, t^n, \xi_k)$ through the following meshfree scheme:

$$(\mathcal{L}_{F\delta}^{h}\boldsymbol{u})_{i,k}^{n} = \sum_{\boldsymbol{x}_{j} \in \chi_{h} \cap B_{\delta}(\boldsymbol{x}_{i})} K_{ij} \left[\left(- \left(\lambda_{ij,k} - \mu_{ij,k} \right) \left(\boldsymbol{x}_{j} - \boldsymbol{x}_{i} \right) \left(\theta_{i,k}^{n} + \theta_{j,k}^{n} \right) \right.$$

$$\left. - 8\mu_{ij,k} \frac{\left(\boldsymbol{x}_{j} - \boldsymbol{x}_{i} \right) \otimes \left(\boldsymbol{x}_{j} - \boldsymbol{x}_{i} \right)}{\left| \boldsymbol{x}_{j} - \boldsymbol{x}_{i} \right|^{2}} \cdot \left(\boldsymbol{u}_{j,k}^{n} - \boldsymbol{u}_{i,k}^{n} \right) \right) \tilde{\omega}_{j,i,k}^{n-1}$$

$$+ \left(-2 \left(\lambda_{ij,k} - \mu_{ij,k} \right) \left(\boldsymbol{x}_{j} - \boldsymbol{x}_{i} \right) - 4 \left(\lambda_{ij,k} + 2\mu_{ij,k} \right) \mathbf{n}_{i,k}^{n-1} \frac{\left[\left(\boldsymbol{x}_{j} - \boldsymbol{x}_{i} \right) \cdot \mathbf{n}_{i,k}^{n-1} \right] \left[\left(\boldsymbol{x}_{j} - \boldsymbol{x}_{i} \right) \cdot \mathbf{p}_{i,k}^{n-1} \right]^{2}}{\left| \boldsymbol{x}_{j} - \boldsymbol{x}_{i} \right|^{2}} \right.$$

$$+ 4\lambda_{ij,k} \mathbf{n}_{i,k}^{n} \frac{\left[\left(\boldsymbol{x}_{j} - \boldsymbol{x}_{i} \right) \cdot \mathbf{n}_{i,k}^{n} \right]^{3}}{\left| \boldsymbol{x}_{j} - \boldsymbol{x}_{i} \right|^{2}} \right) \theta_{i,k}^{n} \hat{\omega}_{j,i,k}^{n-1} \right] = \boldsymbol{f}(\boldsymbol{x}_{i}), \qquad (3.19)$$

$$\theta_{i,k}^{n} = \sum_{\boldsymbol{x}_{i} \in \boldsymbol{x}_{k} \cap B_{\delta}(\boldsymbol{x}_{i})} K_{ij} \left(\boldsymbol{x}_{j} - \boldsymbol{x}_{i} \right) \cdot \mathbf{M}_{i,k}^{n} \cdot \left(\boldsymbol{u}_{j,k}^{n} - \boldsymbol{u}_{i,k}^{n} \right) \tilde{\omega}_{j,i,k}^{n-1}, \qquad (3.20)$$

where $\lambda_{ij,k} := \lambda(\boldsymbol{x}_i, \boldsymbol{x}_j, \boldsymbol{\xi}_k), \ \mu_{ij,k} := \mu(\boldsymbol{x}_i, \boldsymbol{x}_j, \boldsymbol{\xi}_k),$

$$\mathbf{M}_{i,k}^{n} := \left[\sum_{\mathbf{x}_{j} \in \chi_{h} \cap B_{\delta}(\mathbf{x}_{i})} K_{ij}(\mathbf{x}_{j} - \mathbf{x}_{i}) \otimes (\mathbf{x}_{j} - \mathbf{x}_{i}) \tilde{\omega}_{j,i,k}^{n-1} \right]^{-1}, \tag{3.21}$$

the normal vector $\mathbf{n}(x)$ on free surfaces is numerically approximated and updated as

$$\boldsymbol{n}_{i,k}^{n} = -\frac{\sum\limits_{\boldsymbol{x}_{j} \in \chi_{h} \cap B_{\delta}(\boldsymbol{x}_{i})} (\boldsymbol{x}_{j} - \boldsymbol{x}_{i}) \tilde{\omega}_{j,i,k}^{n-1}}{\left\| \sum\limits_{\boldsymbol{x}_{j} \in \chi_{h} \cap B_{\delta}(\boldsymbol{x}_{i})} (\boldsymbol{x}_{j} - \boldsymbol{x}_{i}) \tilde{\omega}_{j,i,k}^{n-1} \right\|},$$
(3.22)

and the tangential vector $\mathbf{p}_{i,k}^n$ is calculated as the orthogonal direction to $\mathbf{n}_{i,k}^n$. The correction tensor should be invertible to ensure that the correction dilatation can be computed. This holds as long as the bonds in the horizon are non-colinear. For fracture case resulting in bond break, leaving an isolated particle, the matrix inverse may be replaced with the pseudo-inverse to improve the robustness. To postprocess fracture evolution and identify cracks, the damage field $\phi_{i,k}^n \approx \phi(\mathbf{x}_i, t^n, \boldsymbol{\xi}_k)$ can then be defined as

$$\phi_{i,k}^{n} = \frac{\sum\limits_{\substack{x_j \in \chi_h \cap B_\delta(x_i) \backslash x_i \\ x_i \in \chi_h \cap B_\delta(x_i) \backslash x_i}} (1 - \gamma_{j,i,k}^n)}{\sum\limits_{\substack{x_j \in \chi_h \cap B_\delta(x_i) \backslash x_i \\ }} 1},$$
(3.23)

which measures the weakening of material via the percentage of broken bonds in the neighborhood of x_i .

4. Numerical verification of convergences

In this section, we will investigate the asymptotic compatibility of the proposed method by testing the convergence of the numerical solution to its local limit. Three test problems are considered: (1) a material deformation problem featuring smooth local limit for its displacement, (2) a composite material deformation problem featuring discontinuous material properties, and (3) an interfacial crack problem with in-plane extension of two dissimilar materials. In each test we study the L^2 errors for the mean and standard deviation of the solution. Let

 $u_{\delta}^{h,Q}$ represent the numerical solution with spatial grid size h in meshfree methods and Q samples in PCM, u_0 stands for the analytical local limit. We investigate the convergence of numerical solutions to the local limit as Q increases and $\delta, h \to 0$ simultaneously with fixed ratio under the δ -convergence limit. In particular we calculate the expectation $\mathbb E$ and standard derivation σ

$$\|\mathbb{E}(\boldsymbol{u}_{\delta}^{h,Q}) - \mathbb{E}(\boldsymbol{u}_0)\|_{L_2(\Omega)}, \quad \text{and} \quad \|\sigma(\boldsymbol{u}_{\delta}^{h,Q}) - \sigma(\boldsymbol{u}_0)\|_{L_2(\Omega)}. \tag{4.1}$$

In the stochastic problem, the Young's modulus $E(x, \xi)$ is set as a random field to represent the uncertainty in material microstructure, while the Poisson ratio ν is taken as a constant in the whole domain. Moreover, we assume that the material model satisfies the plane strain assumption:

$$\lambda(x, \xi) = E(x, \xi)\nu/((1+\nu)(1-2\nu)), \ \mu(x, \xi) = E(x, \xi)/(2(1+\nu)).$$

Following the conventions in [34], we adopt the nonlocal Lamé moduli as the harmonic mean of the local ones. Similarly, for problems with fracture, the local fracture energy $G(x, \xi)$ is also a random field, with the nonlocal fracture energy $G(x, y, \xi)$ defined via the arithmetic mean of the local ones. For all tests in this validation section, the dimension N of the parametric spaces is less than 4. Therefore, in PCM the tensor product strategy is employed to generate the collocation point set Θ_N . Moreover, in all numerical examples, we adopt the following popular scaled kernel for K:

$$K(r) = \begin{cases} \frac{3}{\pi \delta^3 r}, & \text{for } r \le \delta, \\ 0, & \text{for } r > \delta. \end{cases}$$

$$(4.2)$$

4.1. Test 1: An LPS problem with smooth local limit

We first demonstrate the convergence rates on a Dirichlet-type LPS problem without fracture. In particular, we consider a case with 2D physical domain $\Omega = [-0.5, 0.5] \times [-0.5, 0.5]$ depending on a random variable ξ following a Gaussian distribution $\xi \sim \mathcal{N}(0, 0.1^2)$. The analytical local solution of displacement is given by

$$u_0(x, \xi) = u_0(x, y, \xi) = \left[\sin(x)\sin(y)/(2 + \sin(5\xi)), -\cos(x)\cos(y)/(2 + \sin(5\xi))\right],$$

with Young's modulus

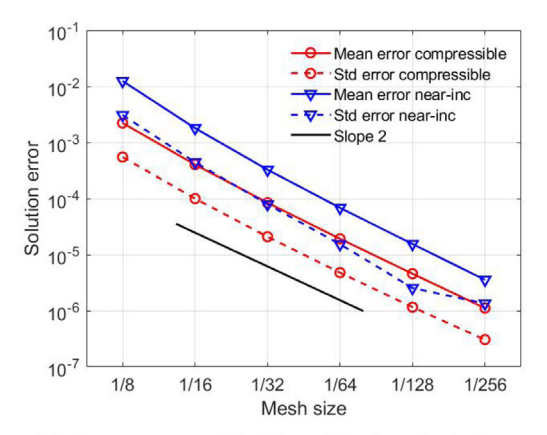
$$E(x, \xi) = E(x, y, \xi) = (2 + \sin(x)\sin(y))(2 + \sin(5\xi)),$$

and fixed loading f(x) = f(x, y):

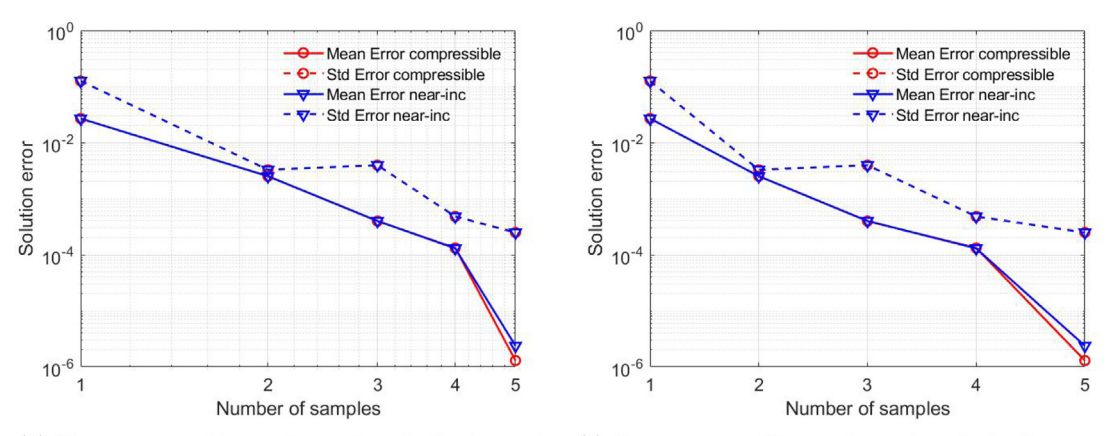
$$f(x, y) = \begin{bmatrix} (C_1 + C_2)(-4\sin(x)\sin(y) + 2\cos(2x)\sin^2(y)) + C_2(-4\sin(x)\sin(y) + 2\cos(2y)\sin^2(x)) \\ (C_1 + 2C_2)(4\cos(x)\cos(y) + \sin(2x)\sin(2y)) \end{bmatrix}^T,$$

where $C_1 := \nu/((1+\nu)(1-2\nu))$, $C_2 := 1/(2(1+\nu))$. In this problem we consider full Dirichlet-type boundary condition on $\partial \Omega$, and Dirichlet-type boundary conditions are applied on $\mathcal{BB}\Omega$ as $\boldsymbol{u}_D(x,y,\xi) = \boldsymbol{u}_0(x,y,\xi)$. Two values of Poisson ratio, $\nu = 0.3$ and 0.495, are investigated which correspond to compressible (as denoted by "compressible") and nearly-incompressible (as denoted by "near-inc") materials, respectively. Here we notice that when $\nu = 0.3$, Assumption 1 is satisfied and we therefore have the $O(\delta^2)$ convergence to the local limit guaranteed by Theorem 3. However, when the material is nearly-incompressible, Assumption 1 is not satisfied.

Numerical results are provided in Fig. 1. With fixed ratio $\delta/h = 3.0$ and Q = 15 samples, in Fig. 1(a) we show the error of numerical solution with respect to the analytical local limit for grid sizes $h = \{1/8, 1/16, 1/32, 1/64, 1/128, 1/256\}$. The optimal second-order convergence $O(\delta^2)$ is observed, which is consistent with Corollary 1 and the results in [34]. In Figs. 1(b) and 1(c) we fix h = 1/256 and $\delta = 3.0h$, and show the convergence of solution error with increasing number of samples $Q \in \{1, \dots, 5\}$ in the parametric space. In Fig. 1(b), the horizontal axis is taken as ϖ (notice that we have $\varpi = Q$, the number of samples, in this 1D case) in the logarithm scale to investigate if the solution error has algebraic convergence or not, while in Fig. 1(c), the horizontal axis is taken as the polynomial order ϖ in the linear scale to investigate the exponential convergence. Almost exponential convergence is observed empirically, verifying the analysis of Remark 3. Similar convergence rates are observed in the compressible and nearly incompressible cases, which indicates that the conditions in Assumption 1 are sufficient conditions for the compatibility property but not a necessity.



(a) Convergence with $\delta, h \to 0$ in the physical space.



(b) Convergence with sample numbers in the log scale. (c) Convergence with sample numbers in the linear scale.

Fig. 1. Convergence study of Test 1: a LPS problem with smooth local limit on 2D physical domain and 1D parametric space. Both compressible ($\nu = 0.3$, as denoted by "compressible" cases) and nearly incompressible ($\nu = 0.495$, as denoted by "near-inc" case) are investigated. Results in (a) are generated with 15 samples. The data points in (b) and (c) correspond to $1, 2, \ldots, 5$ samples, respectively.

4.2. Test 2: Composite material with discontinuous material properties

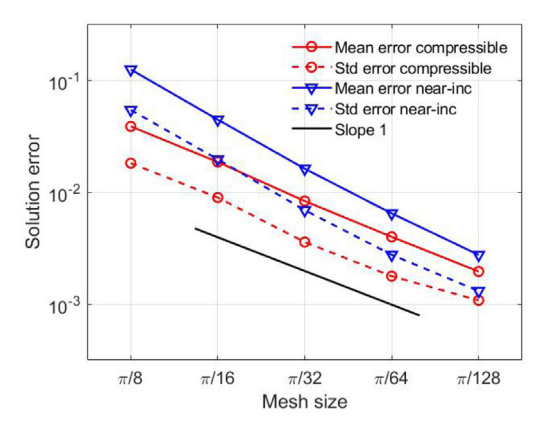
We now investigate composite materials with discontinuous material properties. A 2D physical domain $\Omega = [-\pi/2, \pi/2] \times [-\pi/2, \pi/2]$ and 2D parametric space $\boldsymbol{\xi} = (\xi_{(1)}, \xi_{(2)})$ are considered, where $\xi_{(1)}, \xi_{(2)}$ are i.i.d. standard Gaussian random variables, i.e. $\xi_{(k)} \sim \mathcal{N}(0,1), k=1,2$. Denoting the left half of the physical domain as $\Omega_1 := [-\frac{\pi}{2}, 0] \times [-\frac{\pi}{2}, \frac{\pi}{2}]$ and the right half as $\Omega_2 := [0, \frac{\pi}{2}] \times [-\frac{\pi}{2}, \frac{\pi}{2}]$, the analytical local solution of displacement is given by

$$\mathbf{u}_{0}(\mathbf{x}, \boldsymbol{\xi}) = \begin{cases} \left[3x/(3 + \sin(\xi_{(1)}) + \sin(\xi_{(2)})), -x/(3 + \sin(\xi_{(1)})) + \sin(\xi_{(2)}) \right], & \text{for } (x, y) \in \Omega_{1} \\ \left[1.5x/(3 + \sin(\xi_{(1)}) + \sin(\xi_{(2)})), -0.5x/(3 + \sin(\xi_{(1)}) + \sin(\xi_{(2)})) \right], & \text{for } (x, y) \in \Omega_{2} \end{cases}$$

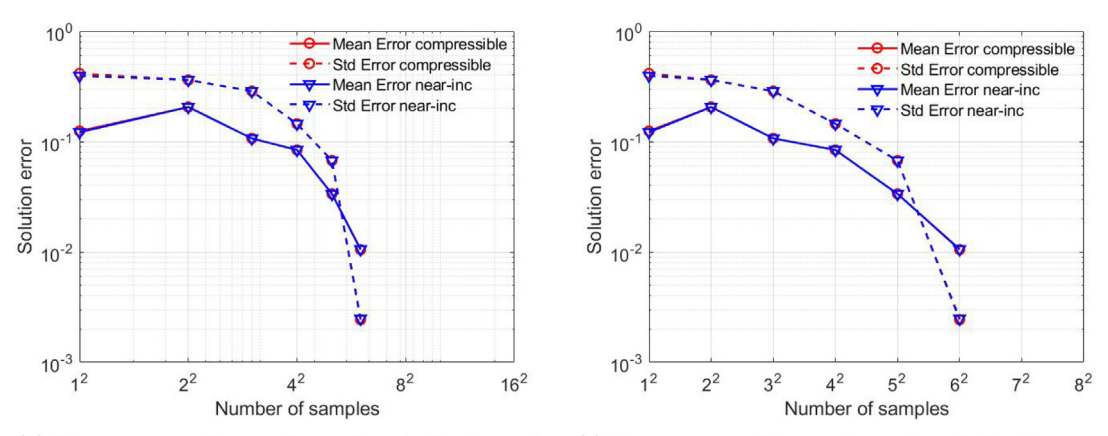
with Young's modulus

$$E(x, \xi) = \begin{cases} 3 + \sin(\xi_{(1)}) + \sin(\xi_{(2)}), & \text{for } (x, y) \in \Omega_1 \\ 2(3 + \sin(\xi_{(1)}) + \sin(\xi_{(2)})), & \text{for } (x, y) \in \Omega_2 \end{cases}$$

and zero loading forces f. In this example we also consider the LPS formulation with full Dirichlet-type boundary condition and without fracture. For $x \in \mathcal{BB}\Omega$, Dirichlet-type boundary conditions are applied as the analytical



(a) Convergence with $\delta, h \to 0$ in the physical space.

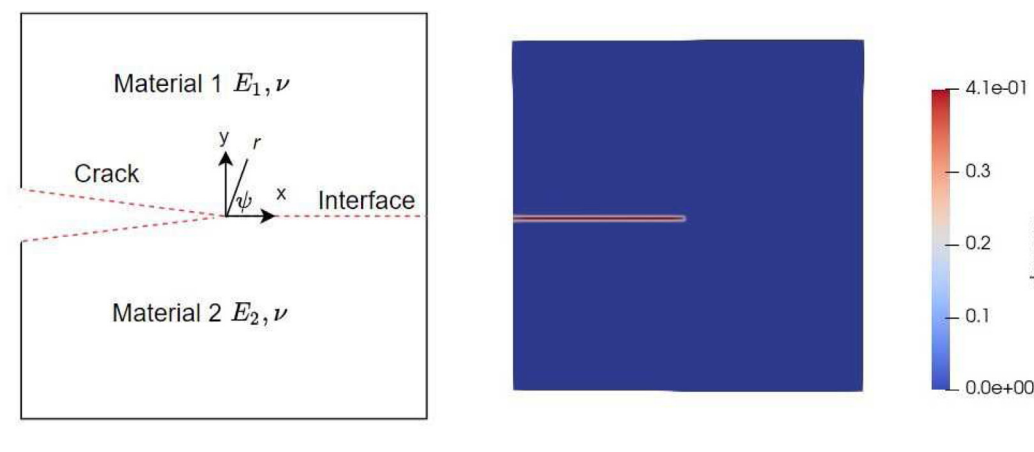


(b) Convergence with sample numbers in the log scale. (c) Convergence with sample numbers in the linear scale.

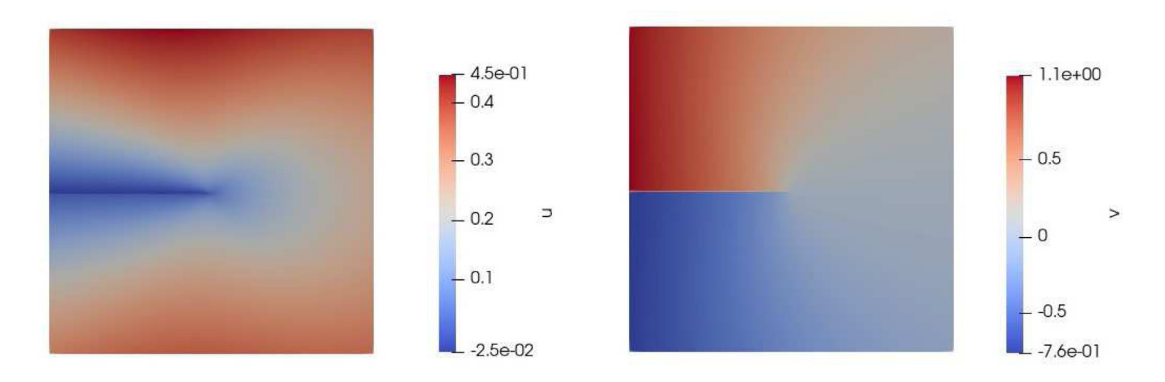
Fig. 2. Convergence study of Test 2: composite material with discontinuous material properties on 2D physical domain and 2D parametric space. Both compressible ($\nu = 0.3$, as denoted by "compressible" cases) and nearly incompressible ($\nu = 0.495$, as denoted by "near-inc" cases) are investigated. Results in (a) are generated with $15^2 = 225$ samples. The data points in (b) and (c) correspond to $1^2, 2^2, \ldots, 6^2$ samples, respectively.

local solution. Similar as in Test 1, two values of Poisson ratio, $\nu = 0.3$ and 0.495, are investigated. Assumption 1 is satisfied when $\nu = 0.3$, but not for $\nu = 0.495$. Here we notice that with discontinuous material properties, the conditions in our compatibility Theorem 2 are no longer satisfied. Therefore, with this example we aim to investigate the numerical stability and AC convergence rates that the theoretical analysis in Section 2.1 does not cover. On the other hand, with the smoothness of u_0 in the parametric space, it satisfies Assumption 2. Therefore, as we increase ϖ in PCM, an exponential convergence is expected from Remark 3.

Numerical results are provided in Fig. 2. With fixed ratio $\delta/h = 3.0$ and Q = 225 samples, in Fig. 2(a) we show the error of numerical solution with respect to the analytical local limit for grid sizes $h = \{\pi/8, \pi/16, \pi/32, \pi/64, \pi/128\}$. First-order convergence $O(\delta)$ is observed, which is consistent with the numerical observations in [34]. In Figs. 2(b) and 2(c) we fix $h = \pi/256$ and $\delta = 3.0h$, and show the convergence of solution error with increasing number of samples $Q \in \{1^2, \dots, 6^2\}$ in the parametric space. Similar as in test 1, in Fig. 2(b), the horizontal axis is taken as ϖ (notice that we have $Q = \varpi^2$ in this case, since the tensor product formula is employed in PCM) in the logarithm scale while in Fig. 2(c), the horizontal axis is taken as ϖ in the linear scale to investigate the exponential convergence. An exponential convergence is observed empirically, verified the analysis in Remark 3.



- (a) Problem setting, where crack lies on a bimaterial interface subjected to remote loading.
- (b) Analytical damage field.



- (c) Analytical displacement on the x-direction.
- (d) Analytical displacement on the y-direction.

Fig. 3. Problem setup and analytical solutions in Test 3: material fracture on a bimaterial interface.. (For interpretation of the references to color in this figure legend, the reader is referred to the web version of this article.)

4.3. Test 3: Material fracture on a bimaterial interface

In this example, we proceed to consider the fracture problem. As shown in Fig. 3, we consider the inplane extension of two dissimilar materials with cracks aligning with their interface. A physical domain $\Omega = [-\pi/2, \pi/2] \times [-\pi/2, \pi/2]$ is employed. The material property depends on a two i.i.d. random variables $\xi_{(1)}$ and $\xi_{(2)}$, where $\xi_{(1)} \sim \mathcal{N}(0, 1)$ satisfies a Gaussian distribution and $\xi_{(2)} \sim \mathcal{U}[-1, 1]$ satisfies a uniform distribution. The Young's modulus of the two materials, on the upper half plane and the lower half plane respectively, are denoted as $E_1(\xi)$ and $E_2(\xi)$. In particular, we take $E_1(\xi) = 2 + \sin(\xi_{(1)})$ and $E_2(\xi) = 2 + \sin(\xi_{(2)})$. Both compressible ($\nu = 0.3$) and nearly incompressible ($\nu = 0.495$) will be investigated. Again, Assumption 1 is satisfied when $\nu = 0.3$, but not for $\nu = 0.495$. For this problem the Cartesian component of the analytical local displacement field u is given by [103]:

$$\boldsymbol{u}_{0}(\boldsymbol{x},\boldsymbol{\xi}) = \begin{bmatrix} u(\boldsymbol{x},\boldsymbol{\xi}) \\ v(\boldsymbol{x},\boldsymbol{\xi}) \end{bmatrix}^{T} = \sqrt{\frac{r(\boldsymbol{x})}{2\pi}} \left(\operatorname{Re}(r(\boldsymbol{x})^{i\epsilon(\boldsymbol{\xi})}) \begin{bmatrix} u^{I}(\psi(\boldsymbol{x}),\boldsymbol{\xi}) \\ v^{I}(\psi(\boldsymbol{x}),\boldsymbol{\xi}) \end{bmatrix} + \operatorname{Im}(r(\boldsymbol{x})^{i\epsilon(\boldsymbol{\xi})}) \begin{bmatrix} u^{II}(\psi(\boldsymbol{x}),\boldsymbol{\xi}) \\ v^{II}(\psi(\boldsymbol{x}),\boldsymbol{\xi}) \end{bmatrix} \right)^{T}$$

$$(4.3)$$

where $(r(x), \psi(x))$ correspond to the local polar coordinate system of x with origin at the crack tip, $\text{Re}(\cdot)$ and $\text{Im}(\cdot)$ denote the real and imaginary parts of a complex number, respectively. Notice that in this example we follow [103] and take the complex stress intensity factor (SIF) as 1.0. The bimaterial constant $\epsilon(\xi)$ depends on the material properties of both materials and leads to oscillation of near-tip displacements and stresses:

$$\epsilon(\xi) = \frac{1}{2\pi} \log \frac{\mu_2(\xi)\kappa_1 + \mu_1(\xi)}{\mu_1(\xi)\kappa_2 + \mu_2(\xi)}, \quad \mu_m(\xi) = \frac{E_m(\xi)}{2(1+\nu)}, \quad \kappa_m = 3 - 4\nu, \text{ for } m = 1, 2.$$
(4.4)

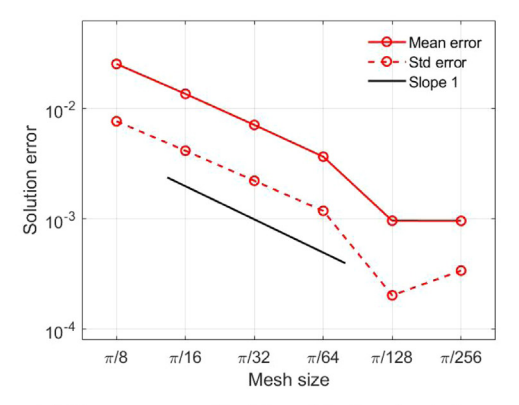
We set the material properties $\mu(x, \xi) = \mu_1(\xi)$, $\kappa(x) = \kappa_1$ when x is in the upper half-plan, and $\mu(x, \xi) = \mu_2(\xi)$, $\kappa(x) = \kappa_2$ when x is in the lower half-plan. (u^I, v^I) and (u^{II}, v^{II}) are then functions of the angular $\psi(x)$ and ξ :

$$u^{I}(\psi(\mathbf{x}), \boldsymbol{\xi}) := -\frac{1}{2\mu(\mathbf{x}, \boldsymbol{\xi})(1 + 4\epsilon(\boldsymbol{\xi})^{2})\cosh(\pi\epsilon(\boldsymbol{\xi}))} \left\{ \left[e^{\epsilon(\boldsymbol{\xi})(\Pi(\mathbf{x}) - \psi(\mathbf{x}))} - \kappa(\mathbf{x})e^{-\epsilon(\boldsymbol{\xi})(\Pi(\mathbf{x}) - \psi(\mathbf{x}))} \right] \cos(\psi(\mathbf{x})/2) \right. \\ \left. - (1 + 4\epsilon(\boldsymbol{\xi})^{2})e^{-\epsilon(\boldsymbol{\xi})(\Pi(\mathbf{x}) - \psi(\mathbf{x}))} \sin\psi(\mathbf{x})\sin(\psi(\mathbf{x})/2) \right. \\ \left. + 2\epsilon(\boldsymbol{\xi}) \left[e^{\epsilon(\boldsymbol{\xi})(\Pi(\mathbf{x}) - \psi(\mathbf{x}))} + \kappa(\mathbf{x})e^{-\epsilon(\boldsymbol{\xi})(\Pi(\mathbf{x}) - \psi(\mathbf{x}))} \right] \sin(\psi(\mathbf{x})/2) \right],$$

$$v^{I}(\psi(\mathbf{x}), \boldsymbol{\xi}) := \frac{1}{2\mu(\mathbf{x}, \boldsymbol{\xi})(1 + 4\epsilon(\boldsymbol{\xi})^{2})\cosh(\pi\epsilon(\boldsymbol{\xi}))} \left\{ \left[e^{\epsilon(\boldsymbol{\xi})(\Pi(\mathbf{x}) - \psi(\mathbf{x}))} + \kappa(\mathbf{x})e^{-\epsilon(\boldsymbol{\xi})(\Pi(\mathbf{x}) - \psi(\mathbf{x}))} \right] \sin(\psi(\mathbf{x})/2) \right. \\ \left. - (1 + 4\epsilon(\boldsymbol{\xi})^{2})e^{-\epsilon(\boldsymbol{\xi})(\Pi(\mathbf{x}) - \psi(\mathbf{x}))} \sin\psi(\mathbf{x})\cos(\psi(\mathbf{x})/2) \right. \\ \left. - 2\epsilon(\boldsymbol{\xi}) \left[e^{\epsilon(\boldsymbol{\xi})(\Pi(\mathbf{x}) - \psi(\mathbf{x}))} - \kappa(\mathbf{x})e^{-\epsilon(\boldsymbol{\xi})(\Pi(\mathbf{x}) - \psi(\mathbf{x}))} \right] \cos(\psi(\mathbf{x})/2) \right. \right. \\ \left. - 2\epsilon(\boldsymbol{\xi}) \left[e^{\epsilon(\boldsymbol{\xi})(\Pi(\mathbf{x}) - \psi(\mathbf{x}))} - \kappa(\mathbf{x})e^{-\epsilon(\boldsymbol{\xi})(\Pi(\mathbf{x}) - \psi(\mathbf{x}))} + \kappa(\mathbf{x})e^{-\epsilon(\boldsymbol{\xi})(\Pi(\mathbf{x}) - \psi(\mathbf{x}))} \right] \sin(\psi(\mathbf{x})/2) \right. \\ \left. + (1 + 4\epsilon(\boldsymbol{\xi})^{2})e^{-\epsilon(\boldsymbol{\xi})(\Pi(\mathbf{x}) - \psi(\mathbf{x}))} \sin\psi(\mathbf{x})\cos(\psi(\mathbf{x})/2) \right. \\ \left. - 2\epsilon(\boldsymbol{\xi}) \left[e^{\epsilon(\boldsymbol{\xi})(\Pi(\mathbf{x}) - \psi(\mathbf{x}))} - \kappa(\mathbf{x})e^{-\epsilon(\boldsymbol{\xi})(\Pi(\mathbf{x}) - \psi(\mathbf{x}))} - \kappa(\mathbf{x})e^{-\epsilon(\boldsymbol{\xi})(\Pi(\mathbf{x}) - \psi(\mathbf{x}))} \right] \cos(\psi(\mathbf{x})/2) \right. \\ \left. + (1 + 4\epsilon(\boldsymbol{\xi})^{2})e^{-\epsilon(\boldsymbol{\xi})(\Pi(\mathbf{x}) - \psi(\mathbf{x}))} \sin\psi(\mathbf{x})\sin(\psi(\mathbf{x})/2) \right. \\ \left. + (1 + 4\epsilon(\boldsymbol{\xi})^{2})e^{-\epsilon(\boldsymbol{\xi})(\Pi(\mathbf{x}) - \psi(\mathbf{x}))} \sin\psi(\mathbf{x})\sin(\psi(\mathbf{x})/2) \right. \\ \left. + (1 + 4\epsilon(\boldsymbol{\xi})^{2})e^{-\epsilon(\boldsymbol{\xi})(\Pi(\mathbf{x}) - \psi(\mathbf{x}))} \sin\psi(\mathbf{x})\sin(\psi(\mathbf{x})/2) \right. \\ \left. + (1 + 4\epsilon(\boldsymbol{\xi})^{2})e^{-\epsilon(\boldsymbol{\xi})(\Pi(\mathbf{x}) - \psi(\mathbf{x}))} \sin\psi(\mathbf{x})\sin(\psi(\mathbf{x})/2) \right. \\ \left. + (2\epsilon(\boldsymbol{\xi})[e^{\epsilon(\boldsymbol{\xi})(\Pi(\mathbf{x}) - \psi(\mathbf{x}))} + \kappa(\mathbf{x})e^{-\epsilon(\boldsymbol{\xi})(\Pi(\mathbf{x}) - \psi(\mathbf{x}))}]\sin(\psi(\mathbf{x})/2) \right. \right. \\ \left. + (2\epsilon(\boldsymbol{\xi})[e^{\epsilon(\boldsymbol{\xi})(\Pi(\mathbf{x}) - \psi(\mathbf{x}))} + \kappa(\mathbf{x})e^{-\epsilon(\boldsymbol{\xi})(\Pi(\mathbf{x}) - \psi(\mathbf{x}))}]\sin(\psi(\mathbf{x})/2) \right. \\ \left. + (2\epsilon(\boldsymbol{\xi})[e^{\epsilon(\boldsymbol{\xi})(\Pi(\mathbf{x}) - \psi(\mathbf{x}))} + \kappa(\mathbf{x})e^{-\epsilon(\boldsymbol{\xi})(\Pi(\mathbf{x}) - \psi(\mathbf{x}))}]\sin(\psi(\mathbf{x})/2) \right. \right] \right.$$

Here the value of $\Pi(x)$ also depends on the location of x: $\Pi(x) = \pi$ for x on the upper half-plane, whereas $\Pi(x) = -\pi$ for the lower half-plane. In Fig. 3 we plot the analytical local solution for the damage field and the displacement fields for illustration. In particular, the crack is represented by breaking the bonds across the segment between $(-\frac{\pi}{2}, 0)$ and (0, 0). On the crack surface, free surface conditions are imposed, while full Dirichlet-type boundary conditions are applied on all four sides of the plate. Similar as in Test 2, in this example the Young's modulus $E(x, \xi)$ is (spatially) discontinuous across the interface, and therefore the conditions in our compatibility Theorem 2 are no longer satisfied.

Numerical results for compressible and nearly incompressible cases are provided in Figs. 4 and 5, respectively. With fixed ratio $\delta/h = 3.0$ and Q = 400 samples, in Figs. 4(a) and 5(a) we show the error of numerical solution with respect to the analytical local limit for grid sizes $h = \{\pi/8, \pi/16, \pi/32, \pi/64, \pi/128, \pi/256\}$. First-order convergence $O(\delta)$ is observed. In Figs. 4(b), 4(c), 5(b) and 5(c), using fixed grid size $h = \pi/256$ and $\delta = 3.0h$, we demonstrate the convergence of solution errors with increasing number of samples $Q = \{1^2, \dots, 9^2\}$ in the parametric space. Similar as in tests 1 and 2, in Figs. 4(b) and 5(b), the error is plotted versus ϖ in the logarithm scale while in Figs. 4(c) and 5(c) the horizontal axis is taken as ϖ in the linear scale. A roughly algebraic convergence rate is observed. We notice that the convergence curve seems more oscillatory comparing with the previous two tests, possibly due to the solution nonlinearity induced by the spatial discontinuity and the reduced regularity in the parametric space. In fact, in [104–106], a similar phenomenon of oscillatory convergence curve was observed, when the solution has discontinuity or reduced regularity in the parametric space (see, e.g., Figure 6 of [107]). To further demonstrate the sample efficiency of the proposed approach, we also plot the convergence



(a) Convergence with $\delta, h \to 0$ in the physical space.

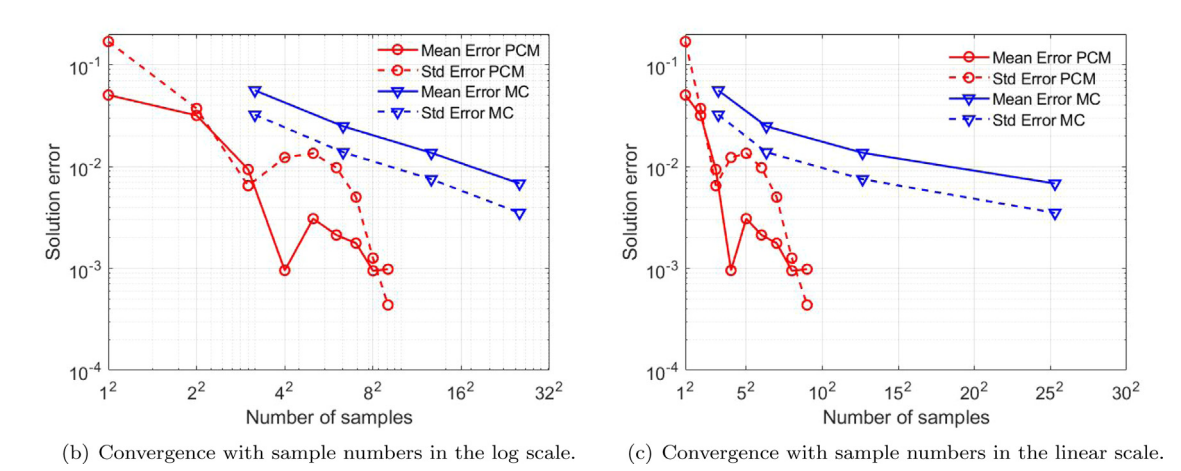
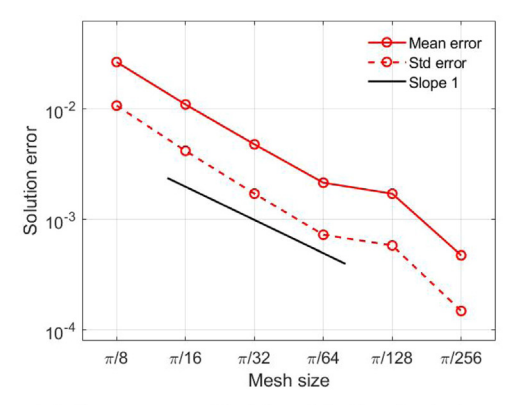


Fig. 4. Convergence study of Test 3: material fracture on a bimaterial interface, for **compressible materials** (ν =0.3). Here we use "PCM" to denote the cases using our proposed probabilistic collocation method approach, and "MC" to denote the cases using the Monte Carlo method. Results in (a) are generated with $20^2 = 400$ samples. The data points in (b) and (c) are corresponding to $1^2, \ldots, 9^2$ samples.

of numerical solutions obtained from Monte Carlo (MC) simulations. The results indicate that to achieve a similar level of accuracy, our proposed approach requires a much smaller number of samples compared to MC.

5. Application: Brittle fracture of glass-ceramics

Having illustrated the AC convergence to the analytical local limits and verified the theoretical analysis in Sections 2–3, we now consider a problem of brittle fracture in a glass-ceramic material as a prototypical exemplar, and provide validation against experiment results. The main objective of this section is to provide a proof-of-principle demonstration that the framework introduced thus far applies to realistic settings, however overall the provided preliminary validation provides good agreement. A glass-ceramic material is the product of controlled crystallization of a specialized glass composition, which results in the creation of a microstructure composed of one or more crystalline phases within the residual amorphous glass. Glass-ceramics have received significant attention due to their enhanced strength and toughness compared to pure glass [89,108–111]. A wide range of flexural strength (100 to \geq 500 MPa) and fracture toughness (1.0 to 5.0 MPa. $m^{0.5}$) are reported in literature [111], with the authors noting that the microstructure and phase assemblage play a vital role in determining strength and toughness. Therefore, it is important to investigate the microstructure of these materials and their relation to damage metrics of interest to get fundamental insight [83]. In particular, we employ the proposed approach to study the fracture toughness of a model glass-ceramic material (lithium disilicate) as a function of crystal volume fraction [83].



(a) Convergence with $\delta, h \to 0$ in the physical space.

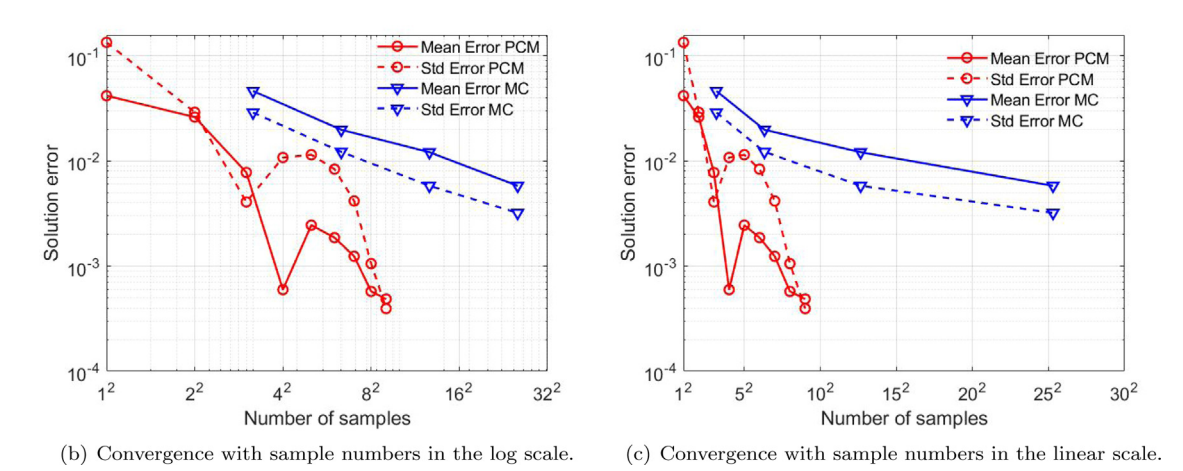


Fig. 5. Convergence study of Test 3: material fracture on a bimaterial interface, for **nearly incompressible materials** (ν =0.495). Here we use "PCM" to denote the cases using our proposed probabilistic collocation method approach, and "MC" to denote the cases using the Monte Carlo method. Results in (a) are generated with $20^2 = 400$ samples. The data points in (b) and (c) are corresponding to $1^2, \ldots, 9^2$ samples.

In this example, we consider a pre-notched idealized microstructural realization which is subject to displacement boundary conditions on its top and bottom boundaries, as demonstrated in Fig. 6. A plate of dimensions 800 µm by 400 μm is considered, which contains an initial crack of length 100 μm. A gradually increasing displacement loading U_D is applied on the top and bottom of the sample. All other boundaries, including the new boundaries created by cracks, are treated as free surfaces. Each realization is composed of randomly distributed crystals embedded in a glassy matrix, with the mechanical properties of glass and crystalline phases listed in Table 1. In particular, we follow [83,89] and generate the center location (C_x, C_y) and rotation angle C_{ψ} of each crystal as random variables satisfying $C_x \sim \mathcal{U}[0, 800]$, $C_y \sim \mathcal{U}[0, 400]$, and $C_\psi \sim \mathcal{U}[0, 2\pi]$. All crystals are identical ellipses with semimajor and semi-minor axes being 12 μm and 7.5 μm, respectively, with an aspect ratio of 1.6. This material was studied experimentally in [83] for different crystallized volume fractions, f. Although the crack pattern varies drastically with different microstructure realizations, for each crystallized volume fraction f the averaged fracture toughness presents a consistent pattern. In particular, a total of three samples were tested experimentally for each crystallized volume fraction and the average of these tests was reported in [83]. It was observed that the averaged fracture toughness grows linearly with f. Therefore, in this example, we aim to reproduce the experimental fracture toughness in [83] rather than the individual crack pattern with numerical simulations, since the former is more reproducible and also provides a more direct measure of the material resistance.

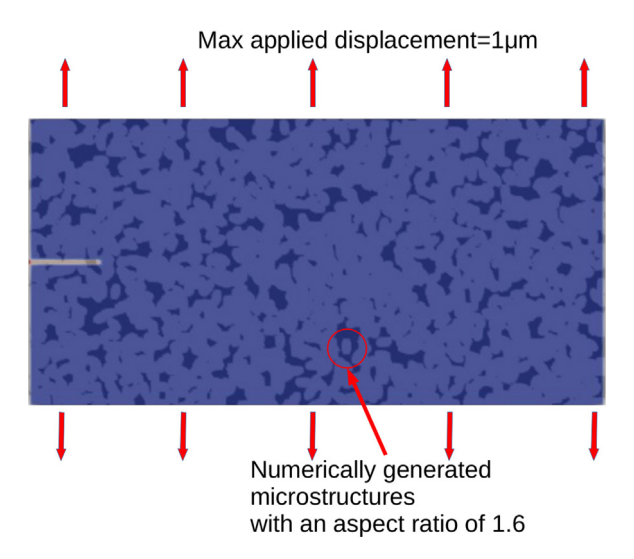


Fig. 6. Problem setup of pre-cracked glass-ceramics experiment with randomly distributed material property fields, following [83]. Here light blue represents the crystalline and dark blue represents the glassy matrix. (For interpretation of the references to color in this figure legend, the reader is referred to the web version of this article.)

 Table 1

 Material properties used in pre-cracked glass-ceramics experiment [83].

	Young's modulus	Poisson ratio	Fracture energy	Fracture toughness
Glass	$E_1 = 80 \text{ GPa}$	0.25	$G_1 = 6.59 \text{ J/m}^2$	0.75 MPa·m ^{0.5}
Crystal	$E_2 = 133 \text{ GPa}$	0.25	$G_2 = 86.35 \text{ J/m}^2$	$3.5 \text{ MPa} \cdot \text{m}^{0.5}$

To numerically simulate the crack growth in this problem, we consider the plane strain model and employ the quasi-static LPS model setting as described in Section 3.3. In numerical experiments, we gradually increase U_D from 0 μ m to 1 μ m, and simulate the propagation of the crack starting from the pre-crack tip till it reaches the right boundary of the domain. At each quasi-static step, we increase U_D by 4e-3 μ m, perform subiterations until no new broken bonds are detected, then proceed to the next step. For spatial discretization, we employ uniform grids with grid size h=2 μ m, and the horizon size $\delta=3h=6$ μ m. Therefore, the whole computational domain $\Omega \cup \mathcal{BB}\Omega$ has M=87969 grid points in total. Four different crystallized volume fraction values are considered: $f \in \{20\%, 40\%, 60\%, 80\%\}$.

To demonstrate the performance of our deterministic LPS solver, in Fig. 7 we show the crack pattern of two samples with volume fractions 20% and 80%, respectively. In Fig. 7(a), one can observe that the crack mostly propagates either inside the glassy matrix or along interfaces after crack deflection and avoids entering the ceramic particles, on account of the fracture toughness of the ceramic phase being much higher. On the other hand, once we increase the crystallinity, as shown in Fig. 7(b)(c) where the crystals occupy 80% of the volume, the crack pattern gets dominated by crystal fracture. In certain cases, where a crack gets penetrated and gets trapped within a large agglomeration, it results in crack bridging wherein it is favorable for the crack to re-initiate in a nearby interface rather than fracturing the crystal agglomeration. Such patterns were also observed and reported in [83], where the authors considered crack deflection, trapping and bridging as the three main toughening mechanisms in glass-ceramics.

We now proceed to solve the stochastic LPS problem and provide a quantitative validation by comparing the numerical results on fracture toughness with the experimental measurements in [83]. In this study, the material microstructure is treated as a random field, and the quantities of interest would be the averaged fracture toughness of different realizations for each volume fraction $f \in \{20\%, 40\%, 60\%, 80\%\}$. For each realization, we use $R(x, \omega)$

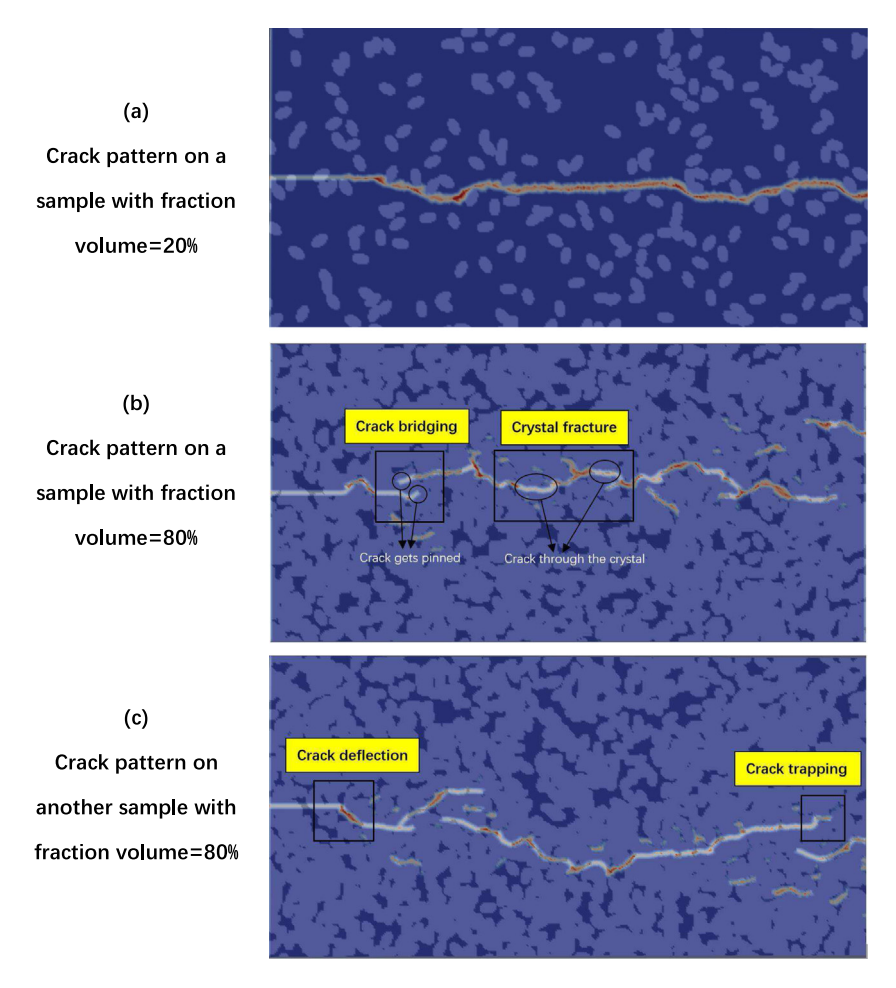


Fig. 7. Crack pattern (represented by the damage field ϕ) of glass-ceramics on two sample microstructures. Here light blue represents the crystalline and dark blue represents the glassy matrix. (a) A sample with crystal volume fraction f=20%. Neither crack bridging nor crystal fracture is observed. (b)(c) Two samples with crystal volume fraction f=80%. The crack pattern is dominated by crystal fracture, and crack bridging, deflection and trapping are also observed. (For interpretation of the references to color in this figure legend, the reader is referred to the web version of this article.)

to denote the microstructure, such that for each $\omega \in \Omega_p$,

$$R(x, \omega) = \begin{cases} 0 & \text{if the material point } x \text{ is glass,} \\ 1 & \text{if the material point } x \text{ is crystal.} \end{cases}$$
 (5.1)

We then notice that the random fields of Young's modulus $E(x, \omega)$ and fracture energy $G(x, \omega)$ can be represented as linear transformations of R:

$$E(\mathbf{x}, \omega) = R(\mathbf{x}, \omega)(E_2 - E_1) + E_1, \quad G(\mathbf{x}, \omega) = R(\mathbf{x}, \omega)(G_2 - G_1) + G_1,$$

where E_1 , E_2 are the Young's modulus of glass and crystal, respectively, and G_1 , G_2 are their fracture energy. The material responses and crack propagation in this sample can then be calculated using the LPS solver (3.19)–(3.20), and the fracture toughness is determined by the mechanisms through which cracks interact with constituents in microstructures [112]. Based on the final crack pattern, we first calculate the average energy release rate through

$$G_{IC} = \frac{G_1 L_1 + G_2 L_2 + G_i L_i}{W},\tag{5.2}$$

where W is the total projected crack length along the x-direction and $G_i := (G_1 + G_2)/2$ denotes the fracture energy for interface debonding. L_1 , L_2 and L_i are the crack length within the glass, within the ceramic and along their interface, calculated through the number of broken bonds per particle. For brittle materials, one can then obtain the fracture toughness K_{IC} from the critical energy release rate:

$$K_{IC} = \sqrt{G_{IC} \frac{E_{eff}}{1 - v^2}},$$
 (5.3)

where $E_{eff} = (1 - f)E_1 + fE_2$ is approximately the effective Young's modulus of the heterogeneous material for the volume fraction f. For further details and discussions on the calculation of fracture toughness for ceramic composites, we refer interested readers to [112].

Although one can calculate the averaged fracture toughness by sampling $R(x, \omega)$ using the Monte Carlo method, we notice that the sampling space Ω_p is of high dimension and therefore would possibly require a large number of samples. This fact calls for dimensionality reduction for Ω_p so as to represent the random fields of E and G using a limited number of random variables. In this work, the principal component analysis (PCA) approach is employed. In particular, for each crystallized volume fraction value we generate 20,000 discretized microstructure realizations $R(x_i, \omega_j)$, $i = 1, \ldots, M$, $j = 1, \ldots, 20000$. Equivalently, we represent each realization by a vector, $R_j \in \mathbb{R}^M$, such that $R_j[i] = R(x_i, \omega_j)$. We then perform PCA to the data matrix formed by R_j , $j = 1, \ldots, 20000$, and keep the first 20 principal components for dimensionality reduction. To this end, each realization R_j can then be approximated by

$$\mathbf{R}_{j} \approx \overline{\mathbf{R}} + \sum_{k=1}^{20} a_{j,k} \mathbf{V}_{k}, \ i = 1, 2, \dots, M,$$
 (5.4)

where \overline{R} is the mean of all R_j , V_k denote the k-th eigenvector in PCA, and $a_{j,k}$ is the kth component of the j-th realization. Thus, we obtain a truncated representation for the Young's modulus and fracture energy fields in glass-ceramics:

$$E(\mathbf{x}_{i}, \boldsymbol{\xi}) = (\overline{\mathbf{R}} + \sum_{k=1}^{20} \xi_{(k)} \mathbf{V}_{k})(E_{2} - E_{1}) + E_{1}, \qquad G(\mathbf{x}_{i}, \boldsymbol{\xi}) = (\overline{\mathbf{R}} + \sum_{k=1}^{20} \xi_{(k)} \mathbf{V}_{k})(G_{2} - G_{1}) + G_{1}.$$
 (5.5)

where $\xi_{(k)}$ is the kth component of ξ . We further take $\xi_{(k)}$ as i.i.d. random variables satisfying $\xi_{(k)} \sim \mathcal{N}(0, \lambda_k^2)$, where λ_k is the k_{th} eigenvalue in PCA. Noticing that E and G are both affine with respect to ξ , and therefore PCM can be applied and the parametric space dimension is 20. For this example we employ the Smolyak formulation with level 2, which consists of 41 samples for each volume fraction value. The results are demonstrated in Fig. 8, together with the experimental measurements from [83]. We also report the results using the Monte Carlo method as a baseline method, where the fracture toughness for each volume fraction is generated from 100 realizations from the original sampling space Ω_p . From the results, we can observe that the results from both PCA and MC are in good agreement with the experiment data. Comparing these two methods, although PCA uses fewer samples, its predictions are more aligned with the linear fitted line from experimental measurements, and are with a low error interval estimation. This validates the applicability of our stochastic LPS solver on providing averaged damage metrics in randomly heterogeneous material fracture problems.

6. Summary and discussion

For heterogeneous material modeling problems, different material microstructure, property, interfacial conditions, and operating environments all cause variability within materials, which is tremendously difficult to be fully quantified. Therefore, without complete detailed measurements for each individual material sample, it is often non-practical, if not impossible, to provide comprehensive quantitative damage characterization for each sample. This fact calls for stochastic modeling for the variability and characterization of material failure for uncertainty quantification.

In this work, we propose a state-based peridynamics formulation with spatial variability of material properties, to capture the high degrees of complexity and heterogeneity in material damage problems. The well-posedness and convergence to the local problems are studied for the proposed stochastic peridynamics model, which provide a theoretical foundation for numerical developments. An asymptotically compatible meshfree discretization method

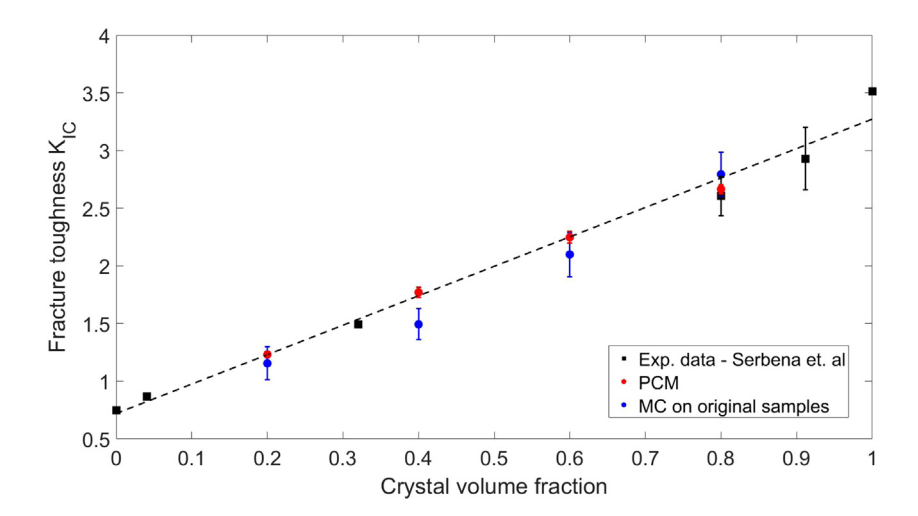


Fig. 8. Averaged fracture toughness for brittle fracture of glass-ceramics with different crystal volume fractions. Error bars represent standard derivations. Here we use "PCM" to denote the results using our proposed probabilistic collocation method approach with 41 samples from the truncated sampling space, "MC" to denote the results using the Monte Carlo method with 100 samples from the original space Ω_p , and "Exp" denotes the experimental results reported in [83].. (For interpretation of the references to color in this figure legend, the reader is referred to the web version of this article.)

is developed for the peridynamics model. It provides an efficient representation of interfaces and fracture surfaces. A probabilistic collocation method (PCM) is employed to sample the random field, which guarantees at least algebraic convergence rate for smooth problems in the parametric space, and therefore ensures the sampling efficiency. This work has presented a complete workflow demonstrating how quadrature, heterogeneity and fracture can be handled for linear elastic materials. In this way, variability in microstructures is captured and a limit to the relevant local problem is preserved as resolution and number of samples are increased. We view this as a major contribution to the field of peridynamics - while numerous works have demonstrated the flexibility of peridynamics in modeling a diverse set of physical phenomena in a deterministic setting, very few studies have considered the impact of uncertainty in material properties and microstructures. Last but not least, we demonstrate an application of the proposed formulation to estimate the fracture toughness of glass-ceramics, quantitatively validating its applicability in practical engineering problems.

While the current work has been mainly focused on the physical processes of material damage with uncertainty from material heterogeneity, an important next step is to incorporate other types of uncertainties, such as the variability from interfacial conditions and operating environments. We will further consider the generalization of this approach to other types of damage modes, such as the nonlinear elastoplasticity which governs the ductile failure. The proposed formulations can be easily extended to 3D problems, though we notice that we were unable to perform 3D simulations mainly due to memory limitations of our serial LPS solver. The numerical framework itself is parallelizable and hence highly scalable, as the meshfree quadrature rule involves only the local construction and inversion of small matrices. For future work, we will investigate how the proposed approach extends to 3D and demonstrate its application in 3D realistic problems.

Declaration of competing interest

The authors declare that they have no known competing financial interests or personal relationships that could have appeared to influence the work reported in this paper.

Data availability

Data will be made available on request.

Acknowledgments

Y. Fan, H. You and Y. Yu would like to acknowledge support by the National Science Foundation under award DMS-1753031. Portions of this research were conducted on Lehigh University's Research Computing infrastructure partially supported by National Science Foundation Award 2019035. X. Tian's research is supported in part by the National Science Foundation Award DMS-2111608. X. Li's research is supported in part by National Science Foundation Award DMS-1847770 and UNC Charlotte internal Faculty Research Grants. X. Yang's research is supported in part by the Energy Storage Materials Initiative, which is a Laboratory Directed Research and Development Project at Pacific Northwest National Laboratory. N. Prakash would like to acknowledge discussions with Jason T. Harris, Ross J. Stewart, Binghui Deng, Charlene M. Smith.

Appendix. Detailed proofs of lemmas and theorems

A.1. Proof of Lemma 1

In this section we elaborate the detailed proof for the characterization of the nonlocal energy space, $S_{H\delta}(\Omega)$, in Lemma 1.

Proof. With the Cauchy–Schwarz inequality we have

$$|\theta(x)| = \left| \int_{\Omega \cup \mathcal{B} \mathcal{B} \Omega} K(|y - x|)(y - x) \cdot (u(y) - u(x)) \, dy \right|$$

$$\leq \sqrt{2} \left(\int_{\Omega \cup \mathcal{B} \mathcal{B} \Omega} \frac{K(|y - x|)}{|y - x|^2} [(y - x) \cdot (u(y) - u(x))]^2 dy \right)^{1/2}, \tag{A.1}$$

and

$$\int_{\Omega \cup \mathcal{B} \mathcal{B} \Omega} \int_{\Omega \cup \mathcal{B} \mathcal{B} \Omega} K(|y-x|) |(y-x) \cdot (u(y)-u(x))| dy \, \theta(x) dx$$

$$\leq \sqrt{2} \int_{\Omega \cup \mathcal{B} \mathcal{B} \Omega} \left(\int_{\Omega \cup \mathcal{B} \mathcal{B} \Omega} \frac{K(|y-x|)}{|y-x|^2} [(y-x) \cdot (u(y)-u(x))]^2 dy \right)^{1/2} |\theta(x)| dx$$

$$\leq \frac{1}{2\tilde{A}} \int_{\Omega \cup \mathcal{B} \mathcal{B} \Omega} (\theta(x))^2 dx + \tilde{A} \int_{\Omega \cup \mathcal{B} \mathcal{B} \Omega} \int_{\Omega \cup \mathcal{B} \mathcal{B} \Omega} \frac{K(|y-x|)}{|y-x|^2} [(y-x) \cdot (u(y)-u(x))]^2 dy dx, \tag{A.2}$$

where the second inequality comes from the Young's inequality with any positive constant \tilde{A} . We then insert (A.1) into (A.2) to get

$$\int_{\Omega \cup \mathcal{B} \mathcal{B} \Omega} \int_{\Omega \cup \mathcal{B} \mathcal{B} \Omega} K(|y-x|) |(y-x) \cdot (u(y)-u(x)) |dy| \theta(x) |dx
\leq \frac{1}{2\tilde{A}} \int_{\Omega \cup \mathcal{B} \mathcal{B} \Omega} (\theta(x))^2 dx + \tilde{A} \int_{\Omega \cup \mathcal{B} \mathcal{B} \Omega} \int_{\Omega \cup \mathcal{B} \mathcal{B} \Omega} \frac{K(|y-x|)}{|y-x|^2} [(y-x) \cdot (u(y)-u(x))]^2 dy dx
\leq \left(\frac{1}{\tilde{A}} + \tilde{A}\right) \int_{\Omega \cup \mathcal{B} \mathcal{B} \Omega} \int_{\Omega \cup \mathcal{B} \mathcal{B} \Omega} \frac{K(|y-x|)}{|y-x|^2} [(y-x) \cdot (u(y)-u(x))]^2 dy dx.$$
(A.3)

We then prove that any $\mathbf{u} \in S_{H\delta}(\Omega)$ has a bounded total strain energy. Taking $\tilde{A} = 1$, for any $\mathbf{u} \in S_{H\delta}(\Omega)$ its total strain energy satisfies

$$\begin{split} \int_{\Omega \cup \mathcal{B} \mathcal{B} \Omega} W_{\boldsymbol{u}}(\boldsymbol{x}) d\boldsymbol{x} &\leq \int_{\Omega \cup \mathcal{B} \mathcal{B} \Omega} \int_{\Omega \cup \mathcal{B} \mathcal{B} \Omega} (\lambda(\boldsymbol{x}, \boldsymbol{y}) + \mu(\boldsymbol{x}, \boldsymbol{y})) K(|\boldsymbol{y} - \boldsymbol{x}|) |(\boldsymbol{y} - \boldsymbol{x}) \cdot (\boldsymbol{u}(\boldsymbol{y}) - \boldsymbol{u}(\boldsymbol{x})) | d\boldsymbol{y} \, |\boldsymbol{\theta}(\boldsymbol{x}) | d\boldsymbol{x} \\ &+ 4 \int_{\Omega \cup \mathcal{B} \mathcal{B} \Omega} \int_{\Omega \cup \mathcal{B} \mathcal{B} \Omega} \mu(\boldsymbol{x}, \boldsymbol{y}) \frac{K(|\boldsymbol{y} - \boldsymbol{x}|)}{|\boldsymbol{y} - \boldsymbol{x}|^2} [(\boldsymbol{y} - \boldsymbol{x}) \cdot (\boldsymbol{u}(\boldsymbol{y}) - \boldsymbol{u}(\boldsymbol{x}))]^2 d\boldsymbol{y} d\boldsymbol{x} \\ &\leq & (2\lambda_{\infty} + 6\mu_{\infty}) \int_{\Omega \cup \mathcal{B} \mathcal{B} \Omega} \int_{\Omega \cup \mathcal{B} \mathcal{B} \Omega} \frac{K(|\boldsymbol{y} - \boldsymbol{x}|)}{|\boldsymbol{y} - \boldsymbol{x}|^2} [(\boldsymbol{y} - \boldsymbol{x}) \cdot (\boldsymbol{u}(\boldsymbol{y}) - \boldsymbol{u}(\boldsymbol{x}))]^2 d\boldsymbol{y} d\boldsymbol{x} < \infty. \end{split}$$

Meanwhile, for any u satisfying $\int_{\Omega \cup \mathcal{BB}\Omega} W_u(x) dx \leq \infty$, we aim to show that $u \in S_{H\delta}(\Omega)$. In particular,

$$\begin{split} &\int_{\Omega\cup\mathcal{B}\mathcal{B}\Omega}W_{u}(x)dx\\ &=\int_{\Omega\cup\mathcal{B}\mathcal{B}\Omega}\int_{\Omega\cup\mathcal{B}\mathcal{B}\Omega}(\lambda(x,\,y)-\mu(x,\,y))K(|y-x|)(y-x)\cdot(u(y)-u(x))dy\,\theta(x)dx\\ &+4\int_{\Omega\cup\mathcal{B}\mathcal{B}\Omega}\int_{\Omega\cup\mathcal{B}\mathcal{B}\Omega}\mu(x,\,y)\frac{K(|y-x|)}{|y-x|^{2}}[(y-x)\cdot(u(y)-u(x))]^{2}dydx\\ &\geq\int_{\Omega\cup\mathcal{B}\mathcal{B}\Omega}\int_{\Omega\cup\mathcal{B}\mathcal{B}\Omega}\lambda(x,\,y)K(|y-x|)(y-x)\cdot(u(y)-u(x))dy\,\theta(x)dx\\ &+A_{1}\int_{\Omega\cup\mathcal{B}\mathcal{B}\Omega}\int_{\Omega\cup\mathcal{B}\mathcal{B}\Omega}\mu(x,\,y)K(|y-x|)\left[\frac{(y-x)\cdot(u(y)-u(x))}{|y-x|}-\frac{1}{2A_{1}}\,|y-x|\,\theta(x)\right]^{2}dydx\\ &+(4-A_{1})\int_{\Omega\cup\mathcal{B}\mathcal{B}\Omega}\int_{\Omega\cup\mathcal{B}\mathcal{B}\Omega}\mu(x,\,y)\frac{K(|y-x|)}{|y-x|^{2}}[(y-x)\cdot(u(y)-u(x))]^{2}dydx\\ &-\frac{1}{4A_{1}}\int_{\Omega\cup\mathcal{B}\mathcal{B}\Omega}\int_{\Omega\cup\mathcal{B}\mathcal{B}\Omega}\mu(x,\,y)K(|y-x|)\,|y-x|^{2}\,dy(\theta(x))^{2}dx. \end{split}$$

Since for d = 2 and with (2.1) we have

$$\begin{split} &-\int_{\Omega \cup \mathcal{B} \mathcal{B} \Omega} \int_{\Omega \cup \mathcal{B} \mathcal{B} \Omega} \mu(\boldsymbol{x}, \boldsymbol{y}) K(|\boldsymbol{y} - \boldsymbol{x}|) \, |\boldsymbol{y} - \boldsymbol{x}|^2 \, d\boldsymbol{y} (\theta(\boldsymbol{x}))^2 d\boldsymbol{x} \\ &\geq -\mu_{\infty} \int_{\Omega \cup \mathcal{B} \mathcal{B} \Omega} \int_{\Omega \cup \mathcal{B} \mathcal{B} \Omega} K(|\boldsymbol{y} - \boldsymbol{x}|) \, |\boldsymbol{y} - \boldsymbol{x}|^2 \, d\boldsymbol{y} (\theta(\boldsymbol{x}))^2 d\boldsymbol{x} = -2\mu_{\infty} \int_{\Omega \cup \mathcal{B} \mathcal{B} \Omega} (\theta(\boldsymbol{x}))^2 d\boldsymbol{x}, \end{split}$$

and by taking $\tilde{A} = A_0(\lambda_{\infty} - \lambda_0)$ in (A.2)

$$\begin{split} &\int_{\varOmega\cup\mathcal{B}\mathcal{B}\varOmega}\int_{\varOmega\cup\mathcal{B}\mathcal{B}\varOmega}\lambda(x,y)K(|y-x|)[(y-x)\cdot(u(y)-u(x))]dy\,\theta(x)dx\\ =&\int_{\varOmega\cup\mathcal{B}\mathcal{B}\varOmega}\int_{\varOmega\cup\mathcal{B}\mathcal{B}\varOmega}(\lambda(x,y)-\lambda_{\infty})K(|y-x|)[(y-x)\cdot(u(y)-u(x))]dy\,\theta(x)dx+\lambda_{\infty}\int_{\varOmega\cup\mathcal{B}\mathcal{B}\varOmega}(\theta(x))^{2}dx\\ \geq&\lambda_{\infty}\int_{\varOmega\cup\mathcal{B}\mathcal{B}\varOmega}(\theta(x))^{2}dx-(\lambda_{\infty}-\lambda_{0})\int_{\varOmega\cup\mathcal{B}\mathcal{B}\varOmega}\int_{\varOmega\cup\mathcal{B}\mathcal{B}\varOmega}K(|y-x|)|(y-x)\cdot(u(y)-u(x))|dy\,|\theta(x)|dx\\ \geq&\left(\lambda_{\infty}-\frac{(\lambda_{\infty}-\lambda_{0})}{2A_{0}}\right)\int_{\varOmega\cup\mathcal{B}\mathcal{B}\varOmega}(\theta(x))^{2}dx-A_{0}(\lambda_{\infty}-\lambda_{0})\\ &\times\int_{\varOmega\cup\mathcal{B}\mathcal{B}\varOmega}\int_{\varOmega\cup\mathcal{B}\mathcal{B}\varOmega}\frac{K(|y-x|)}{|y-x|^{2}}[(y-x)\cdot(u(y)-u(x))]^{2}dydx, \end{split}$$

substituting the above two inequalities yields:

$$\begin{split} &\int_{\Omega \cup \mathcal{B} \mathcal{B} \Omega} W_{\boldsymbol{u}}(\boldsymbol{x}) d\boldsymbol{x} \\ &\geq A_1 \int_{\Omega \cup \mathcal{B} \mathcal{B} \Omega} \int_{\Omega \cup \mathcal{B} \mathcal{B} \Omega} \mu(\boldsymbol{x}, \boldsymbol{y}) K(|\boldsymbol{y} - \boldsymbol{x}|) \left[\frac{(\boldsymbol{y} - \boldsymbol{x}) \cdot (\boldsymbol{u}(\boldsymbol{y}) - \boldsymbol{u}(\boldsymbol{x}))}{|\boldsymbol{y} - \boldsymbol{x}|} - \frac{1}{2A_1} |\boldsymbol{y} - \boldsymbol{x}| \, \theta(\boldsymbol{x}) \right]^2 d\boldsymbol{y} d\boldsymbol{x} \\ &+ ((4 - A_1)\mu_0 - A_0(\lambda_\infty - \lambda_0)) \int_{\Omega \cup \mathcal{B} \mathcal{B} \Omega} \int_{\Omega \cup \mathcal{B} \mathcal{B} \Omega} \frac{K(|\boldsymbol{y} - \boldsymbol{x}|)}{|\boldsymbol{y} - \boldsymbol{x}|^2} [(\boldsymbol{y} - \boldsymbol{x}) \cdot (\boldsymbol{u}(\boldsymbol{y}) - \boldsymbol{u}(\boldsymbol{x}))]^2 d\boldsymbol{y} d\boldsymbol{x} \\ &+ \left(\lambda_\infty - \frac{\lambda_\infty - \lambda_0}{2A_0} - \frac{\mu_\infty}{2A_1} \right) \int_{\Omega \cup \mathcal{B} \mathcal{B} \Omega} (\theta(\boldsymbol{x}))^2 d\boldsymbol{x} \\ \geq &((4 - A_1)\mu_0 - A_0(\lambda_\infty - \lambda_0)) \int_{\Omega \cup \mathcal{B} \mathcal{B} \Omega} \int_{\Omega \cup \mathcal{B} \mathcal{B} \Omega} \frac{K(|\boldsymbol{y} - \boldsymbol{x}|)}{|\boldsymbol{y} - \boldsymbol{x}|^2} [(\boldsymbol{y} - \boldsymbol{x}) \cdot (\boldsymbol{u}(\boldsymbol{y}) - \boldsymbol{u}(\boldsymbol{x}))]^2 d\boldsymbol{y} d\boldsymbol{x}. \end{split}$$

Therefore,
$$\int_{\Omega \cup \mathcal{BB}\Omega} \int_{\Omega \cup \mathcal{BB}\Omega} \frac{K(|y-x|)}{|y-x|^2} [(y-x) \cdot (u(y)-u(x))]^2 dy dx < \infty \text{ and } u \in S_{H\delta}(\Omega).$$

Remark 4. Note that the above derivation also holds for the local extremes of $\lambda(\cdot, \cdot)$ and $\mu(\cdot, \cdot)$. Therefore an alternative (local) form of Assumption 1 writes:

$$(4 - A_1)\mu_0(\mathbf{x}) - A_0(\lambda_\infty(\mathbf{x}) - \lambda_0(\mathbf{x})) > 0, \tag{A.4}$$

$$\lambda_{\infty}(\mathbf{x}) - \frac{\lambda_{\infty}(\mathbf{x}) - \lambda_0(\mathbf{x})}{2A_0} - \frac{\mu_{\infty}(\mathbf{x})}{2A_1} \ge 0,\tag{A.5}$$

for any $x \in \Omega \cup \mathcal{BB}\Omega$, where

$$\lambda_{\infty}(\textbf{\textit{x}}) := \sup_{\textbf{\textit{y}} \in B_{\delta}(\textbf{\textit{x}}) \cap (\varOmega \cup \mathcal{BB}\Omega)} \lambda(\textbf{\textit{x}}, \textbf{\textit{y}}), \ \lambda_{0}(\textbf{\textit{x}}) := \inf_{\textbf{\textit{y}} \in B_{\delta}(\textbf{\textit{x}}) \cap (\varOmega \cup \mathcal{BB}\Omega)} \lambda(\textbf{\textit{x}}, \textbf{\textit{y}}),$$

$$\mu_{\infty}(\mathbf{x}) := \sup_{\mathbf{y} \in B_{\delta}(\mathbf{x}) \cap (\Omega \cup \mathcal{BB}\Omega)} \mu(\mathbf{x}, \mathbf{y}), \ \mu_{0}(\mathbf{x}) := \inf_{\mathbf{y} \in B_{\delta}(\mathbf{x}) \cap (\Omega \cup \mathcal{BB}\Omega)} \mu(\mathbf{x}, \mathbf{y}).$$

If further assuming that $\lambda(\cdot)$, $\mu(\cdot) \in C(\overline{\Omega \cup \mathcal{BB}\Omega})$, we will have

$$\sup_{x \in \Omega \cup \mathcal{BB}\Omega} \sup_{y,z \in B_{\delta}(x) \cap (\Omega \cup \mathcal{BB}\Omega)} |\lambda(x,y) - \lambda(x,z)| \leq C_1 \delta,$$

$$\sup_{\boldsymbol{x} \in \Omega \cup \mathcal{BB}\Omega} \sup_{\boldsymbol{y}, \boldsymbol{z} \in B_{\delta}(\boldsymbol{x}) \cap (\Omega \cup \mathcal{BB}\Omega)} |\mu(\boldsymbol{x}, \boldsymbol{y}) - \mu(\boldsymbol{x}, \boldsymbol{z})| \leq C_2 \delta,$$

for generic constant C_1 and C_2 which are independent of δ . Then Assumption 1 can be relaxed to:

$$(4 - A_1)\mu_0(\mathbf{x}) > A_0 C_1 \delta, \ \lambda_\infty(\mathbf{x}) - \frac{\mu_\infty(\mathbf{x})}{2A_1} \ge \frac{C_2 \delta}{2A_0}. \tag{A.6}$$

A.2. Proof of Lemma 5

In this section we provide detailed truncation estimates for the proposed LPS formulations. We consider the heterogeneous LPS formulation with full Dirichlet-type boundary conditions, proposed in (2.3) and (2.5). In particular, before showing the proof of Lemma 5, we first show that the nonlocal dilatation θ is consistent with the local dilatation with the following lemma.

Lemma 7. Assume that $\mathbf{u} \in C^4(\overline{\Omega \cup \mathcal{BB}\Omega})$, then there exists $\overline{\delta} > 0$ such that for any $0 < \delta \leq \overline{\delta}$,

$$\theta(\mathbf{x}) - \nabla \cdot \mathbf{u}(\mathbf{x}) = D_1 \left(\frac{\partial^3 u_1}{\partial x_1^3} (\mathbf{x}) + \frac{\partial^3 u_2}{\partial x_2^3} (\mathbf{x}) \right) + 3D_2 \left(\frac{\partial^3 u_1}{\partial x_1 \partial x_2^2} (\mathbf{x}) + \frac{\partial^3 u_2}{\partial x_1^2 \partial x_2} (\mathbf{x}) \right) + O(\delta^3) = O(\delta^2),$$

for all $x \in \Omega \cup B\Omega$. Here

$$D_1 := \int_{B_{\delta}(\mathbf{x})} K(|\mathbf{y} - \mathbf{x}|) (y_1 - x_1)^4 d\mathbf{y} = O(\delta^2), \quad D_2 := \int_{B_{\delta}(\mathbf{x})} K(|\mathbf{y} - \mathbf{x}|) (y_1 - x_1)^2 (y_2 - x_2)^2 d\mathbf{y} = O(\delta^2).$$

Proof. Denote $\mathbf{x} = (x_1, x_2)$ where x_1 and x_2 are the coordinate components along the horizontal and vertical axes, respectively, and u_1 , u_2 as the displacement components along the x_1 and x_2 directions, respectively. For simplicity, in the following we use K to represent $K(|\mathbf{y} - \mathbf{x}|)$ when there is no confusion. For $\mathbf{u} \in C^4$ and $\mathbf{x} \in \Omega \cup \mathcal{B}\Omega$, with the symmetry of $B_{\delta}(\mathbf{x})$ we have

$$\begin{aligned} &\theta(\boldsymbol{x}) - \nabla \cdot \boldsymbol{u}(\boldsymbol{x}) \\ &= O(\delta^3) + \int_{B_{\delta}(\boldsymbol{x})} K(y_1 - x_1)^2 \left(\frac{\partial u_1}{\partial x_1}(\boldsymbol{x}) + (y_1 - x_1)^2 \frac{\partial^3 u_1}{\partial x_1^3}(\boldsymbol{x}) + 3(y_2 - x_2)^2 \frac{\partial^3 u_1}{\partial x_1 \partial x_2^2}(\boldsymbol{x}) \right) d\boldsymbol{y} \\ &+ \int_{B_{\delta}(\boldsymbol{x})} K(y_2 - x_2)^2 \left(\frac{\partial u_2}{\partial x_2}(\boldsymbol{x}) + (y_2 - x_2)^2 \frac{\partial^3 u_2}{\partial x_2^3}(\boldsymbol{x}) + 3(y_1 - x_1)^2 \frac{\partial^3 u_2}{\partial x_1^2 \partial x_2}(\boldsymbol{x}) \right) d\boldsymbol{y} - \frac{\partial u_1}{\partial x_1}(\boldsymbol{x}) - \frac{\partial u_2}{\partial x_2}(\boldsymbol{x}) \\ &= O(\delta^3) + D_1 \left(\frac{\partial^3 u_1}{\partial x_1^3}(\boldsymbol{x}) + \frac{\partial^3 u_2}{\partial x_1^2}(\boldsymbol{x}) \right) + 3D_2 \left(\frac{\partial^3 u_1}{\partial x_1 \partial x_2^2}(\boldsymbol{x}) + \frac{\partial^3 u_2}{\partial x_1^2 \partial x_2}(\boldsymbol{x}) \right). \quad \Box \end{aligned}$$

We now proceed to the proof of Lemma 5:

Proof. We again adopt the coordinate system as in the proof of Lemma 7 and denote the two components of u as u_1 and u_2 . We notice that

$$\lambda(x, y) - \lambda(x) = \frac{\lambda(x)(\lambda(y) - \lambda(x))}{\lambda(x) + \lambda(y)} = \frac{(\lambda(y) - \lambda(x))}{2} \left(1 + \frac{(\lambda(y) - \lambda(x))}{2\lambda(x)} + O\left(\frac{(\lambda(y) - \lambda(x))}{2\lambda(x)}\right)^2 \right)$$

$$= \frac{(\lambda(y) - \lambda(x))}{2} + O\left(\left(\lambda(y) - \lambda(x)\right)\right)^2 = \frac{1}{2} \nabla \lambda(x) \cdot (y - x) + O(\delta^2)$$
(A.7)

and similarly

$$\mu(\mathbf{x}, \mathbf{y}) - \mu(\mathbf{x}) = \frac{1}{2} \nabla \mu(\mathbf{x}) \cdot (\mathbf{y} - \mathbf{x}) + O(\delta^2). \tag{A.8}$$

The bound of $\mathcal{L}_{H0}u - \mathcal{L}_{H\delta}u$ can then be obtained via Lemma 7, Taylor expansion of u and the symmetry of $B_{\delta}(x)$:

$$\mathcal{L}_{H0}(\boldsymbol{u})(\boldsymbol{x}) - \mathcal{L}_{H\delta}(\boldsymbol{u})(\boldsymbol{x})$$

$$= -\frac{1}{2}\nabla \cdot \left[\lambda(\boldsymbol{x})\operatorname{tr}(\nabla \boldsymbol{u}(\boldsymbol{x}) + (\nabla \boldsymbol{u}(\boldsymbol{x}))^{T})\mathbf{I} + 2\mu(\boldsymbol{x})(\nabla \boldsymbol{u}(\boldsymbol{x}) + (\nabla \boldsymbol{u}(\boldsymbol{x}))^{T})\right]$$

$$+ \int_{B_{\delta}(\boldsymbol{x})} (\lambda(\boldsymbol{x}, \boldsymbol{y}) - \mu(\boldsymbol{x}, \boldsymbol{y})) K (\boldsymbol{y} - \boldsymbol{x}) \left(\nabla \cdot \boldsymbol{u}(\boldsymbol{x}) + \nabla \cdot \boldsymbol{u}(\boldsymbol{y}) + D_{1} \left(\frac{\partial^{3} u_{1}}{\partial x_{1}^{3}}(\boldsymbol{x}) + \frac{\partial^{3} u_{2}}{\partial x_{2}^{3}}(\boldsymbol{x})\right) + 3D_{2} \left(\frac{\partial^{3} u_{1}}{\partial x_{1} \partial x_{2}^{2}}(\boldsymbol{x}) + \frac{\partial^{3} u_{2}}{\partial x_{1}^{2} \partial x_{2}}(\boldsymbol{x}) + \frac{\partial^{3} u_{1}}{\partial x_{1} \partial x_{2}^{2}}(\boldsymbol{y}) + \frac{\partial^{3} u_{2}}{\partial x_{1}^{2} \partial x_{2}}(\boldsymbol{y})\right)\right) d\boldsymbol{y}$$

$$+ 8 \int_{B_{\delta}(\boldsymbol{x})} \mu(\boldsymbol{x}, \boldsymbol{y}) K \frac{(\boldsymbol{y} - \boldsymbol{x}) \otimes (\boldsymbol{y} - \boldsymbol{x})}{|\boldsymbol{y} - \boldsymbol{x}|^{2}} (\boldsymbol{u}(\boldsymbol{y}) - \boldsymbol{u}(\boldsymbol{x})) d\boldsymbol{y} + O(\delta^{2})$$

$$= -\frac{1}{2}\nabla \cdot \left[\lambda(\boldsymbol{x})\operatorname{tr}(\nabla \boldsymbol{u}(\boldsymbol{x}) + (\nabla \boldsymbol{u}(\boldsymbol{x}))^{T})\mathbf{I} + 2\mu(\boldsymbol{x})(\nabla \boldsymbol{u}(\boldsymbol{x}) + (\nabla \boldsymbol{u}(\boldsymbol{x}))^{T})\right]$$

$$+ \int_{B_{\delta}(\boldsymbol{x})} (\lambda(\boldsymbol{x}, \boldsymbol{y}) - \mu(\boldsymbol{x}, \boldsymbol{y})) K (\boldsymbol{y} - \boldsymbol{x}) (\nabla \cdot \boldsymbol{u}(\boldsymbol{x}) + \nabla \cdot \boldsymbol{u}(\boldsymbol{y})) d\boldsymbol{y}$$

$$+ 8 \int_{B_{\delta}(\boldsymbol{x})} \mu(\boldsymbol{x}, \boldsymbol{y}) K \frac{(\boldsymbol{y} - \boldsymbol{x}) \otimes (\boldsymbol{y} - \boldsymbol{x})}{|\boldsymbol{y} - \boldsymbol{x}|^{2}} (\boldsymbol{u}(\boldsymbol{y}) - \boldsymbol{u}(\boldsymbol{x})) d\boldsymbol{y} + O(\delta^{2})$$

Hence, by using (A.7) and (A.8) and their asymptotic orders in terms of δ , and the symmetry of $B_{\delta}(x)$, we have

$$\mathcal{L}_{H0}(\boldsymbol{u})(\boldsymbol{x}) - \mathcal{L}_{H\delta}(\boldsymbol{u})(\boldsymbol{x})$$

$$= -\frac{1}{2}\lambda(\boldsymbol{x})\nabla \cdot (tr(\nabla \boldsymbol{u}(\boldsymbol{x}) + (\nabla \boldsymbol{u}(\boldsymbol{x}))^{T})\mathbf{I} - \mu(\boldsymbol{x})\nabla \cdot (\nabla \boldsymbol{u}(\boldsymbol{x}) + (\nabla \boldsymbol{u}(\boldsymbol{x}))^{T}))$$

$$- (\nabla \cdot \lambda(\boldsymbol{x})\mathbf{I})\nabla \cdot \boldsymbol{u}(\boldsymbol{x}) - \nabla \mu(\boldsymbol{x}) \cdot (\nabla \boldsymbol{u}(\boldsymbol{x}) + (\nabla \boldsymbol{u}(\boldsymbol{x}))^{T})$$

$$+ (\lambda(\boldsymbol{x}) - \mu(\boldsymbol{x})) \int_{B_{\delta}(\boldsymbol{x})} K(\boldsymbol{y} - \boldsymbol{x}) (\nabla \cdot \boldsymbol{u}(\boldsymbol{x}) + \nabla \cdot \boldsymbol{u}(\boldsymbol{y})) d\boldsymbol{y}$$

$$+ \frac{1}{2} \int_{B_{\delta}(\boldsymbol{x})} (\nabla \lambda(\boldsymbol{x}) - \nabla \mu(\boldsymbol{x})) \cdot (\boldsymbol{y} - \boldsymbol{x}) K(\boldsymbol{y} - \boldsymbol{x}) (\nabla \cdot \boldsymbol{u}(\boldsymbol{x}) + \nabla \cdot \boldsymbol{u}(\boldsymbol{y})) d\boldsymbol{y}$$

$$+ 8\mu(\boldsymbol{x}) \int_{B_{\delta}(\boldsymbol{x})} K \frac{(\boldsymbol{y} - \boldsymbol{x}) \otimes (\boldsymbol{y} - \boldsymbol{x})}{|\boldsymbol{y} - \boldsymbol{x}|^{2}} (\boldsymbol{u}(\boldsymbol{y}) - \boldsymbol{u}(\boldsymbol{x})) d\boldsymbol{y}$$

$$+ 4 \int_{B_{\delta}(\boldsymbol{x})} (\nabla \mu(\boldsymbol{x}) \cdot (\boldsymbol{y} - \boldsymbol{x})) K \frac{(\boldsymbol{y} - \boldsymbol{x}) \otimes (\boldsymbol{y} - \boldsymbol{x})}{|\boldsymbol{y} - \boldsymbol{x}|^{2}} (\boldsymbol{u}(\boldsymbol{y}) - \boldsymbol{u}(\boldsymbol{x})) d\boldsymbol{y}$$

$$= - (\nabla \cdot \lambda(\boldsymbol{x})\mathbf{I})\nabla \cdot \boldsymbol{u}(\boldsymbol{x}) - \nabla \mu(\boldsymbol{x}) \cdot (\nabla \boldsymbol{u}(\boldsymbol{x}) + (\nabla \boldsymbol{u}(\boldsymbol{x}))^{T})$$

$$+ (\nabla \lambda(\boldsymbol{x}) - \nabla \mu(\boldsymbol{x})) \cdot (\nabla \cdot \boldsymbol{u}(\boldsymbol{x})) \int_{B_{\delta}(\boldsymbol{x})} \left(K(y_{1} - x_{1})^{2} / K(y_{2} - x_{2})^{2} \right) d\boldsymbol{y}$$

$$+ 4 \int_{B_{\delta}(\boldsymbol{x})} (\nabla \mu(\boldsymbol{x}) \cdot (\boldsymbol{y} - \boldsymbol{x})) K \frac{(\boldsymbol{y} - \boldsymbol{x}) \otimes (\boldsymbol{y} - \boldsymbol{x})}{|\boldsymbol{y} - \boldsymbol{x}|^{2}} (\boldsymbol{u}(\boldsymbol{y}) - \boldsymbol{u}(\boldsymbol{x})) d\boldsymbol{y} + O(\delta^{2}) = O(\delta^{2}). \quad \Box$$

A.3. Proof of Theorem 2

In this section, we provide the detailed proof for the compatibility results demonstrated in Theorem 2.

Proof. We first show the proof of (2.13). Since u_{δ} is a solution to the nonlocal problem, we have

$$T_{H\delta}[\boldsymbol{u}_{\delta}, \boldsymbol{v}; \lambda, \mu] = \langle \boldsymbol{f}, \boldsymbol{v} \rangle \leq \|\boldsymbol{f}\|_{(S_{H\delta}(\Omega))^*} \|\boldsymbol{v}\|_{S_{H\delta}(\Omega)}$$

for any test function $\mathbf{v} \in S_{H\delta}(\Omega)$. Now let $\mathbf{v} = \mathbf{u}_{\delta}$, we get $r \|\mathbf{u}_{\delta}\|_{S_{H\delta}(\Omega)}^2 \le T_{H\delta}[\mathbf{u}_{\delta}, \mathbf{u}_{\delta}] \le \|\mathbf{f}\|_{(S_{H\delta}(\Omega))^*} \|\mathbf{u}_{\delta}\|_{S_{H\delta}(\Omega)}$. Therefore, we have (2.13).

The proof of the second part involves two steps. In the first step, we assume $\lambda(\cdot)$, $\mu(\cdot) \in C^2(\overline{\Omega \cup \mathcal{BB}\Omega})$, then from Lemma 5, we know that $\mathcal{L}_{H\delta} v$ converges to $\mathcal{L}_0 v$ uniformly on Ω for $v \in C_0^{\infty}(\Omega)$ as $\delta \to 0$. Notice that from the assumption on $||f||_{(S_{H\delta}(\Omega))^*}$, we have $||u_{\delta}||_{S_{H\delta}(\Omega)}$ being uniformly bounded for all $\delta \in (0, \overline{\delta})$. Then using similar arguments in [52] together with the compactness result [88, Lemma 7], we can show $||u_{\delta} - u_0||_{L^2(\Omega;\mathbb{R}^d)} \to 0$ as $\delta \to 0$.

For the general case that $\lambda, \mu \in C(\overline{\Omega \cup \mathcal{BB}\Omega})$, we will use the mollification technique. First notice that we can extend λ and μ continuously to a larger domain that contains $\overline{\Omega \cup \mathcal{BB}\Omega}$. Then we can take standard mollifiers $\phi^{\epsilon} \in C^{\infty}(\mathbb{R}^{d})$, and define $\lambda^{\epsilon} = \phi^{\epsilon} * \lambda$ and $\mu^{\epsilon} = \phi^{\epsilon} * \mu$ on $\overline{\Omega \cup \mathcal{BB}\Omega}$ for small enough $\epsilon > 0$. We denote the solution to (2.9) associated with coefficient $\lambda^{\epsilon}(x, y) := 2((\lambda^{\epsilon}(x))^{-1} + (\lambda^{\epsilon}(y))^{-1})^{-1}$ and $\mu^{\epsilon}(x, y) := 2((\mu^{\epsilon}(x))^{-1} + (\mu^{\epsilon}(y))^{-1})^{-1}$ to be $u_{\delta,\epsilon}$. Then we can use the first step to conclude that $\|u_{\delta,\epsilon} - u_{0,\epsilon}\|_{L^{2}(\Omega;\mathbb{R}^{d})} \xrightarrow{\delta \to 0} 0$, where $u_{0,\epsilon}$ is the solution to (2.12) associated with coefficient λ^{ϵ} and μ^{ϵ} . Now in order to show $\|u_{\delta} - u_{0}\|_{L^{2}(\Omega;\mathbb{R}^{d})} \to 0$, we notice that

$$\lim_{\delta\to 0}\|\boldsymbol{u}_{\delta}-\boldsymbol{u}_{0}\|_{L^{2}(\Omega;\mathbb{R}^{d})}\leq \sup_{\delta\in (0,\overline{\delta})}\|\boldsymbol{u}_{\delta,\epsilon}-\boldsymbol{u}_{\delta}\|_{L^{2}(\Omega;\mathbb{R}^{d})}+\lim_{\delta\to 0}\|\boldsymbol{u}_{\delta,\epsilon}-\boldsymbol{u}_{0,\epsilon}\|_{L^{2}(\Omega;\mathbb{R}^{d})}+\|\boldsymbol{u}_{0,\epsilon}-\boldsymbol{u}_{0}\|_{L^{2}(\Omega;\mathbb{R}^{d})},$$

for any $\epsilon > 0$. Therefore, we only need to show

$$\begin{cases} \lim_{\epsilon \to 0} \sup_{\delta \in (0,\overline{\delta})} \|\boldsymbol{u}_{\delta,\epsilon} - \boldsymbol{u}_{\delta}\|_{L^{2}(\Omega;\mathbb{R}^{d})} = 0, & \text{and} \\ \lim_{\epsilon \to 0} \|\boldsymbol{u}_{0,\epsilon} - \boldsymbol{u}_{0}\|_{L^{2}(\Omega;\mathbb{R}^{d})} = 0. \end{cases}$$
(A.9)

Notice that $\|\lambda^{\epsilon} - \lambda\|_{C(\overline{\Omega \cup \mathcal{B}B\Omega})} \to 0$ and $\|\mu^{\epsilon} - \mu\|_{C(\overline{\Omega \cup \mathcal{B}B\Omega})} \to 0$ as $\epsilon \to 0$ since λ and μ are continuous. Then $\lambda^{\epsilon}(x, y) \to \lambda(x, y)$ and $\mu^{\epsilon}(x, y) \to \mu(x, y)$ uniformly on $(\overline{\Omega \cup \mathcal{B}B\Omega})^2$ as $\epsilon \to 0$. For this, we simply write $\|\lambda^{\epsilon} - \lambda\|_{C((\overline{\Omega \cup \mathcal{B}B\Omega})^2)} \to 0$ and $\|\mu^{\epsilon} - \mu\|_{C((\overline{\Omega \cup \mathcal{B}B\Omega})^2)} \to 0$ where the functions λ^{ϵ} , λ , μ^{ϵ} and μ are continuous functions of the two variables $x \in \overline{\Omega \cup \mathcal{B}B\Omega}$ and $y \in \overline{\Omega \cup \mathcal{B}B\Omega}$. Now for the first equation in (A.9), notice that since $u_{\delta,\epsilon}$ and u_{δ} are solutions to (2.9) with different coefficients and the same right-hand side, we have

$$T_{H\delta}[\boldsymbol{u}_{\delta,\epsilon} - \boldsymbol{u}_{\delta}, \boldsymbol{v}; \lambda^{\epsilon}, \mu^{\epsilon}] = T_{H\delta}[\boldsymbol{u}_{\delta}, \boldsymbol{v}; \lambda - \lambda^{\epsilon}, \mu - \mu^{\epsilon}] =: \langle \boldsymbol{g}_{\delta,\epsilon}, \boldsymbol{v} \rangle,$$

for any $\mathbf{v} \in S_{H\delta}(\Omega)$. We can show $\langle \mathbf{g}_{\delta,\epsilon}, \mathbf{v} \rangle \to 0$ as $\epsilon \to 0$ uniformly independent of δ since

$$\begin{split} & \langle \boldsymbol{g}_{\delta,\epsilon}, \boldsymbol{v} \rangle \\ & \leq \left(\| \boldsymbol{\lambda}^{\epsilon} - \boldsymbol{\lambda} \|_{C((\overline{\Omega \cup \mathcal{B}B\Omega})^{2})} + \| \boldsymbol{\mu}^{\epsilon} - \boldsymbol{\mu} \|_{C((\overline{\Omega \cup \mathcal{B}B\Omega})^{2})} \right) \iint_{(\Omega \cup \mathcal{B}B\Omega)^{2}} K(|\boldsymbol{y} - \boldsymbol{x}|) | \, (\boldsymbol{y} - \boldsymbol{x}) \cdot (\boldsymbol{v}(\boldsymbol{y}) - \boldsymbol{v}(\boldsymbol{x})) \, | d\boldsymbol{y} \, | \theta_{\delta}(\boldsymbol{x}) | d\boldsymbol{x} \\ & + 4 \| \boldsymbol{\mu}^{\epsilon} - \boldsymbol{\mu} \|_{C((\overline{\Omega \cup \mathcal{B}B\Omega})^{2})} \iint_{(\Omega \cup \mathcal{B}B\Omega)^{2}} \frac{K(|\boldsymbol{y} - \boldsymbol{x}|)}{|\boldsymbol{y} - \boldsymbol{x}|^{2}} | \, (\boldsymbol{y} - \boldsymbol{x}) \cdot (\boldsymbol{u}_{\delta}(\boldsymbol{y}) - \boldsymbol{u}_{\delta}(\boldsymbol{x})) \, || \, (\boldsymbol{y} - \boldsymbol{x}) \cdot (\boldsymbol{v}(\boldsymbol{y}) - \boldsymbol{v}(\boldsymbol{x})) \, | d\boldsymbol{y} d\boldsymbol{x} \\ & \leq 5 \left(\| \boldsymbol{\lambda}^{\epsilon} - \boldsymbol{\lambda} \|_{C((\overline{\Omega \cup \mathcal{B}B\Omega})^{2})} + \| \boldsymbol{\mu}^{\epsilon} - \boldsymbol{\mu} \|_{C((\overline{\Omega \cup \mathcal{B}B\Omega})^{2})} \right) \| \boldsymbol{u}_{\delta} \|_{S_{H\delta}(\Omega)} \| \boldsymbol{v} \|_{S_{H\delta}(\Omega)}. \end{split}$$

Now use the coercivity of $T_{H\delta}$ and $\|\boldsymbol{u}_{\delta}\|_{S_{H\delta}(\Omega)} \leq C$ from (2.13), we have

$$\begin{split} \sup_{\delta \in (0,\overline{\delta})} \| \boldsymbol{u}_{\delta,\epsilon} - \boldsymbol{u}_{\delta} \|_{S_{H\delta}(\Omega)} &\leq C \sup_{\delta \in (0,\overline{\delta})} \| \boldsymbol{g}_{\delta,\epsilon} \|_{(S_{H\delta}(\Omega))^*} \\ &\leq C \left(\| \lambda^{\epsilon} - \lambda \|_{C((\overline{\Omega \cup \mathcal{BB\Omega}})^2)} + \| \mu^{\epsilon} - \mu \|_{C((\overline{\Omega \cup \mathcal{BB\Omega}})^2)} \right) \to 0 \text{ as } \epsilon \to 0 \end{split}$$

and the convergence in L^2 is then implied from the Poincaré inequality in Lemma 3. The proof for the second equation in (A.9) can be similarly done. \Box

A.4. Proof of Lemma 6

In this section, we provide the detailed proof for the bound in Lemma 6.

Proof. The inequality is shown by taking w to be the truncated Chebyshev expansion of v up to degree p which follows the proof of [101, Lemma 4.4]. Since our functions are vector valued, we show the proof of the inequality for completeness. Let $\{T_k(t)\}_{k=1}^{\infty}$ be the Chebyshev polynomials on [-1, 1], then the expansion of $v(x, t) = v(x, \cos(t))$ in t is given by

$$\mathbf{v}(\mathbf{x},t) = \frac{\mathbf{a}_0(\mathbf{x})}{2} + \sum_{k=1}^{\infty} \mathbf{a}_k(\mathbf{x}) T_k(t)$$

where $a_k \in S_{H\delta}(\Omega)$, k = 0, 1, ..., are given by

$$\boldsymbol{a}_k(\boldsymbol{x}) = \frac{1}{\pi} \int_{-\pi}^{\pi} \boldsymbol{v}(\boldsymbol{x}, \cos(s)) \cos(ks) ds.$$

The Chebyshev series has an analytic extension which converges in any open elliptic disk delimited by the ellipse E_{ϱ} with foci ± 1 and the sum of the half-axes ϱ (see e.g. [113]). Let $\mathbf{w} = a_0(\mathbf{x})/2 + \sum_{k=1}^p \mathbf{a}_k(\mathbf{x})T_k(t)$, then

$$\|\boldsymbol{v}-\boldsymbol{w}\|_{C(\Gamma^1;S_{H\delta}(\Omega))} \leq \sum_{k=q+1}^{\infty} \|\boldsymbol{a}_k\|_{S_{H\delta}(\Omega)} = \sum_{k=q+1}^{\infty} \|\boldsymbol{a}_k\|_{S_{H\delta}(\Omega;\mathbb{C}^d)}.$$

Now for any $\hat{\rho}$ with $1 < \hat{\rho} < \rho$, following the arguments of [113, Chapter 7, Theorem 8.1], one can rewrite a_k as

$$\boldsymbol{a}_{k}(\boldsymbol{x}) = \frac{1}{2\pi i} \int_{C_{1}} \boldsymbol{v}\left(\boldsymbol{x}, \frac{z+z^{-1}}{2}\right) z^{k-1} dz + \frac{1}{2\pi i} \int_{C_{2}} \boldsymbol{v}\left(\boldsymbol{x}, \frac{z+z^{-1}}{2}\right) z^{-k-1} dz$$
(A.10)

where $C_1 := \{z \in \mathbb{C} : |z| = \hat{\varrho}^{-1}\}$ and $C_2 := \{z \in \mathbb{C} : |z| = \hat{\varrho}\}$. Now we do change of variables with $z = \hat{\varrho}^{-1}e^{is}$ for the first integral in (A.10) and $z = \hat{\varrho}e^{is}$ for the second integral in (A.10), we get

$$\boldsymbol{a}_{k}(\boldsymbol{x}) = \frac{1}{2\pi} \int_{-\pi}^{\pi} \boldsymbol{v}\left(\boldsymbol{x}, \hat{\varrho}^{-1}\cos(s)\right) \hat{\varrho}^{-k} e^{iks} ds + \frac{1}{2\pi} \int_{-\pi}^{\pi} \boldsymbol{v}\left(\boldsymbol{x}, \hat{\varrho}\cos(s)\right) \hat{\varrho}^{-k} e^{-iks} ds. \tag{A.11}$$

Using (A.11), it is then easy to see that

$$\|\boldsymbol{a}_{k}\|_{S_{H\delta}(\Omega;\mathbb{C}^{d})} \leq 2\hat{\varrho}^{-k} \max_{z \in \mathcal{A}(\Gamma^{1},\tau)} \|\boldsymbol{v}(\cdot,z)\|_{S_{H\delta}(\Omega;\mathbb{C}^{d})}.$$

So

$$\|\boldsymbol{v}-\boldsymbol{w}\|_{C(\Gamma^1;S_{H\delta}(\Omega))} \leq \sum_{k=q+1}^{\infty} \|\boldsymbol{a}_k\|_{S_{H\delta}(\Omega;\mathbb{C}^d)} \leq \frac{2}{\hat{\varrho}-1} \hat{\varrho}^{-p} \max_{z \in \mathcal{A}(\Gamma^1,\tau)} \|\boldsymbol{v}(\cdot,z)\|_{S_{H\delta}(\Omega;\mathbb{C}^d)}.$$

Taking $\hat{\varrho} \to \varrho$, we get the desired result. \square

References

- [1] T. Zohdi, D. Steigmann, The toughening effect of microscopic filament misalignment on macroscopic ballistic fabric response, Int. J. Fract. 118 (4) (2002) 71–76.
- [2] P. Wriggers, G. Zavarise, T. Zohdi, A computational study of interfacial debonding damage in fibrous composite materials, Comput. Mater. Sci. 12 (1) (1998) 39–56.
- [3] E.E. Prudencio, P.T. Bauman, S. Williams, D. Faghihi, K. Ravi-Chandar, J.T. Oden, A dynamic data driven application system for real-time monitoring of stochastic damage, Procedia Comput. Sci. 18 (2013) 2056–2065.
- [4] Z. Su, L. Ye, Y. Lu, Guided lamb waves for identification of damage in composite structures: A review, J. Sound Vib. 295 (3-5) (2006) 753-780.
- [5] 2014 Technical Strategic Plan, Tech. Rep., The Air Force Office of Scientific Research, 2014.
- [6] R. Talreja, J. Varna, Modeling Damage, Fatigue and Failure of Composite Materials, Elsevier, 2015.
- [7] J. Sorić, P. Wriggers, O. Allix, Multiscale Modeling of Heterogeneous Structures, Springer, 2018.
- [8] G. Pijaudier-Cabot, F. Dufour, Damage Mechanics of Cementitious Materials and Structures, John Wiley & Sons, 2013.
- [9] C. Mourlas, G. Markou, M. Papadrakakis, Accurate and computationally efficient nonlinear static and dynamic analysis of reinforced concrete structures considering damage factors, Eng. Struct. 178 (2019) 258–285.

- [10] G. Markou, R. Garcia, C. Mourlas, M. Guadagnini, K. Pilakoutas, M. Papadrakakis, A new damage factor for seismic assessment of deficient bare and frp-retrofitted rc structures, Eng. Struct. 248 (2021) 113152.
- [11] E. Lindgren, J. Brausch, C. Buynak, P. Kobryn, M. Leonard, The state of nondestructive evaluation and structural health monitoring, in: Aircraft Structural Integrity Program Conference, 2013.
- [12] M. HDBK, Nondestructive evaluation system reliability assessment, in: Department of Defense Handbook, Vol. 7.
- [13] J.D. Achenbach, Quantitative nondestructive evaluation, Int. J. Solids Struct. 37 (1-2) (2000) 13-27.
- [14] D. Forsyth, M. Gehlen, J. Guthrie, M. Keiser, R. Kent, M. Morgan, C. Pairazaman, D. Stamper, D. Carreon, The air force nondestructive improvement program, in: Proceedings of the 2010 Air Transport Association Nondestructive Testing Forum, Albuquerque, New Mexico, 2010.
- [15] U. AFLCMC, In-service inspection flaw assumptions for metallic structures, Struct. Bull. EN-SB-08-012, no. Rev. C.
- [16] K. Jones, J. Brausch, W. Fong, B. Harris, Probing the future: Better f-16 inspections using conformal eddy current inspection tools, in: Proceedings of 2015 Aircraft Airworthiness & Sustainment Conference, Baltimore, Maryland, 2015.
- [17] B. Pan, L. Yu, Q. Zhang, Review of single-camera stereo-digital image correlation techniques for full-field 3d shape and deformation measurement, Sci. China Technol. Sci. 61 (1) (2018) 2–20.
- [18] K. Shukla, P.C. Di Leoni, J. Blackshire, D. Sparkman, G.E. Karniadakis, Physics-informed neural network for ultrasound nondestructive quantification of surface breaking cracks, Journal of Nondestructive Evaluation 39 (3) (2020) 1–20.
- [19] Y. Kok, X.P. Tan, P. Wang, M. Nai, N.H. Loh, E. Liu, S.B. Tor, Anisotropy and heterogeneity of microstructure and mechanical properties in metal additive manufacturing: A critical review, Mater. Des. 139 (2018) 565–586.
- [20] J. Zhang, B. Song, Q. Wei, D. Bourell, Y. Shi, A review of selective laser melting of aluminum alloys: Processing, microstructure, property and developing trends, J. Mater. Sci. Technol. 35 (2) (2019) 270–284.
- [21] M. Bessa, R. Bostanabad, Z. Liu, A. Hu, D.W. Apley, C. Brinson, W. Chen, W.K. Liu, A framework for data-driven analysis of materials under uncertainty: Countering the curse of dimensionality, Comput. Methods Appl. Mech. Engrg. 320 (2017) 633–667.
- [22] R. Bostanabad, Y. Zhang, X. Li, T. Kearney, L.C. Brinson, D.W. Apley, W.K. Liu, W. Chen, Computational microstructure characterization and reconstruction: Review of the state-of-the-art techniques, Prog. Mater. Sci. 95 (2018) 1-41.
- [23] X. Han, J. Gao, M. Fleming, C. Xu, W. Xie, S. Meng, W.K. Liu, Efficient multiscale modeling for woven composites based on self-consistent clustering analysis, Comput. Methods Appl. Mech. Engrg. 364 (2020) 112929.
- [24] E.A. Lindgren, US air force perspective on validated NDE-past, present, and future, in: AIP Conference Proceedings, Vol. 1706, AIP Publishing LLC, 2016, 020002.
- [25] S.A. Silling, Reformulation of elasticity theory for discontinuities and long-range forces, J. Mech. Phys. Solids 48 (1) (2000) 175–209.
- [26] P. Seleson, M.L. Parks, M. Gunzburger, R.B. Lehoucq, Peridynamics as an upscaling of molecular dynamics, Multiscale Model. Simul. 8 (1) (2009) 204–227.
- [27] M.L. Parks, R.B. Lehoucq, S.J. Plimpton, S.A. Silling, Implementing peridynamics within a molecular dynamics code, Comput. Phys. Comm. 179 (11) (2008) 777–783.
- [28] M. Zimmermann, A Continuum Theory with Long-Range Forces for Solids (Ph.D. thesis), Massachusetts Institute of Technology, 2005.
- [29] E. Emmrich, O. Weckner, Analysis and numerical approximation of an integro-differential equation modeling non-local effects in linear elasticity, Math. Mech. Solids 12 (4) (2007) 363–384.
- [30] Q. Du, K. Zhou, Mathematical analysis for the peridynamic nonlocal continuum theory, ESAIM Math. Model. Numer. Anal. 45 (02) (2011) 217–234.
- [31] F. Bobaru, J.T. Foster, P.H. Geubelle, S.A. Silling, Handbook of peridynamic modeling, CRC press, 2016.
- [32] Y. Yu, F.F. Bargos, H. You, M.L. Parks, M.L. Bittencourt, G.E. Karniadakis, A partitioned coupling framework for peridynamics and classical theory: analysis and simulations, Comput. Methods Appl. Mech. Engrg. 340 (2018) 905–931.
- [33] N. Trask, H. You, Y. Yu, M.L. Parks, An asymptotically compatible meshfree quadrature rule for nonlocal problems with applications to peridynamics, Comput. Methods Appl. Mech. Engrg. 343 (2019) 151–165.
- [34] Y. Yu, H. You, N. Trask, An asymptotically compatible treatment of traction loading in linearly elastic peridynamic fracture, Comput. Methods Appl. Mech. Engrg. 377 (2021) 113691.
- [35] H. You, Y. Yu, S. Silling, M. D'Elia, A data-driven peridynamic continuum model for upscaling molecular dynamics, Comput. Methods Appl. Mech. Engrg. 389 (2022) 114400.
- [36] X. Tian, Q. Du, Analysis and comparison of different approximations to nonlocal diffusion and linear peridynamic equations, SIAM J. Numer. Anal. 51 (6) (2013) 3458–3482.
- [37] Q. Du, Y. Tao, X. Tian, A peridynamic model of fracture mechanics with bond-breaking, J. Elasticity 132 (2) (2018) 197-218.
- [38] N. Prakash, G.D. Seidel, Electromechanical peridynamics modeling of piezoresistive response of carbon nanotube nanocomposites, Comput. Mater. Sci. 113 (2016) 154–170.
- [39] N. Prakash, G.D. Seidel, Computational electromechanical peridynamics modeling of strain and damage sensing in nanocomposite bonded explosive materials (ncbx), Eng. Fract. Mech. 177 (2017) 180–202.
- [40] N. Prakash, Calibrating bond-based peridynamic parameters using a novel least squares approach, J. Peridyn. Nonlocal Model. 1 (1) (2019) 45–55.
- [41] Z.P. Bažant, M. Jirásek, Nonlocal integral formulations of plasticity and damage: survey of progress, J. Eng. Mech. 128 (11) (2002) 1119–1149
- [42] Q. Du, M. Gunzburger, R.B. Lehoucq, K. Zhou, A nonlocal vector calculus, nonlocal volume-constrained problems, and nonlocal balance laws, Math. Models Methods Appl. Sci. 23 (03) (2013) 493–540.
- [43] J. Zhao, Z. Chen, J. Mehrmashhadi, F. Bobaru, A stochastic multiscale peridynamic model for corrosion-induced fracture in reinforced concrete, Eng. Fract. Mech. (2020) 106969.

- [44] E. Emmrich, O. Weckner, et al., On the well-posedness of the linear peridynamic model and its convergence towards the navier equation of linear elasticity, Commun. Math. Sci. 5 (4) (2007) 851–864.
- [45] Y. Fan, X. Tian, X. Yang, X. Li, C. Webster, Y. Yu, An asymptotically compatible probabilistic collocation method for randomly heterogeneous nonlocal problems, J. Comput. Phys. 465 (2022) 111376.
- [46] Q. Guan, M. Gunzburger, C.G. Webster, G. Zhang, Reduced basis methods for nonlocal diffusion problems with random input data, Comput. Methods Appl. Mech. Engrg. 317 (2017) 746–770.
- [47] H.A. Nguyen, H. Wang, S. Tanaka, S. Oterkus, E. Oterkus, An in-depth investigation of bimaterial interface modeling using ordinary state-based peridynamics, J. Peridyn. Nonlocal Model. (2021) 1–27.
- [48] S. Oterkus, E. Madenci, A. Agwai, Peridynamic thermal diffusion, J. Comput. Phys. 265 (2014) 71-96.
- [49] F. Wang, L. Liu, Q. Liu, D. Cao, S. Yang, Studies of bimaterial interface fracture with peridynamics, in: 2015 International Power, Electronics and Materials Engineering Conference, Atlantis Press, 2015, pp. 856–861.
- [50] D. Behera, P. Roy, E. Madenci, Peridynamic modeling of bonded-lap joints with viscoelastic adhesives in the presence of finite deformation, Comput. Methods Appl. Mech. Engrg. 374 (2021) 113584.
- [51] J. Mehrmashhadi, Y. Tang, X. Zhao, Z. Xu, J.J. Pan, Q. Van Le, F. Bobaru, The effect of solder joint microstructure on the drop test failure—a peridynamic analysis, IEEE Trans. Components Packag. Manuf. Technol. 9 (1) (2018) 58–71.
- [52] X. Tian, Q. Du, Asymptotically compatible schemes and applications to robust discretization of nonlocal models, SIAM J. Numer. Anal. 52 (4) (2014) 1641–1665.
- [53] M. D'Elia, Q. Du, C. Glusa, M. Gunzburger, X. Tian, Z. Zhou, Numerical methods for nonlocal and fractional models, Acta Numerica 29 (2020) 1–124.
- [54] Y. Leng, X. Tian, N. Trask, J.T. Foster, Asymptotically compatible reproducing kernel collocation and meshfree integration for nonlocal diffusion, SIAM Journal on Numerical Analysis 59 (1) (2021) 88–118.
- [55] M. Pasetto, Y. Leng, J.-S. Chen, J.T. Foster, P. Seleson, A reproducing kernel enhanced approach for peridynamic solutions, Comput. Methods Appl. Mech. Engrg. 340 (2018) 1044–1078.
- [56] M. Hillman, M. Pasetto, G. Zhou, Generalized reproducing kernel peridynamics: unification of local and non-local meshfree methods, non-local derivative operations, and an arbitrary-order state-based peridynamic formulation, Comput. Part. Mech. 7 (2) (2020) 435–469.
- [57] P. Seleson, D.J. Littlewood, Convergence studies in meshfree peridynamic simulations, Comput. Math. Appl. 71 (11) (2016) 2432–2448.
- [58] Q. Du, Local limits and asymptotically compatible discretizations, in: Handbook of Peridynamic Modeling, 2016, pp. 87-108.
- [59] H. You, X. Lu, N. Trask, Y. Yu, An asymptotically compatible approach for neumann-type boundary condition on nonlocal problems, ESAIM Math. Model. Numer. Anal. 54 (4) (2020) 1373–1413.
- [60] H. You, Y. Yu, D. Kamensky, An asymptotically compatible formulation for local-to-nonlocal coupling problems without overlapping regions, Comput. Methods Appl. Mech. Engrg. 366 (2020) 113038.
- [61] Y. Tao, X. Tian, Q. Du, Nonlocal diffusion and peridynamic models with neumann type constraints and their numerical approximations, Appl. Math. Comput. 305 (2017) 282–298.
- [62] S.A. Silling, E. Askari, A meshfree method based on the peridynamic model of solid mechanics, Comput. Struct. 83 (17–18) (2005) 1526–1535.
- [63] M. Bessa, J. Foster, T. Belytschko, W.K. Liu, A meshfree unification: reproducing kernel peridynamics, Comput. Mech. 53 (6) (2014) 1251–1264.
- [64] F. Bobaru, M. Yang, L.F. Alves, S.A. Silling, E. Askari, J. Xu, Convergence, adaptive refinement, and scaling in 1d peridynamics, Internat. J. Numer. Methods Engrg. 77 (6) (2009) 852–877.
- [65] M. Foss, P. Radu, Y. Yu, Convergence analysis and numerical studies for linearly elastic peridynamics with dirichlet-type boundary conditions, Journal of Peridynamics and Nonlocal Modeling (2022) 1–36.
- [66] I. Babuska, R. Tempone, G.E. Zouraris, Galerkin finite element approximations of stochastic elliptic partial differential equations, SIAM J. Numer. Anal. 42 (2) (2004) 800–825.
- [67] I. Babuška, R. Tempone, G.E. Zouraris, Solving elliptic boundary value problems with uncertain coefficients by the finite element method: the stochastic formulation, Comput. Methods Appl. Mech. Engrg. 194 (12–16) (2005) 1251–1294.
- [68] R.G. Ghanem, P.D. Spanos, Stochastic Finite Elements: A Spectral Approach, Courier Corporation, 2003.
- [69] O. Le Maitre, O. Knio, H. Najm, R. Ghanem, Uncertainty propagation using wiener-haar expansions, J. Comput. Phys. 197 (1) (2004) 28–57.
- [70] H.G. Matthies, A. Keese, Galerkin methods for linear and nonlinear elliptic stochastic partial differential equations, Comput. Methods Appl. Mech. Engrg. 194 (12–16) (2005) 1295–1331.
- [71] D. Xiu, G.E. Karniadakis, The wiener–askey polynomial chaos for stochastic differential equations, SIAM J. Sci. Comput. 24 (2) (2002) 619–644.
- [72] X. Wan, G.E. Karniadakis, An adaptive multi-element generalized polynomial chaos method for stochastic differential equations, J. Comput. Phys. 209 (2) (2005) 617–642.
- [73] D. Xiu, J.S. Hesthaven, High-order collocation methods for differential equations with random inputs, SIAM J. Sci. Comput. 27 (3) (2005) 1118–1139.
- [74] F. Nobile, R. Tempone, C.G. Webster, An anisotropic sparse grid stochastic collocation method for partial differential equations with random input data, SIAM J. Numer. Anal. 46 (5) (2008) 2411–2442.
- [75] X. Ma, N. Zabaras, An adaptive hierarchical sparse grid collocation algorithm for the solution of stochastic differential equations, J. Comput. Phys. 228 (8) (2009) 3084–3113.
- [76] G. Zhang, M. Gunzburger, Error analysis of a stochastic collocation method for parabolic partial differential equations with random input data, SIAM J. Numer. Anal. 50 (4) (2012) 1922–1940.

- [77] G. Lin, A.M. Tartakovsky, An. efficient, High-order probabilistic collocation method on sparse grids for three-dimensional flow and solute transport in randomly heterogeneous porous media, Adv. Water Resour. 32 (5) (2009) 712–722.
- [78] G. Rozza, D.B.P. Huynh, A.T. Patera, Reduced basis approximation and a posteriori error estimation for affinely parametrized elliptic coercive partial differential equations, Arch. Comput. Methods Eng. 15 (3) (2007) 1.
- [79] G. Rozza, K. Veroy, On the stability of the reduced basis method for stokes equations in parametrized domains, Comput. Methods Appl. Mech. Engrg. 196 (7) (2007) 1244–1260.
- [80] P. Chen, A. Quarteroni, G. Rozza, Comparison between reduced basis and stochastic collocation methods for elliptic problems, J. Sci. Comput. 59 (1) (2014) 187–216.
- [81] P. Chen, A. Quarteroni, G. Rozza, A weighted reduced basis method for elliptic partial differential equations with random input data, SIAM J. Numer. Anal. 51 (6) (2013) 3163–3185.
- [82] H.C. Elman, Q. Liao, Reduced basis collocation methods for partial differential equations with random coefficients, SIAM/ASA J. Uncertain. Quantif. 1 (1) (2013) 192–217.
- [83] F. Serbena, I. Mathias, C. Foerster, E. Zanotto, Crystallization toughening of a model glass-ceramic, Acta Mater. 86 (2015) 216–228.
- [84] G. Capodaglio, M. D'Elia, P. Bochev, M. Gunzburger, An energy-based coupling approach to nonlocal interface problems, Comput. & Fluids 207 (2020) 104593.
- [85] C. Glusa, M. D'Elia, G. Capodaglio, M. Gunzburger, P.B. Bochev, An asymptotically compatible coupling formulation for nonlocal interface problems with jumps arXiv:2203.07565.
- [86] T. Mengesha, Nonlocal korn-type characterization of sobolev vector fields, Commun. Contemp. Math. 14 (04) (2012) 1250028.
- [87] T. Mengesha, Q. Du, The bond-based peridynamic system with Dirichlet-type volume constraint, Proc. Roy. Soc. Edinburgh Sect. A 144 (1) (2014) 161–186.
- [88] T. Mengesha, Q. Du, Nonlocal constrained value problems for a linear peridynamic Navier equation, J. Elasticity 116 (1) (2014) 27–51.
- [89] N. Prakash, B. Deng, R.J. Stewart, C.M. Smith, J.T. Harris, Investigation of microscale fracture mechanisms in glass-ceramics using peridynamics simulations, J. Am. Ceram. Soc..
- [90] A. Brudnyi, et al., Methods of Geometric Analysis in Extension and Trace Problems. Vol. 1, Springer Science & Business Media, 2011, p. 102.
- [91] H. Zhang, P. Qiao, A state-based peridynamic model for quantitative fracture analysis, Int. J. Fract. 211 (1-2) (2018) 217-235.
- [92] A. Agwai, I. Guven, E. Madenci, Predicting crack propagation with peridynamics: a comparative study, Int. J. Fract. 171 (1) (2011) 65–78.
- [93] M. Tatang, G. McRae, Direct Treatment of Uncertainty in Models of Reaction and Transport, Technical report, MIT Tech. Rep.
- [94] A. Keese, H. Matthies, et al., Numerical methods and Smolyak quadrature for nonlinear stochastic partial differential equations.
- [95] H. Wendland, Scattered Data Approximation, Vol. 17, Cambridge University Press, 2004.
- [96] S.A. Silling, R.B. Lehoucq, Peridynamic theory of solid mechanics, Adv. Appl. Mech. 44 (2010) 73–168.
- [97] S.A. Smolyak, Quadrature and interpolation formulas for tensor products of certain classes of functions, in: Doklady Akademii Nauk, Vol. 148, Russian Academy of Sciences, 1963, pp. 1042–1045.
- [98] E. Novak, K. Ritter, High dimensional integration of smooth functions over cubes, Numer. Math. 75 (1) (1996) 79-97.
- [99] E. Novak, K. Ritter, Simple cubature formulas with high polynomial exactness, Constr. Approx. 15 (4) (1999) 499-522.
- [100] F. Nobile, R. Tempone, C.G. Webster, A sparse grid stochastic collocation method for partial differential equations with random input data, SIAM J. Numer. Anal. 46 (5) (2008) 2309–2345.
- [101] I. Babuška, F. Nobile, R. Tempone, A stochastic collocation method for elliptic partial differential equations with random input data, SIAM J. Numer. Anal. 45 (3) (2007) 1005–1034.
- [102] E.A.S.A. Silling, A meshfree method based on the peridynamic model of solid mechanics, Comput. Struct. 83 (2005) 1526–1535.
- [103] Y. Wang, C. Cerigato, H. Waisman, E. Benvenuti, Xfem with high-order material-dependent enrichment functions for stress intensity factors calculation of interface cracks using irwin's crack closure integral, Eng. Fract. Mech. 178 (2017) 148–168.
- [104] J. Foo, X. Wan, G.E. Karniadakis, The multi-element probabilistic collocation method (me-pcm): Error analysis and applications, J. Comput. Phys. 227 (22) (2008) 9572–9595.
- [105] J.D. Jakeman, A. Narayan, D. Xiu, Minimal multi-element stochastic collocation for uncertainty quantification of discontinuous functions, J. Comput. Phys. 242 (2013) 790–808.
- [106] J.A. Witteveen, G. Iaccarino, Simplex stochastic collocation with eno-type stencil selection for robust uncertainty quantification, J. Comput. Phys. 239 (2013) 1–21.
- [107] J.A. Witteveen, G. Iaccarino, Simplex stochastic collocation with eno-type stencil selection for robust uncertainty quantification, J. Comput. Phys. 239 (2013) 1–21.
- [108] F.C. Serbena, E.D. Zanotto, Internal residual stresses in glass-ceramics: A review, J. Non-Crystalline Solids 358 (6-7) (2012) 975-984.
- [109] S. Freiman, L. Hench, Effect of crystallization on the mechanical properties of li2o-sio2 glass-ceramics, J. Am. Ceram. Soc. 55 (2) (1972) 86–90.
- [110] W. Holand, G.H. Beall, Glass-Ceramic Technology, John Wiley & Sons, 2019.
- [111] Q. Fu, G.H. Beall, C.M. Smith, Nature-inspired design of strong, tough glass-ceramics, MRS Bull. 42 (3) (2017) 220–225.
- [112] Y. Li, M. Zhou, Prediction of fracturess toughness of ceramic composites as function of microstructure: Ii. analytical model, J. Mech. Phys. Solids 61 (2) (2013) 489–503.
- [113] R.A. DeVore, G.G. Lorentz, Constructive Approximation, Vol. 303, Springer Science & Business Media, 1993.